DISSERTATION

submitted

to the

Combined Faculty for the Natural Sciences and Mathematics

of

Heidelberg University, Germany

for the degree of

Doctor of Natural Sciences

Put forward by

Marco Tektonidis

Born in: Bückeburg, Germany

Oral examination: .....

Non-Rigid Multi-Frame Registration of Cell Nuclei in Live Cell Microscopy Image Data

Advisor: PD Dr. Karl Rohr

Abstract

To gain a better understanding of cellular and molecular processes it is important to quantitatively analyze the motion of subcellular particles in live cell microscopy image sequences. For accurate quantification of the subcellular particle motion, compensation of the motion and deformation of the cell nucleus is required. This thesis deals with non-rigid registration of cell nuclei in 2D and 3D live cell fluorescence microscopy images. We developed two multi-frame non-rigid registration approaches which simultaneously exploit information from multiple consecutive frames of an image sequence to improve the registration accuracy. The multi-frame registration approaches are based on local optic flow estimation, use information from multiple consecutive images, and take into account computed transformations from previous time steps. The first approach comprises three intensity-based variants and two different temporal weighting schemes. The second approach determines diffeomorphic transformations in the log-domain which allows efficient computation of the inverse transformations. We use a temporally weighted mean image which is constructed based on inverse transformations and multiple consecutive frames. In addition, we employ a flow boundary preserving method for regularization of computed deformation vector fields. Both multi-frame registration approaches have been successfully applied to 2D and 3D synthetic as well as real live cell microscopy image sequences. We have performed an extensive quantitative evaluation of our approaches and compared their performance with previous non-rigid pairwise, multi-frame, and temporal groupwise registration approaches.

Zusammenfassung

Die quantitative Analyse der Bewegung von subzellulären Partikeln in Mikroskopie-Bildsequenzen lebender Zellen ist wichtig, um zelluläre und molekulare Prozesse besser zu verstehen. Die genaue Quantifizierung der Partikelbewegung im Inneren einer Zelle erfordert die Kompensierung der Bewegung und der Deformation des Zellkerns. Diese Dissertation beschäftigt sich mit der nicht-starren Registrierung von Zellkernen in 2D- und 3D-Fluoreszenzmikroskopie-Bildern von lebenden Zellen. Wir haben zwei nicht-starre multi-frame Registrierungsverfahren entwickelt, die Informationen von mehreren aufeinanderfolgenden Bildern einer Bildsequenz gleichzeitig nutzen, um die Registrierungsgenauigkeit zu erhöhen. Die multi-frame Registrierungsverfahren basieren auf lokalem optischen Fluss, verwenden Informationen von mehreren aufeinanderfolgenden Bildern und berücksichtigen die berechneten Transformationen von früheren Zeitpunkten. Das erste Verfahren besteht aus drei intensitätsbasierten Varianten und zwei unterschiedlichen zeitlichen Gewichtungsschemata. Das zweite Verfahren berechnet diffeomorphische Transformationen in der logarithmischen Domäne, die eine effiziente Berechnung der inversen Transformationen ermöglicht. Wir verwenden ein zeitlich gewichtetes Mittelbild, dessen Berechnung auf inversen Transformationen und mehreren aufeinanderfolgenden Bildern basiert. Zusätzlich verwenden wir eine flussgrenzerhaltende Methode für die Regularisierung der berechneten Deformationsvektorfelder. Beide multi-frame Registrierungsverfahren wurden erfolgreich auf 2D und 3D synthetische sowie reale Mikroskopiebildsequenzen lebender Zellen angewendet. Ferner haben wir eine quantitative

Evaluierung unserer Verfahren durchgeführt und ihre Leistung mit existierenden nicht-starren paarweisen, multi-frame und zeitlichen gruppenbasierten Registrierungsverfahren verglichen.

Acknowledgements

I would like to express my gratitude to PD Dr. Karl Rohr for giving me the opportunity to work on a very interesting topic and to accomplish this work with this thesis at the Faculty of Mathematics and Computer Science of Heidelberg University. This would not have been possible without his invaluable guidance, his wise advices, and his immense expertise in the field. I would also like to thank him for constantly trying to teach me how important precision is, not only for writing an article, but in every academic or professional context.

I would also like to express my sincere gratitude to Prof. Hartmut Dickhaus for being my second reviewer. Special thanks to Dr. Frank Christnacher and Dr. David Monnin from ISL for their support during the completion of this thesis, and to Prof. Andreas Deutsch, Dr. Babis Hatzikirou and Dr. Arnaud Chauviere for giving me the opportunity to enter the "academic world" at the TU Dresden which played an important role in my decision to pursue a PhD.

I am also very grateful to my colleagues in the BMCV group of Heidelberg University and DKFZ, Jan-Philip Bergeest, Dr. Andreas Biesdorf, Simon Eck, Dr. Astha Jaiswal, Dr. William J. Godinez, Dr. Nathalie Harder, Il-Han Kim, Wei Liao, Dr. Dmitry Sorokin, Vasil Tsimashchuk, and Dr. Stefan Wörz for the helpfulness, the discussions, the collaboration, and the countless coffee breaks.

Finally, thanks to Sara for her support and patience, she is probably one of few social workers able to explain the meaning of "non-rigid registration of cell nuclei". I would also like to thank my family for the encouragement, especially my two little nieces who always know how to make me laugh, and of course my friends for the support.

Publications

Journal Papers

- D. V. Sorokin, I. Peterlik, **M. Tektonidis**, K. Rohr, and P. Matula, Non-rigid contour-based registration of cell nuclei in 2D live cell microscopy images using a dynamic elasticity model, *IEEE Transactions on Medical Imaging*, vol. 37, no. 1, pp. 173-184, 2018.

- **M. Tektonidis** and K. Rohr, Diffeomorphic multi-frame non-rigid registration of cell nuclei in 2D and 3D live cell images, *IEEE Transactions on Image Processing*, vol. 26, no. 3, pp. 1405-1417, 2017.

- **M. Tektonidis**, I.-H. Kim,Y.-C. M. Chen, R. Eils, D. L. Spector, and K. Rohr, Non-rigid multi-frame registration of cell nuclei in live cell fluorescence microscopy image data, *Medical Image Analysis*, vol. 19, no. 1, pp. 1-14, 2015.

- L. Chang, W. J. Godinez, I.-H. Kim, **M. Tektonidis**, P. de Lanerolle, R. Eils, K. Rohr, and D. M. Knipe, Herpesviral replication compartments move and coalesce at nuclear speckles to enhance export of viral late mRNA, *Proceedings of the National Academy of Sciences (PNAS)*, vol. 108, no. 21, pp. E136-E144, 2011.

Conference Papers

- D. V. Sorokin, **M. Tektonidis**, K. Rohr, and P. Matula, Non-rigid contour-based temporal registration of 2D cell nuclei images using the Navier equation, in *Proc. IEEE International Symposium on Biomedical Imaging (ISBI)*, Beijing, China, pp. 746-749, 2014.

- **M. Tektonidis**, I.-H. Kim, and K. Rohr, Non-rigid multi-frame registration of live cell microscopy images, in *Proc. IEEE International Symposium on Biomedical Imaging (ISBI)*, Barcelona, Spain, pp. 438-441, 2012.

Contents

List of Figures

List of Tables

Chapter 1

Introduction

1.1 Motivation

The time-resolved behaviour of cellular and subcellular structures observed in temporal microscopy image sequences plays an important role in molecular biology. Biomolecular systems are dynamic, and one of the major challenges of biomedical research is to unravel the spatial and temporal relationships of these complex systems and to gain insight into the underlying biological processes. The study of the movement of subcellular structures, in particular, particles within the cell nucleus is important for understanding cell function, since the nuclear structure and dynamics play a critical role in many cellular processes [1, 2]. Various nuclear bodies have been shown to modify proteins and process RNAs, and are thus involved in the regulation of gene expression and its implications for human disease [3]. The study of the localization, dynamics, and interaction of these subcellular particles are essential for the understanding of cell function. For example, the study of the movement of promyelocytic leukemia nuclear bodies is important for understanding the potential contributions of cellular functions to certain human diseases, since these particles play a role in tumor suppression, viral defense, or DNA repair [4].

Fluorescence microscopy allows imaging subcellular particles by using fluorescent

proteins. Based on this technique time-lapse image sequences can be acquired for monitoring the location of subcellular particles over time. However, besides the motion of particles within a cell nucleus, also the motion and deformation of the nucleus are observed in the images. The observed motion in the image data represents therefore a mixture of both the motion of the particles and the motion and deformation of the nucleus (Figs. 1.1 and 1.2). Thus, a quantitative analysis of particle motion directly on the original microscopy image data is generally inaccurate.

To compensate the nucleus motion and deformation, image registration techniques can be used to align the frames of a time-lapse image sequence with reference to the first frame. Image registration yields a mapping of homologous points of a cell along the sequence of images, which can be used to compensate the cell nucleus motion and deformation. The registration task can be quite challenging for a number of reasons, for example, autofluorescence causes significant background noise, and photobleaching reduces the image contrast over time. Additional challenges exist for image sequences acquired during prophase and prometaphase, when cell nuclei are going into mitosis (cell division). During these cell phases, the shape and the intensity structure of the nucleus are changing strongly due to, for example, chromatin condensation which leads to the shrinking of the nucleus, nuclear envelope breakdown which causes the disassembly of the nucleus (cf. Figs. 1.1 and 1.2), or the disappearance of internal structures such as the nucleoli.

1.2 Registration of Live Cell Microscopy Images

In this work, we consider image registration approaches to compensate the nucleus motion and deformation in live cell microscopy image sequences. In this section, we first introduce the basic biological concepts for the cell nucleus, focusing on the behavior of nuclei during mitotic entry. Next, we describe the properties and issues of the image data

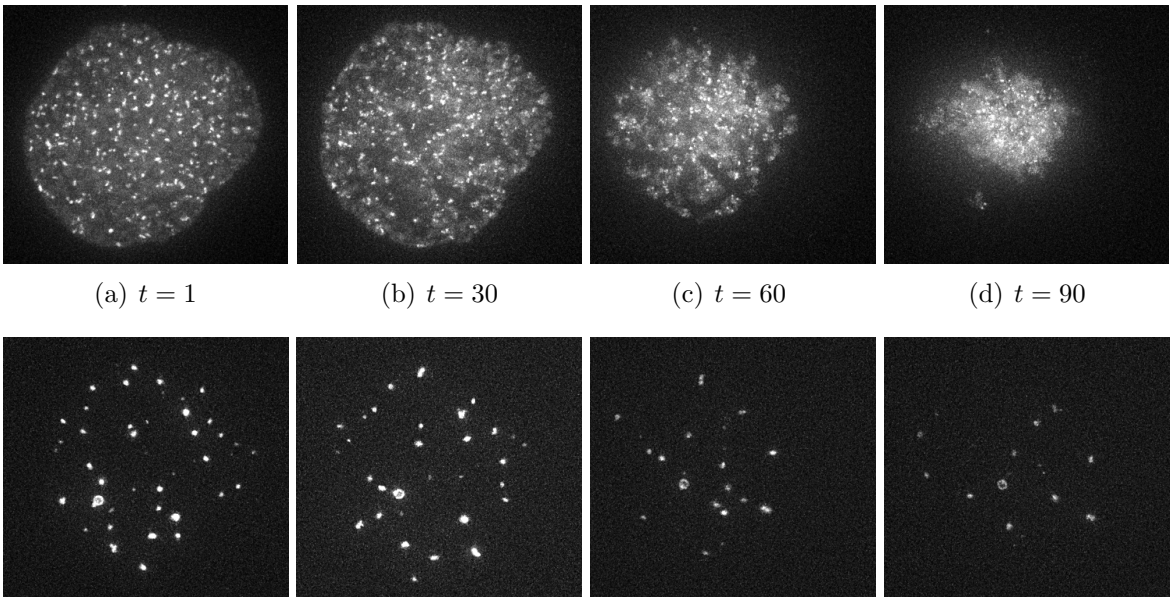

(a) $t = 1$ (b) $t = 30$ (c) $t = 60$ (d) $t = 90$

(e) $t = 1$ (f) $t = 30$ (g) $t = 60$ (h) $t = 90$

Figure 1.1: Example images from a 2D dynamic two-channel microscopy image sequence ((a)-(d) nucleus channel, (e)-(h) particle channel, contrast enhanced).

acquired using time-lapse fluorescence microscopy and then we discuss the challenges of the image registration task on compensating cell nucleus and deformation in time-lapse fluorescence microscopy image data.

1.2.1 Cell Nucleus and Entry into Mitosis

The cell nucleus is the largest and most important organelle in an eukaryotic cell, playing a central role in many cellular functions. This well-organized and highly compartmentalized organelle contains the majority of the genetic material of a cell, organized as multiple chromosomes. The genetic information directs the activity of the entire cell, and the most important cellular processes take place within the cell nucleus, such as DNA replication and recombination as well as RNA transcription and processing [5]. The nucleus is physically separated from the cytoplasm of a cell by the nuclear envelope which consists of an inner and an outer membrane. Important functions of the nuclear envelope are that it encloses the genetic material and that it allows interactions

of proteins between the nucleus and the cytoplasm [6].

During prophase and prometaphase, i.e., the first stages of mitosis (cell division), cell nuclei undergo significant and irreversible changes. Events which cause changes to cell nuclei and degrade the nucleo-cytoplasmic compartmentation are *nuclear envelope breakdown* and *chromatin condensation* [7]. When nuclear envelope breakdown occurs, the nuclear envelope disassembles and forms compartments, creating gaps at the border between the nucleus and the cytoplasm. In Figs. 1.1(c) and 1.2(c) we show examples of microscopy images acquired during nuclear envelope breakdown. It can be seen, that the shape of the cell nucleus changes significantly, and that a clear boundary between the nucleus and the cytoplasm is not visible.

After nuclear envelope breakdown, chromatin (i.e., a complex of macromolecules consisting of DNA, protein, and RNA) condenses to form chromosomes. Condensed chromatin is a major contributor to nuclear stiffness [2] and it has been shown that chromatin condensation leads to nucleus shrinking [8]. In Figs. 1.1 and 1.2 it can be seen, that the depicted nucleus shrinks significantly over time. In addition, nucleoli which are located within cell nuclei, disappear during prophase. To summarize, during the first stages of mitosis different events occur which significantly change the shape and the structure of cell nuclei.

1.2.2 Time-Lapse Fluorescence Microscopy

Fluorescence microscopy plays an important role in cellular and molecular biology since it allows to visualize cellular, subcellular or molecular structures in live cells and tissues [9]. This imaging technique is based on tagging structures of interest using fluorophores (e.g., green fluorescent protein, GFP). The fluorophores emit light of different wavelength compared to the light emitted by the background after excitation with a light source, such as a laser. The structures of interest are visualized with higher contrast in the acquired image data, compared to imaging techniques which are based on the absorp-

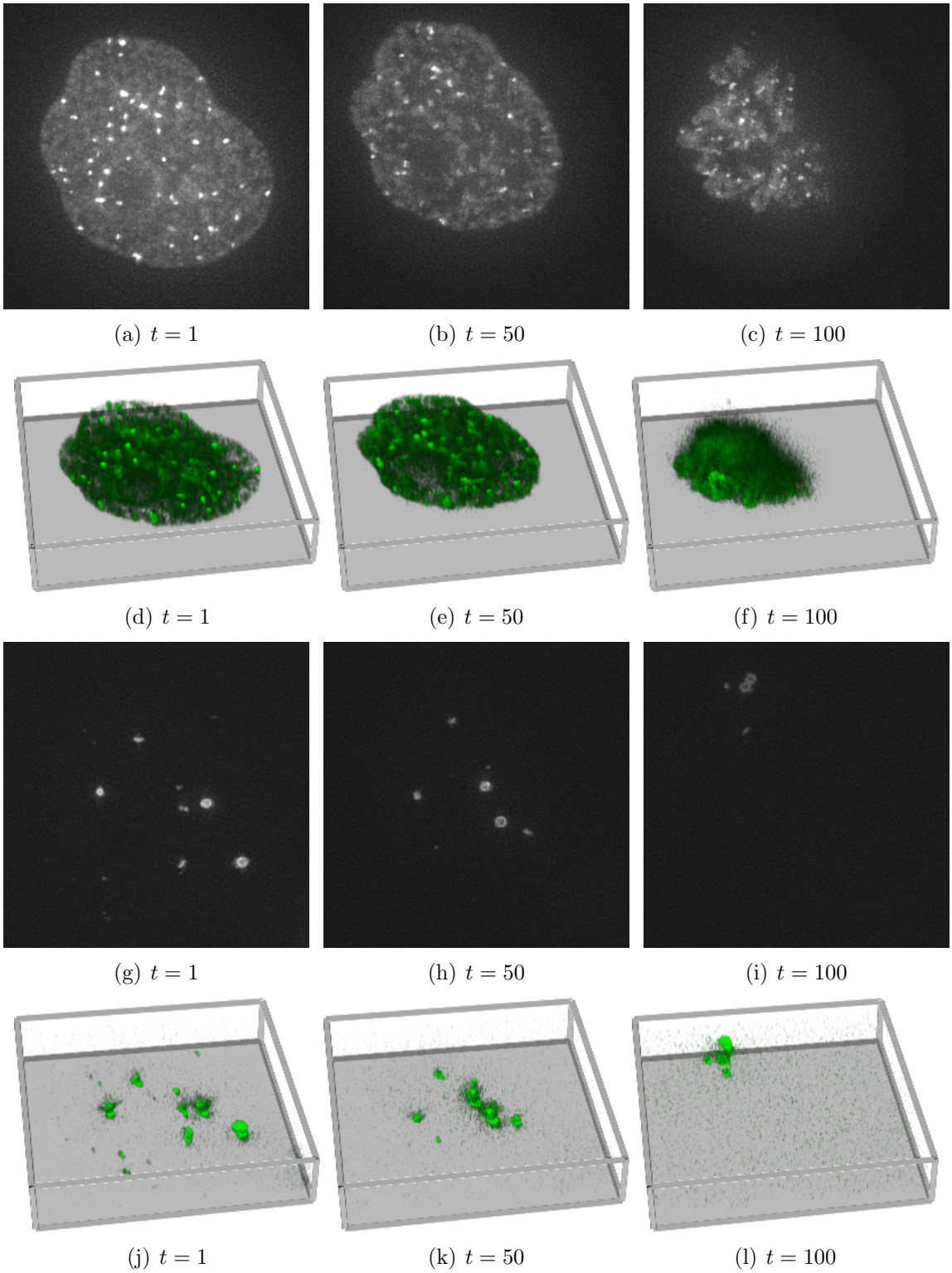

(a) $t = 1$ (b) $t = 50$ (c) $t = 100$

(d) $t = 1$ (e) $t = 50$ (f) $t = 100$

(g) $t = 1$ (h) $t = 50$ (i) $t = 100$

(j) $t = 1$ (k) $t = 50$ (l) $t = 100$

Figure 1.2: Example images from a 3D dynamic two-channel microscopy image sequence ((a)-(f) nucleus channel, (g)-(l) particle channel, contrast enhanced). (a)-(c) and (g)-(i): maximum intensity projection (MIP) images, and (d)-(f) and (j)-(l): rendered volumes.

tion of light. Tagging different subcellular structures with different fluorophores allows to simultaneously acquire multiple images of the different structures (*multi-channel* image data). A drawback of fluorescence microscopy is that the background may also emit light since different cellular structures have intrinsic *autofluorescence* [9]. The autofluorescence decreases the contrast between the structures of interest and the background. Additional factors which degrade the quality of fluorescence microscopy image data are the inherent image noise and optical limitations of fluorescent microscopes related to the small size of the structures of interest.

In *time-lapse fluorescence microscopy*, the acquisition of temporal image sequences enables to study the dynamics of tagged structures of interest over time. An issue with time-lapse imaging is that the used fluorophores permanently lose their ability to fluoresce due to chemical damages caused by the light source (*photobleaching*). This results in a decrease of the intensity of the emitted light over time. Hence, the intensity levels for a structure of interest in an image sequence decrease over time, and the contrast of the structures w.r.t. the background decreases over time as well.

1.2.3 Image Registration Tasks and Challenges

The cell nucleus motion and deformation in live cell microscopy image sequences can be compensated using image registration approaches. Accurate registration is crucial since registration errors influence the subsequent study of particle movement and degrade the performance of the quantitative motion analysis. The microscopy image data is often acquired with two channels, one displaying the cell nucleus (e.g., the chromatin), and the other displaying the subcellular particles of interest. Using the nucleus channel of an image sequence (e.g., Fig. 1.1(a-d)), registration can be used to compute transformations between each frame of the sequence and a reference frame (typically the first frame of the sequence). The determined transformations describe the change in position over time for each image point in the nucleus channel. Then, the transformations can be applied

to the image sequences of the particle channel to compensate for the nucleus motion and deformation (e.g., Fig. 1.2(a-f)). Having decoupled the particle motion from the nucleus motion and deformation, the motion of subcellular particles can be accurately quantified.

Registration of cell nuclei in fluorescence microscopy image data is not a trivial task, due to challenges related to fluorescence microscopy and properties of cell nuclei. Determining transformations between corresponding image frames is difficult due to the typically low quality of microscopy images. The optical limitations of typical fluorescent microscopes in conjunction with the small size of the cellular structures result in a distorted appearance of the intensities of these structures. Cellular autofluorescence, i.e. the light emission of the cellular background, generally leads to a low contrast in the acquired images. In addition, the contrast is decreasing over time due to photobleaching, since the fluorescence intensity decreases over time. Due to these factors, as well as the typically high level of the inherent image noise, the intensity of corresponding image structures in the different frames can differ significantly. Cell nuclei going into mitosis introduce additional challenges. The significant structural changes that occur during this cell phase (e.g., change of the nucleus shape, disappearance of structures) further influences the image intensities over time and increases the difficulties of the registration task. To summarize, the registration of cell nuclei in live microscopy image sequences involves a number of challenges, such as the limitations of fluorescent microscopes, the inherent image noise, photobleaching, and structural changes which occur in cell nuclei going into mitosis.

1.3 Approach and Contributions

This dissertation is concerned with non-rigid registration of cell nuclei in time-lapse microscopy images. The image data in our application consist of two channels (nucleus

channel and particle channel) and the displayed cells are going into mitosis. Therefore, strong changes in the intensity structure and strong deformations occur over time. In particular:

- We propose two intensity-based *multi-frame* non-rigid registration approaches based on optic flow estimation. Compared to pairwise registration, the proposed approaches take advantage of additional temporal information to improve the registration accuracy. In both multi-frame approaches, each frame of an image sequence is registered by exploiting information from multiple consecutive images and by taking into account computed transformations from previous time steps. A local differential consecutive registration scheme is employed which computes deformation vectors for each pixel of an image and thus exploits the full image information. This is important in our application because of the strong structural changes that increase over time (e.g., nuclear envelope breakdown, disappearance of nucleoli). Moreover, an advantage compared to, for example, contour-based registration approaches is that segmentation of the cell nuclei is not required since the intensity-based approaches exploit directly the image intensities.

- Our first multi-frame non-rigid registration approach computes a transformation for each frame of a live cell temporal microscopy image sequence based on the minimization of the sum of squared intensity differences between the current frame and several previous frames. The previous images are warped using the transformations computed at previous time steps. Transformations are represented by deformation vector fields and regularization of transformations is performed using Gaussian kernels. We present a symmetric, a weighting, and a symmetric weighting variant of our intensity-based non-rigid multi-frame registration approach. In addition, we propose two temporal weighting schemes which control the influence of single previous frames on the registration result, based on the temporal distance and on the image similarity.

- Our second approach is a diffeomorphic multi-frame non-rigid registration approach and computes diffeomorphic transformations, which guarantees the invertibility of the transformations. This is important since the inverse of the computed transformations is required for multi-frame registration. The transformations are determined based on velocity vector fields which are computed in the *log-domain* and allow efficient computation of the inverse transformations. This is advantageous, since the inverse transformations are required at each time point of an image sequence. Diffeomorphic multi-frame non-rigid registration approaches have not been employed earlier for dynamic live cell image data. To register single images of an image sequence to a reference image, we use a temporally weighted mean image which is constructed based on inverse transformations and multiple consecutive frames. The diffeomorphic transformations are computed based on the minimization of the sum of squared intensity differences between each image of the image sequence and the temporal mean image. We present a weighting as well as a symmetric weighting intensity-based variant of our diffeomorphic multi-frame registration approach. In addition, for regularization of the computed deformation vector fields, we use a flow boundary preserving method instead of standard Gaussian smoothing to avoid over-smoothing.

- We have successfully applied our multi-frame non-rigid registration approaches to 2D and 3D synthetic as well as real live cell microscopy image data of cell nuclei. We have used the nucleus channel of the image sequences, which consist of a relatively large number of image frames (100-200 time points). To quantitatively assess the performance of the developed approaches, we determined the registration errors using synthetic image sequences with ground truth transformations and using real image sequences with manually determined spot-like structures. We also performed an experimental comparison with previous pairwise [10], [11], and temporal groupwise [12] registration approaches. It turned out, that our multi-

frame approaches outperform previous registration approaches.

1.4 Overview of the Thesis

This thesis is organized as follows. In Chapter 2 we review previous work on image registration with focus on biomedical applications. Chapter 3 introduces our non-diffeomorphic multi-frame approach for non-rigid registration of cell nuclei in live cell microscopy image sequences. We also present three intensity-based variants of the multi-frame registration approach and investigate two different temporal weighting schemes. In Chapter 4 we introduce our diffeomorphic multi-frame non-rigid registration approach using a temporally weighted mean image. We describe the used iterative log-domain diffeomorphic registration scheme as well as the flow boundary preserving method for regularization of the deformation vector fields. In Chapter 5 we present experimental results for the proposed multi-frame registration approaches using both synthetic and real live cell microscopy image data. We also performed an experimental comparison with previous registration approaches. Finally, in Chapter 6 we conclude the thesis with a discussion and a summary.

Chapter 2

Overview of Previous Work

In this chapter, we first describe the basic concepts of image registration and focus on registration approaches based on optical flow. Then, we review previous approaches for registration of cells and cell nuclei in microscopy image data. Registration approaches for other biological applications using microscopy image data are also discussed. Finally, we describe previous methods for temporal registration in medical image analysis and point out the differences to temporal registration of cell nuclei in microscopy image data.

2.1 Image Registration

Image registration describes the process of determining an optimal geometric transformation that maps a target (or moving) image to a reference (or fixed) image, such that corresponding structures in the two images are aligned to each other [13]. The two images can depict the same object acquired at different time points, or different objects. The task of image registration is challenging due to the wide range of applications and the wide range of imaging modalities. Thus, a universal approach that is appropriate for all registration tasks does not exist [14]. In addition, the registration task describes a challenging optimization problem, since often the problem of determining an optimal transformation does not have a unique solution (ill-posedness of image registration [15]).

Registration approaches require a selection of a feature space, a similarity measure which describes the alignment quality, a transformation type, and a search strategy. For reviews on image registration, we refer to, for example, Zitová and Flusser [14], Crum et al. [16], and Holden [13]. Registration approaches have been widely used in biomedical applications, for example, to align cells or organs in images acquired at different time points. For reviews in biomedical image registration we refer to, for example, Maintz and Viergever [17], Rohr [18, 19], Oliveira and Tavares [20], and Sotiras et al. [15]. In the following, we review registration approaches and distinguish between the employed transformation model (i.e., rigid, affine, or non-rigid) and the used type of information for the alignment of the images (i.e. geometry-based or intensity-based).

2.1.1 Transformation Model

The transformation model should be chosen based on the type of the geometric transformation that is required to align the objects of interest in the different images. The geometric transformation can be rigid, affine, or non-rigid, and defines the degrees of freedom that can be used to align the images.

Rigid transformations can be described by a single rotation and a translation. For registration problems which require more degrees of freedom, the rigid transformation can be extended to an *affine* transformation, which additionally includes scaling and shearing. Rigid and affine transformation models are *global*, since the same transformation is used to align all image points. However, for images with objects that are deforming, rigid or affine transformations are not sufficient. In this case, *non-rigid* transformations are required which describe *local* transformations (i.e. different transformations may be required for the alignment of different image points).

Non-rigid transformations vary from smooth regional variations using a small number of parameters to dense deformation fields describing the transformation at each image point (pixel or voxel). Non-rigid registration approaches determine deformations either

allowing any type of transformation (free-form transformations), or based on a physical model which takes into account the properties of the object of interest (e.g., tissue elasticity or fluid flow). *Free-form* registration approaches often use a grid of control points which are moved to maximize a similarity measure between the images, and B-spline functions to model the deformations (e.g., [21]). Popular *elastic models* are based on the Navier equation of linear elasticity and consider the objects of interest in the images being elastic solids that deform under the application of external forces (e.g., [22]). *Fluid registration* methods are based on a viscous fluid model (e.g., [23]) and are able to cope with larger deformations, compared to elastic models. *Optical flow*-based registration approaches address the problem of registration as a motion problem and estimate the movement of pixels between the images (e.g., [24]).

2.1.2 Image Information

Registration schemes are distinguished into geometry-based and intensity-based, depending on the type of image information used to determine the searched transformation.

Geometry-based registration approaches are based on the alignment of salient geometric features in the images. These features can be sets of points (or landmarks), contours, or surfaces that are representative for the objects of interest. Depending on the type of the images, the features can be extracted automatically (e.g., salient points), or segmentation may be required (e.g., contours, surfaces). The extracted features are used to establish correspondences between the different images. Based on the determined correspondences, rigid registration approaches determine the transformation based on optimization schemes which minimize a distance measure between the corresponding sets of features. For example, the *iterative closest point* scheme [25] is often used for landmark-based approaches, or the *Chamfer matching* scheme [26] for binary structures. For non-rigid registration, deformable models can be used to compute the transforma-

tion for segmented structures such as curves or surfaces. Spline-based schemes are often employed for landmark-based non-rigid registration. The landmarks are used as control points on a non-uniform grid, and, for example, *thin-plate splines* (e.g., [27]) or *Gaussian elastic body splines* (e.g., [28]) can be used for matching corresponding landmarks, while the correspondences for the other image points are determined based on interpolation. The extracted set of features in geometry-based registration is sparse compared to the original image content, allowing for a relatively fast optimization process. The main problem of geometry-based registration is that the registration accuracy depends on the employed technique for feature extraction. Depending on the nature of the images, extracting features can be challenging, for example in microscopy images with high noise levels.

Intensity-based registration approaches directly exploit the intensity information of the images and match intensity patterns based on mathematical or statistical criteria. The transformation that aligns the target and the reference image is determined based on the minimization of intensity dissimilarity (or the maximization of a measure of intensity similarity). Dissimilarity measures include the *mean squared differences* of intensities (MSD), the *mean correlation coefficient* (CC), the *mutual information* (MI), or measures based on optic flow. Rigid intensity-based registration approaches often use the intensities to align the center of gravity and the principal directions of the two images (e.g., [29]). Non-rigid intensity-based registration is often formulated as an energy minimization problem. For the minimization problem a set of partial differential equations can be derived, which can be solved using the *finite difference* method [30], the *finite element* method [31], or the *variational* method [32]. The energy (or cost) function contains a similarity measure term and often an additional regularization term which imposes constrains on the computed transformation. These constraints can be defined by physical deformation models, such as elastic or fluid models. Alternatively, approaches based on *level sets* (e.g., [33]) or *optic flow* (e.g., [34]) can be used to compute

the transformation.

2.2 Optical Flow-Based Registration

Optical flow methods are used to determine the motion of objects between successive frames of image sequences. Since optical flow is based on the estimation of correspondences of points between different images, it is closely related to image registration. The correspondences are described by a displacement vector field and can be used to obtain the transformation between two frames. Optical flow estimation is based on the *intensity constancy assumption* which states that the intensity value of image points remains constant across successive frames, and is expressed for the 3D case by the general differential formulation of optical flow [35]:

$$I(x + u_x, y + u_y, z + u_z, t + \Delta t) = I(x, y, z, t), \tag{2.1}$$

where I denotes the image function and u_x, u_y, u_z are the x, y, z components of the image velocity or optical flow. Assuming that the motion between successive frames is small, first order Taylor expansion can be performed [35]:

$$\frac{\partial I}{\partial x}\frac{u_x}{\Delta t} + \frac{\partial I}{\partial y}\frac{u_y}{\Delta t} + \frac{\partial I}{\partial z}\frac{u_z}{\Delta t} + \frac{\partial I}{\partial t} = 0. \tag{2.2}$$

Often it is assumed that $\Delta t = 1$ for the time interval between the reference image f and the target image g, thus $\frac{\partial I}{\partial t} = g - f$. Eq. (2.2) can be rewritten as:

$$\nabla g \cdot \mathbf{u} + g - f = 0. \tag{2.3}$$

where $\nabla g = (\frac{\partial g}{\partial x}, \frac{\partial g}{\partial y}, \frac{\partial I}{\partial z})$ denotes the spatial intensity gradient of the image g, and $\mathbf{u} = (u_x, u_y, u_z)$ is the displacement vector field describing the optical flow. Eq. (2.2) is

not sufficient for computing a unique solution for the optical flow with three unknowns at each image position (*aperture problem*). To tackle the aperture problem and estimate the optical flow it is required to introduce additional constraints. In the following, we briefly describe the two main classes of optical flow approaches (i.e. global and local optical flow), as well as the demons algorithm which is also based on optical flow.

2.2.1 Global Optical Flow

Horn and Schunck [35] proposed to constrain the estimation of the optical flow by a global smoothness term (or regularization term). The problem was formulated by a global energy functional:

$$\int \left((\nabla g \cdot \mathbf{u} + g - f)^2 + \alpha |\nabla \mathbf{u}|^2 \right) dx\, dy\, dz, \tag{2.4}$$

where α denotes a *regularization parameter* which controls the influence of the smoothness term by penalizing large flow gradients ($|\nabla \mathbf{u}|^2 = |\nabla u_x|^2 + |\nabla u_y|^2 + |\nabla u_z|^2$). To minimize the functional in (2.4), the corresponding Euler-Lagrange equations are solved using the iterative Gauss-Seidel method. An advantage of the global formulation in (2.4) is that the smoothness term allows to estimate the optical flow even for image regions where the first term of (2.4) (*data term*) is zero or close to zero. This results in a dense displacement vector field (i.e. a vector is estimated for each image point), however, the method is sensitive to image noise. Extensions of the Horn/Schunck global optical flow approach [35] include approaches allowing discontinuities in the estimated optical flow field (e.g., [36], [37], [38]), or approaches allowing the estimation of optical flow for larger displacements (e.g., [39], [40], [41]).

2.2.2 Local Optical Flow

Lucas and Kanade [42] proposed a local optical flow approach to overcome the aperture problem. Based on the assumption that the unknown optical flow vector is constant within a local image neighborhood Ω, an overdetermined linear system of equations using (2.3) is proposed:

$$\sum_{x,y,z\in\Omega} W^2(x,y,z)\left(\nabla g\cdot\mathbf{u}+g-f\right)^2=0, \tag{2.5}$$

where $W(x,y,z)$ is a weighting function which gives more influence to pixels in the center of the neighborhood Ω. The optical flow vector $\mathbf{u}$ for the neighborhood Ω can be estimated using a least square minimization method:

$$\sum_{x,y,z\in\Omega}\left(\nabla g^T W^2(x,y,z)\nabla g\right)\mathbf{u}=\sum_{x,y,z\in\Omega}\nabla g^T W^2(x,y,z)(f-g). \tag{2.6}$$

The estimation of the optical flow is performed iteratively, by computing the current $\mathbf{u}_i$ at iteration i based on an additive rule:

$$\mathbf{u}_i=\mathbf{u}_{i-1}+d\mathbf{u}, \tag{2.7}$$

where $d\mathbf{u}$ is an *update vector field* which can be computed using (2.6), and $\mathbf{u}_{i-1}$ is the deformation vector field of the previous iteration. Note, that $\mathbf{u}_0$ is the zero vector field.

The advantage of local optical flow is the robustness to image noise, since information from a local spatial neighborhood is exploited for the computation of each vector [43]. However, the estimated vector field is sparse since one vector for each neighborhood Ω is computed [42]. To overcome this issue, a vector can be computed for each pixel of an image using (2.6). Extensions of the Lucas/Kanade local optical flow approach [42] include approaches based on the image gradient constancy for increasing the robustness to illumination changes (e.g., [44], [45]), approaches that use robust statistics (e.g., [46]),

or approaches using parametric models of higher order (e.g., [47]).

2.2.3 Demons

Thirion [34] introduced the *demons* algorithm for non-rigid image registration, based on the optical flow equations and inspired by Maxwell's demons in thermodynamics. The demons describe forces which reduce the differences between the reference and the target image, by moving image points according to local characteristics of the images. The estimation of the demons forces is similar to solving the optical flow equation (2.3):

$$\mathbf{u} = \frac{(f-g)\nabla g}{|\nabla g|^2 + (f-g)^2}. \tag{2.8}$$

The displacement vector field is computed iteratively (see (2.7)), and a Gaussian filter is used to regularize the displacement field. In [48] the demons approach was described as a global energy minimization problem, and in [49, 50] symmetric schemes of the demons have been proposed.

In general, using a local optical flow approach or a local demons-based approach is advantageous for the registration of dynamic live cell image data with local structural changes over time. Such local registration approaches can cope well with local deformations.

2.3 Diffeomorphic Registration

For biomedical applications it is advantageous to compute *diffeomorphic* transformations to preserve the topology of objects in the registered images, and to prevent foldings. Diffeomorphic registration approaches determine transformations which are invertible and the transformation as well as its inverse are smooth (continuously differentiable). Typically, diffeomorphic registration approaches require high computation times due to the

use of complex partial differential equations (e.g., [51, 52, 53]). In [54], a computationally efficient diffeomorphic registration approach based on the demons method was proposed. The approach combines the alternate optimization scheme of demons [50] with the Lie group structure on diffeomorphic transformations [55]. To ensure the diffeomorphism of a computed transformation at iteration i, the displacement vector field of the previous iteration is composed with the exponential map of an update stationary velocity field:

$$\mathbf{u}_i = \mathbf{u}_{i-1} \circ \exp\left(d\mathbf{v}\right), \tag{2.9}$$

where $d\mathbf{v}$ denotes the update velocity field, and the exponential map is efficiently determined based on the scaling and squaring method [56]. The diffeomorphic demons approach [54] was extended in [10] by computing the spatial transformation in the log-domain:

$$exp(\mathbf{v}_i) = \exp(\mathbf{v}_{i-1}) \circ \exp\left(d\mathbf{v}\right), \tag{2.10}$$

where $\mathbf{v}_i$ and $\mathbf{v}_{i-1}$ are the velocity vector fields in the log-domain for the iterations i and $i-1$, respectively, and the deformation vector field $\mathbf{u}_i$ can be determined by computing the exponential map of the respective velocity field, i.e., $\mathbf{u}_i = \exp\left(\mathbf{v}_i\right)$. This allows for an efficient computation of the inverse transformation, which can be determined by computing the exponent of the negative velocity vector field, i.e., $\mathbf{u}_i^{-1} = \exp(-\mathbf{v}_i)$.

2.4 Registration of Cells and Cell Nuclei in Live Microscopy Image Data

In this section, we review previous work on the registration of cells or cell nuclei in microscopy image data. We distinguish between rigid and affine, and non-rigid registration approaches.

2.4.1 Rigid and Affine Registration

Rieger et al. [57] proposed an approach for 3D rigid registration of cell nuclei in 3D confocal microscopy image sequences. The approach uses the spot channel of the image data and exploits the intensity information of labeled proteins located within the cell nucleus. The translation and the rotation of cell nuclei is determined based on the weighted center of mass and the principal axes of the inertia tensor of the intensity distribution of the labeled proteins.

A correlation-based approach has been developed by Wilson and Theriot [58] for rigid registration of cells in time-lapse phase-contrast microscopy image sequences. The task of estimating the rotation of cells between consecutive frames is converted to the task of estimating the translation of the 2D Fourier-transformed images. A polar transform to the magnitude spectrum of each transformed image is applied, and the translation (which describes the rotation in the original images) is computed based on cross-correlation. Cross-correlation is also used to compute the translation of cells between consecutive frames of the image sequences.

Sage et al. [59] used a model-based approach based on a least-squares fit of an ellipse and 2D segmentations of nuclear membranes to determine the translation of nuclei in time-lapse fluorescence microscopy image sequences. Each frame of an image sequence is registered w.r.t. a reference time point.

In Matula et al. [60], a point-based rigid registration of multiple cells in 3D time-lapse microscopy image sequences was presented. The approach is based on the matching of centroids of certain intracellular structures in consecutive frames of an image sequence. A 3D extension of the matching pairs support algorithm is used, and the rotation is assumed to occur only around the z-axis. The 3D transformation is determined by minimizing the mean-squared distances between the point sets of consecutive time points.

An approach for rigid 3D registration of cell nuclei in dynamic live cell microscopy image data was described in De Vos et al. [61]. The approach consists of two steps. In

the first step, the intensity weighted centres of mass of segmented nuclei are used to determine the translation, and the correlation coefficients of consecutive frames w.r.t. the centres of mass are used to determine the rotation. In the second step, the computed transformation is refined by utilizing the geometric centre of the 3D locations of telomeric dots.

Dzyubachyk et al. [62] introduced an affine shape-based approach for registration of cells in fluorescence microscopy images. The approach uses the maximum intensity projection images of 3D segmented cell shapes. The parameters for translation, rotation, and scaling are obtained by minimizing an energy functional based on distance functions between the nuclear shapes in consecutive frames of an image sequence. In addition, the energy functional can be extended by a deformation field which acts as a complement for the affine transformation.

In Kim et al. [63], an approach for rigid registration of live cells in 2D FRAP (Fluorescence Recovering After Photobleaching) image sequences was proposed. To cope with intensity changes after bleaching, registration is based on the minimization of the mutual information between cell nuclei using a regular step gradients descent optimizer.

Li et al. [64] proposed fitting the axes of an ellipse model to segmented nuclei for determining the rotation of multiple mitotic nuclei in laser scanning confocal microscopy image data. A similar approach was used in [65] for rigid registration of cells in dynamic image sequences. The two first components of a principal component analysis (PCA) of the intensities of segmented cells were used to determine translation and rotation.

In the context of multi-modal image registration, Klein et al. [66] registered confocal Raman microscopic images to immunofluorescence microscopy images of the same live cells. A rigid transformation is determined using the normalized mutual information between the intensity distribution of the immunofluorescence microscopy images, and the intensity distribution of PCA components of the Raman microscopic images.

In addition, other approaches for global registration of images containing cells or cell

nuclei have been described. For example, in Würflinger et al. [67], microscopy images of cell nuclei acquired using different stains were rigidly registered based on an intensity-based approach and the Powell minimization algorithm. Goobic et al. [68] proposed to compute the 2D translation in intravital video microscopy images of rolling leukocytes using a correlation-based approach. A phase-correlation based approach has been used in Kim et al. [69] to determine the translation in time-lapse confocal microscopy image sequences of live cells.

2.4.2 Non-Rigid Registration

Rigid registration approaches cannot cope with cell or nucleus deformations over time, affecting the accuracy of the movement analysis of subcellular particles. In the following, we review previous work on *non-rigid* registration of cells or cell nuclei in microscopy image data.

Mattes et al. [70] described a semi-automatic non-rigid registration approach for cell nuclei. Point sets which represent cell nuclei are interactively determined from two images of the same cell nucleus acquired at different time points, based on the confinement tree feature extraction method. The transformation is obtained by minimizing a cost functional based on the Euclidean distance between the two point sets. Optimization is performed using the Levenberg-Marquardt algorithm, and interpolation is performed using thin-plate splines.

In Yang et al. [71], a demons-based approach was presented for registration of 3D cell nuclei in live cell fluorescence microscopy image data. The approach was used to register different nuclei in static images, as well as the same nuclei in dynamic multi-channel image sequences. First, the cell nuclei are segmented using a global thresholding approach, and the images are smoothed using a Gaussian filter. Then, rigid registration is performed based on the normalized correlation coefficient and the regular gradient descent optimizer. For non-rigid registration, an extension of the demons approach with

symmetric forces was proposed. This extension uses the image gradients of both the reference and the target images to compute a displacement vector field:

$$\mathbf{u} = \frac{2(f-g)(\nabla f + \nabla g)}{|\nabla f + \nabla g|^2 + (f-g)^2}. \tag{2.11}$$

In contrast to the original demons formulation (2.8), the symmetric demons allows to compute a displacement vector at image locations with zero or close to zero values of the image gradient ∇g. To reduce the computation time, an adaptive step length optimization scheme as well as a coarse to fine multi-resolution scheme was used.

Kim et al. [11] proposed an intensity-based approach for non-rigid registration of cell nuclei in 2D and 3D dynamic live cell microscopy image data. The approach is based on the Lucas-Kanade optic flow algorithm, and minimizes the mean squared intensity differences between consecutive frames of an image sequence. The iterative Gauss-Newton optimization method is performed for each image point, providing dense deformation vector fields. The computed deformation fields are regularized using a Gaussian kernel, and an incremental scheme is used to compute deformation fields for each time point w.r.t. the first time point of an image sequence. In addition, three variants of the proposed approach have been introduced. First, a symmetric variant was proposed which uses the gradients of both the reference and the target image:

$$\sum_{x,y,z\in\Omega} (\nabla g + \nabla f)(\nabla g + \nabla f)^T \mathbf{U}/2 = \sum_{x,y,z\in\Omega} (\nabla g + \nabla f)(f-g), \tag{2.12}$$

where $\mathbf{U}$ denotes a vector of the displacement vector field $\mathbf{u}$. Second, a weighting approach based on the Levenberg-Marquardt optimization method was introduced:

$$\sum_{x,y,z\in\Omega} (\nabla g \nabla g^T + \mathbf{D})\mathbf{U} = \sum_{x,y,z\in\Omega} \nabla g(f-g), \tag{2.13}$$

where $\mathbf{D}$ is a diagonal matrix which depends on the similarity of the two image gradients

and controls the optimization process. Finally, the third symmetric weighting variant represents a combination of the symmetric and the weighting variants.

A contour-based non-rigid registration approach was proposed by De Vylder et al. [72] for registration of 2D cell nuclei in dynamic image sequences. First, the contours of cell nuclei are extracted from the segmented images. Then, the correspondences between contours in consecutive frames of an image sequence are established based on signatures which provide a description of the contours. The mapping is performed using a dynamic time warp algorithm defining the displacements of the nucleus boundary. The dense deformation field is determined by interpolating the displacements of the nucleus boundary points using thin-plate splines.

Sorokin et al. [73] presented a contour-based approach based on the Navier equation for non-rigid registration of 2D cell nuclei in dynamic image sequences. First, the cell nuclei in consecutive frames are registered using a rigid cross-correlation approach and the extracted contours of the nuclei. For non-rigid registration, correspondences between the two contours are established based on morphological contour matching and the generalized geodesic distance. Based on the computed displacements on the cell nuclei boundary, the Navier equation is used for modelling the nucleus deformation. The approach was extended in [74] with a dynamic elasticity model for forward simulation of nucleus motion and deformation. The contour matching process was embedded as a constraint into the system of equations describing the elastic behavior of the nucleus.

In general, intensity-based approaches are more suitable for the registration of nuclei in multi-channel image data, compared to contour-based or landmark-based approaches. Using the full intensity information of the nucleus channel generally allows to compute local deformations within cell nuclei with higher accuracy, compared to contour-based or landmark-based approaches which determine the deformation for the inner part of nuclei based on interpolation. On the other hand, contour-based or landmark-based registration approaches are advantageous for image data consisting of a single channel,

since stable landmarks on the contours of nuclei are used to determine the nucleus motion and deformation. In comparison, the determined transformations in intensity-based approaches may be influenced by the local motion of subcellular structures.

2.5 Non-Rigid Registration of Microscopy Image Data for other Biological Applications

Besides temporal registration of cells and cell nuclei as described in Sect. 2.4 above, non-rigid registration approaches for microscopy image data have also been used in other biological applications. In the following, we briefly describe representative approaches for different applications.

In the field of *cell nucleus shape modeling*, Rohde et al. [75] developed a diffeomorphic registration approach to compute deformations between cell nuclei in static or 2D time-lapse images. The registration approach combines the large deformation metric mapping with multi-dimensional scaling, and minimizes the geodesic distances between the segmented nuclei. Johnson et al. [76] used the former approach to additionally compute deformations between corresponding cells and nuclei, for constructing spatio-temporal models of cell and nuclear shape variation. Yoshizawa et al. [77] employed an interactive approach for non-rigid registration of the same nucleus in images acquired with different fluorescent markers. The registration uses features from segmented nuclei and the plasma membrane, and deformations are modeled by triharmonic radial basis functions.

To *detect cell division* in 2D dynamic confocal laser scanning microscopy image sequences, Tokuhisa and Kaneko [78] used a viscous fluid registration approach. A displacement vector field is determined between consecutive frames of an image sequence, and a similarity maximization step is used to cope with dividing nuclei.

To *track cells* in 2D dynamic phase-contrast microscopy image sequences, Hand et

al. [79] registered segmented cells using a symmetric local optical flow approach [80]. A deformation vector is computed for each node of a regular cubic grid placed across the image, and interpolation is performed using trilinear basis functions. A global optical flow approach has been used in Scherf et al. [81] to track cells in 2D time-lapse confocal microscopy image sequences of cell colonies. The approach minimizes the mean squared intensity differences between consecutive frames and the resulting partial differential equations are solved numerically using a fast Poisson solver.

For *3D reconstruction* of static fluorescence confocal microscopy image stacks of Drosophila muscles, Du and Wasser [82] introduced an intensity-based non-rigid registration approach using thin-plate splines. Allgeier et al. [83] reconstructed static 3D confocal laser scanning microscopy image data using a registration algorithm based on phase correlation. Hsu et al. [84] employed a non-rigid registration approach based on analytic robust point matching for the 3D reconstruction of vessels of rat brains in static histological microscopy images. For 3D reconstruction of static electron microscopy images, Akselrod-Ballin et al. [85] described a feature-based registration approach, and Saalfeld et al. [86] used a block-matching registration approach. Hogrebe et al. [87] introduced a landmark-based approach based on B-splines to register axons in 3D histological serial sections of fluorescence confocal microscopy image data. Lorenz et al. [88] employed an intensity-based registration approach using B-splines for 3D reconstruction and reduction of motion-induced artifacts in intravital images of living animals. In Wang et al. [89], a combined area-based and feature-based non-rigid registration approach has been described for 3D reconstruction of laser scanning microscope images and serial section transmission electron microscope images.

To *analyze gene expression data* in confocal microscopy images, Tomer et al. [90] described an intensity-based free-form non-rigid registration approach using third-order B-splines. For *atlas construction* of Drosophila brains in 3D laser scanning microscopy images, Peng et al. [91] introduced a landmark-based registration approach based on

thin-plate splines. The former approach was extended by a point-based rigid registration method in Qu et al. [92], for registration of images to atlas models of fruit fly brains. Fowlkes et al. [93] established a spatiotemporal gene expression atlas of Drosophila using a point-based registration approach based on segmented boundaries of cells or cell nuclei in two-photon microscopy image data.

For *motion estimation* of cells and tissue in 3D time-lapse laser scanning microscopy image data, Lombardot et al. [94] evaluated different registration approaches based on B-splines, a viscous fluid model, demons, and level-set optical flow. Pizarro et al. [95] applied a B-spline based free-form deformation approach as well as a combined local/global optical flow approach to estimate motion in dynamic light and electron microscopy image data. For *motion correction* in temporal microscopy image data of biological structures such as vessels, dendrites, and axons, Kumar et al. [96] proposed a point-based registration approach based on thin-plate splines.

2.6 Non-Rigid Registration of Temporal Medical Image Data

In medical image analysis, *temporal groupwise* registration approaches have been proposed, which simultaneously take into account all or multiple images of a dynamic image sequence. Most temporal groupwise registration approaches are based on the minimization of a dissimilarity metric between all frames of an image sequence and a reference frame (e.g., [97, 98, 99, 100, 101]). In [12, 102, 103, 104], group mean images were used as reference for temporal registration. Other approaches use dissimilarity metrics between all consecutive frames [105, 106], between all possible combinations of frames [107], or between all frames and a reference frame and simultaneously between consecutive frames [108, 109, 110]. In addition, several registration approaches consider all images of different dynamic image sequences simultaneously for the construction of a dynamic

atlas or for comparison of the different sequences (e.g., [111, 112, 113, 114, 115, 116, 117]).

Chapter 3

Non-Rigid Multi-Frame Registration

In this chapter, we present our non-rigid multi-frame approach for registration of cell nuclei in temporal microscopy image data. Previous approaches for non-rigid registration of cell nuclei or other biological structures in dynamic data (Section 2.4) are based on *pairwise* registration, where each frame of an image sequence is registered either to a chosen reference frame, or to the previous frame. Thus, pairwise registration decomposes the 2D+t or 3D+t registration task into multiple independent 2D or 3D registration tasks. However, to improve the accuracy of temporal registration, it is necessary to exploit additional information from the dynamic image sequences.

First, we describe the general incremental scheme of our non-rigid temporal registration approach. Then, we briefly review a previous pairwise consecutive registration scheme and subsequently introduce our multi-frame consecutive registration approach. We describe the used iterative registration scheme, and present three intensity-based variants of the multi-frame registration approach. We also investigate two different temporal weighting schemes for the multi-frame approach. The work in this chapter was published in Tektonidis et al. [118].

3.1 Incremental Temporal Registration Scheme

Our non-rigid multi-frame registration approach is based on an incremental scheme, where each image g_k of an image sequence at time point $k \geq 2$ is registered to the reference image g_1 at the first time point. First, the transformation of the image g_k to the image g_{k-1} is computed and represented by a dense deformation vector field $\mathbf{u}(g_k, g_{k-1})$. Then, the transformation of g_k to g_1 is obtained by concatenating $\mathbf{u}(g_k, g_{k-1})$ and $\mathbf{u}(g_{k-1}, g_1)$:

$$\mathbf{u}(g_k, g_1) = G * \left(\mathbf{u}\left(g_k, g_{k-1}\right)(\mathbf{x}) + \mathbf{u}\left(g_{k-1}, g_1\right)\left(\mathbf{T}\left(\mathbf{x}, \mathbf{u}_{k,k-1}\right)\right)\right), \tag{3.1}$$

where $\mathbf{T}\left(\mathbf{x}, \mathbf{u}_{k,k-1}\right) = \mathbf{T}\left(\mathbf{x}, \mathbf{u}\left(g_k, g_{k-1}\right)\right)$ denotes the transformation using the deformation vector field $\mathbf{u}\left(g_k, g_{k-1}\right)$, and $\mathbf{x} = (x, y)$ is the spatial coordinate. The vector field $\mathbf{u}(g_{k-1}, g_1)$ is computed analogously (recursively), $\mathbf{u}(g_1, g_1)$ is a zero vector field, and G represents a Gaussian kernel for regularization of the vector fields.

3.2 Pairwise Consecutive Registration Scheme

Pairwise registration approaches for cell images estimate for each time point k the deformation vector field $\mathbf{u}(g_k, g_{k-1})$ by exploiting the information from two consecutive images g_{k-1} and g_k (e.g., [11]). The image g_k is registered to the previous image g_{k-1} by computing the deformation vector field $\mathbf{u}(g_k, g_{k-1})$ which minimizes a similarity metric S (e.g., squared intensity differences, normalized cross correlation) between the two images:

$$S\left(g_k\left(\mathbf{T}\left(\mathbf{x}, \mathbf{u}_{k,k-1}\right)\right), g_{k-1}\left(\mathbf{x}\right)\right) \tag{3.2}$$

where $g_k\left(\mathbf{T}\left(\mathbf{x}, \mathbf{u}_{k,k-1}\right)\right)$ is the image at time point k warped with the currently estimated $\mathbf{u}(g_k, g_{k-1})$. Note, that since we use a local registration approach, pixelwise minimization of the similarity metric is performed.

3.3 Multi-Frame Consecutive Registration Scheme

In our multi-frame registration approach, we estimate for each time point k the deformation vector field $\mathbf{u}(g_k, g_{k-1})$ by exploiting the information from $N \geq 3$ consecutive images of an image sequence simultaneously. The image g_k is registered simultaneously to the $N-1$ warped previous images, for which the transformations have been computed in previous time steps. Note, however, that $N-1$ previous images are available only for $k \geq N$. Generally, for a time point k, the temporal range of available previous images g_l is given by $\max(k-N+1, 1) \leq l \leq k-1$, and the number of the available previous images is $N_l = \min(N-1, k-1)$.

Since the searched vector field $\mathbf{u}(g_k, g_{k-1})$ describes the transformation between the coordinate systems of g_k and g_{k-1}, the N_l previous images g_l have to be warped into the coordinate system of g_{k-1}. For warping, a vector field $\mathbf{u}(g_l, g_{k-1})$ is required, which can be determined by combining vector fields that have been computed for images at previous time points. For example, to determine $\mathbf{u}(g_{k-3}, g_{k-1})$ for warping g_{k-3}, we concatenate the vector fields $\mathbf{u}(g_{k-2}, g_{k-3})$ and $\mathbf{u}(g_{k-1}, g_{k-2})$, and compute the inverse of the resulting vector field (see also Section 5.2.1 below). In general, each image g_l is warped using the following vector field:

$$\mathbf{u}(g_l, g_{k-1}) = G * \mathbf{u}^{-1}\left(g_{k-1}, g_l\right), \tag{3.3}$$

where $\mathbf{u}\left(g_{k-1}, g_l\right)$ is calculated recursively using computed vector fields of previous time points. Note, that the regularization of the deformation vector fields with a Gaussian kernel G can be interpreted as an approximation to elastic deformations [48]. The inverse vector field $\mathbf{u}^{-1}\left(g_{k-1}, g_l\right)$ in (3.3) is computed as follows. For each pixel of an image we determine a number of vectors (we used three vectors) of the original vector field which point closest to the pixel. Then, the weighted average of these vectors is computed (using the Euclidean distance as weight) and its negative vector is used as

inverse vector for this pixel. Note, that $\mathbf{u}(g_{k-1}, g_{k-1})$ is a zero vector field, and therefore the image g_{k-1} is not warped.

The multi-frame consecutive registration approach computes the deformation vector field $\mathbf{u}(g_k, g_{k-1})$ which minimizes for each time point k the sum of a similarity metric S between the image g_k and the images $g_l^\star$:

$$\frac{1}{N_l} \sum_l S\left(g_k\left(\mathbf{T}\left(\mathbf{x}, \mathbf{u}_{k,k-1}\right)\right), g_l^\star\right), \tag{3.4}$$

where

$$g_l^\star = g_l\left(\mathbf{T}\left(\mathbf{x}, \mathbf{u}_{l,k-1}\right)\right) \tag{3.5}$$

denotes the previous image at time point l warped using $\mathbf{u}(g_l, g_{k-1})$ (3.3). Note, that also in (3.4) pixelwise minimization of the similarity metric is performed. A diagram of the multi-frame consecutive registration approach is shown in Fig. 3.1, which gives an overview of the use of the different deformation vector fields and images.

An advantage of our consecutive incremental registration approach is that multiple successive images are registered and that the intensity similarity measure is computed between time points within a certain time range of an image sequence. Thus, strong changes in shape and intensity structure over the entire image sequence (e.g., due to nuclear envelope breakdown or photobleaching) can be coped better with compared to computing the similarity measure between time points that are very far apart (e.g., first and last time point of an image sequence). Note that with our consecutive registration approach only the information of previous time points is used since only for those time points transformations have been computed. The information from later time points cannot be used since the transformations have not yet been computed.

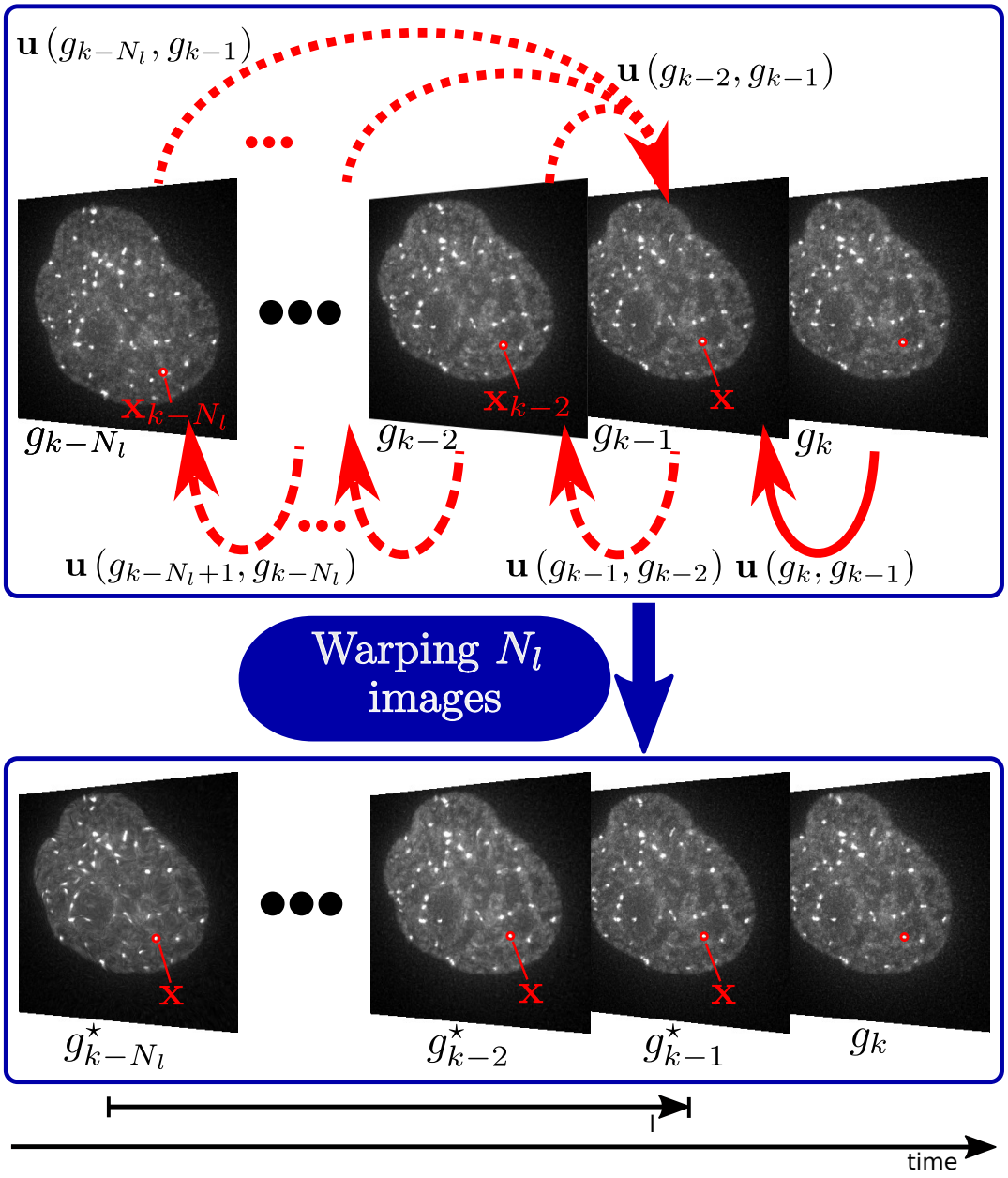

Figure 3.1: Diagram of the multi-frame consecutive registration approach. The searched transformation $\mathbf{u}(g_k, g_{k-1})$ (red solid arrow) is computed based on information from multiple consecutive images. In the upper part of the diagram, the location of an example image point (red dot) has been marked at different consecutive time points. The example point has different coordinates at the different time points. Warping of the previous N_l images is performed using vector fields (dotted arrows) that are determined based on the vector fields computed at previous time points (dashed arrows). After warping, the spatial coordinates of the example image point are the same in all warped previous images $g_l^\star$ (lower part of diagram).

3.4 Iterative Registration Scheme

To compute the searched deformation vector field $\mathbf{u}(g_k, g_{k-1})$ in (3.4) we use an iterative scheme. At each iteration i the current $\mathbf{u}_i(g_k, g_{k-1})$ is updated by:

$$\mathbf{u}_i(g_k, g_{k-1}) = G * (\mathbf{u}_{i-1}(g_k, g_{k-1}) + G * d\mathbf{u}_i(g_k^*, g_{k-1})), \tag{3.6}$$

where

$$g_k^* = g_k(\mathbf{T}(\mathbf{x}, \mathbf{u}_{i-1}(g_k, g_{k-1}))) \tag{3.7}$$

is the transformed image at time point k using the vector field from the previous iteration $i-1$, and $d\mathbf{u}_i(g_k^*, g_{k-1})$ is an update field (see Section 3.5 below). For regularization of the vector fields a Gaussian kernel G is used. The initial vector field $\mathbf{u}_0(g_k, g_{k-1})$ is the zero vector field. The iteration terminates either when a certain number of iterations is reached or when the sum of the similarity metric in (3.4) is below a threshold value.

3.5 Intensity-Based Non-Rigid Multi-Frame Registration

For minimizing the similarity metric in (3.4), we introduce three intensity-based variants of the non-rigid multi-frame registration approach, which are based on local optic flow estimation. In general, a local optical flow registration approach is advantageous in our application since many local structural changes occur within cell nuclei in the live cell microscopy data. For image data of cell nuclei going into mitosis, additional local structural changes occur due to, for example, the nuclear envelope breakdown or the disappearance of nucleoli. A local registration approach can generally better cope with local deformations compared to global optical flow approaches.

3.5.1 Weighting Approach

The first variant of the multi-frame approach is an extension of the pairwise weighting approach in [11]. The *pairwise weighting* approach has been previously used for registration of microscopy images and it performed better than other optic flow based registration approaches, for example, symmetric Demons [71] and Lucas-Kanade [11, 43]. The pairwise weighting approach minimizes for each image point the squared intensity differences between pairs of successive images. In our *multi-frame weighting* approach, we minimize for each time point k and for each image point $\mathbf{x}_c$ the sum of squared intensity differences between the image g_k^* in (3.7) and the N_l previous warped images $g_l^\star$ in (3.5) over a spatial neighborhood region Ω around each pixel $\mathbf{x}_c$:

$$\min_{\mathbf{U}} \sum_{\mathbf{x}\in\Omega} \frac{1}{N_l} \sum_{l} \left[g_k^* \left(\mathbf{x} + \mathbf{U} \right) - g_l^\star \left(\mathbf{x} \right) \right]^2 , \tag{3.8}$$

where $\mathbf{U}$ denotes the vector of the update field $d\mathbf{u}_i \left(g_k^*, g_{k-1} \right)$ at position $\mathbf{x}_c$, and a Gaussian function is used to emphasize image points at the center of the neighborhood Ω. Note, that a *local* transformation model $\mathbf{x} + \mathbf{U}$ is used since the optimization is performed separately for each pixel $\mathbf{x}_c$, and that considering a neighborhood region imposes spatial smoothness [42]. The squared intensity differences in (3.8) correspond to the similarity metric S in (3.4). The non-linear formulation in (3.8) can be linearized by performing a first order Taylor expansion:

$$\min_{\mathbf{U}} \sum_{\mathbf{x}\in\Omega} \frac{1}{N_l} \sum_{l} \left[g_k^* + \nabla g_k^{*T} \mathbf{U} - g_l^\star \right]^2 . \tag{3.9}$$

Note, that g_k^*, ∇g_k^*, and $g_l^\star$ are evaluated at coordinate $\mathbf{x}$. Minimization of (3.9) yields the following system of linear equations:

$$\sum_{\mathbf{x}\in\Omega} \frac{1}{N_l} \sum_{l} \left(\nabla g_k^* \nabla g_k^{*T} \right) \mathbf{U} = \sum_{\mathbf{x}\in\Omega} \frac{1}{N_l} \sum_{l} \nabla g_k^* \left(g_l^\star - g_k^* \right) . \tag{3.10}$$

from which $\mathbf{U}$ can be determined. The gradient ∇g_k^* is determined using a four point central difference scheme, and the terms on both sides of (3.10) are weighted with the Euclidean norm $\|\nabla g_k^*\|$ to emphasize image points with strongly changing intensity ([43]).

In the pairwise weighting approach [11] an extension of the Lucas-Kanade optic flow approach [42, 43] was used, which includes a weighting matrix and performs an optimization similar to the method of Levenberg-Marquardt (e.g., [119]). Analogously to [11], we introduce a weighting matrix $\mathbf{D}_l$ in the multi-frame registration approach defined in (3.10):

$$\sum_{\mathbf{x}\in\Omega} \frac{1}{N_l} \sum_l \left(\nabla g_k^* \nabla g_k^{*T} + \mathbf{D}_l\right) \mathbf{U} = \sum_{\mathbf{x}\in\Omega} \frac{1}{N_l} \sum_l \nabla g_k^* \left(g_l^\star - g_k^*\right), \tag{3.11}$$

where $\mathbf{D}_l$ is a diagonal matrix which indicates whether the current estimate of $\mathbf{U}$ is close to the solution or not. The elements of the matrix are given by:

$$\mathbf{D}_{l,nn} = c\, w_l(\mathbf{x}) \left(\frac{\partial g_k^*}{\partial x_n}\right)^2, \tag{3.12}$$

where c is a constant (in our experiments we used $c = 1.0$). The weighting function $w_l(\mathbf{x})$ is computed for each pixel $\mathbf{x}$ by:

$$w_l(\mathbf{x}) = \frac{\left(\|\nabla g_l^\star\| - \|\nabla g_k^*\|\right)^2}{2\left(\|\nabla g_l^\star\|^2 + \|\nabla g_k^*\|^2\right)} + \frac{\left|\arccos\left(\frac{\nabla g_l^\star \nabla g_k^*}{\|\nabla g_l^\star\| \|\nabla g_k^*\|}\right)\right|}{2\pi}, \tag{3.13}$$

and quantifies the similarity between the image g_k^* and each image $g_l^\star$ on the basis of the image gradient magnitude (first term) and the gradient orientation (second term). For identical gradients, the weight $w_l(\mathbf{x})$ is zero and for dissimilar gradients, $w_l(\mathbf{x})$ is close to one.

The motivation for using the weighting function $w_l(\mathbf{x})$ in (3.11), (3.12) is as follows. The linear approximation $g_k^*(\mathbf{x} + \mathbf{U}) \approx g_k^*(\mathbf{x}) + \nabla g_k^{*T}(\mathbf{x})\,\mathbf{U}$ in (3.9) is generally good for relatively small magnitude values of $\mathbf{U}$. However, since higher order terms are

neglected, the approximation may not be good for large magnitude values of $\mathbf{U}$ and the solution in (3.10) can be subject to errors. In comparison, depending on the values of the matrix $\mathbf{D}_l$ at each iteration in (3.11), the Levenberg-Marquardt method switches between the Gauss-Newton method (i.e. the linear approximation used in the Lucas-Kanade approach) and the steepest-descent method to improve the result. If the current estimate is close to the solution (i.e. the magnitude value of $\mathbf{U}$ is small), the values of $\mathbf{D}_l$ are small (since the values of $w_l(\mathbf{x})$ are small), and (3.11) becomes more similar to the original formulation in (3.10). Otherwise, the values of $\mathbf{D}_l$ are larger and the steepest-descent method is used.

3.5.2 Symmetric Approach

The second variant of the multi-frame approach is based on the pairwise symmetric approach [11], which exploits the image gradient of both images g_k^* and g_{k-1} and allows to compute $\mathbf{U}$ in image regions where at least one of the image gradients ∇g_k^* and ∇g_{k-1} is not a zero vector (or not close to a zero vector). Note, that using the image gradient of both images is analogous to symmetric schemes for the demons approach (Thirion [34], Yang et al. [49], Vercauteren et al. [50]). The *multi-frame symmetric* approach exploits the gradients of the image at time point k and also the gradients of the previous N_l images, and is based on the minimization problem:

$$\min_{\mathbf{U}} \sum_{\mathbf{x}\in\Omega} \frac{1}{N_l} \sum_{l} \left[g_k^* \left(\mathbf{x} + \frac{\mathbf{U}}{2} \right) - g_l^\star \left(\mathbf{x} - \frac{\mathbf{U}}{2} \right) \right]^2 . \tag{3.14}$$

A linear expansion of (3.14) yields:

$$\min_{\mathbf{U}} \sum_{\mathbf{x}\in\Omega} \frac{1}{N_l} \sum_{l} \left[g_k^* + \nabla g_k^{*T} \frac{\mathbf{U}}{2} - g_l^\star + \nabla g_l^{\star T} \frac{\mathbf{U}}{2} \right]^2 . \tag{3.15}$$

Minimization of (3.15) leads to a linear system of equations which includes the gradients of the image g_k^* and the gradients of the images $g_l^\star$:

$$\sum_{\mathbf{x}\in\Omega} \frac{1}{N_l} \sum_l \left(\nabla g_l^\star + \nabla g_k^*\right) \left(\nabla g_l^\star + \nabla g_k^*\right)^T \frac{\mathbf{U}}{2} = \sum_{\mathbf{x}\in\Omega} \frac{1}{N_l} \sum_l \left(\nabla g_l^\star + \nabla g_k^*\right) \left(g_l^\star - g_k^*\right). \quad (3.16)$$

The multi-frame symmetric approach allows to compute $\mathbf{U}$ when at least one of the gradients ∇g_k^* or $\nabla g_l^\star$ is not a zero vector (or not close to a zero vector). Thus, the larger the number of frames N used by the multi-frame approach, the more likely is that at least one of the N used image gradients is not a zero vector, and that a solution for $\mathbf{U}$ can be computed.

3.5.3 Symmetric Weighting Approach

The third variant of the multi-frame approach combines the weighting approach with the symmetric approach described above. The vector $\mathbf{U}$ in the *multi-frame symmetric weighting* approach is obtained by:

$$\sum_{\mathbf{x}\in\Omega} \frac{1}{N_l} \sum_l \left(\left(\nabla g_l^\star + \nabla g_k^*\right) \left(\nabla g_l^\star + \nabla g_k^*\right)^T + \mathbf{D}_l \right) \frac{\mathbf{U}}{2} = \sum_{\mathbf{x}\in\Omega} \frac{1}{N_l} \sum_l \left(\nabla g_l^\star + \nabla g_k^*\right) \left(g_l^\star - g_k^*\right), \quad (3.17)$$

with

$$\mathbf{D}_{l,nn} = c\, w_l(\mathbf{x}) \left(\frac{\partial g_k^*}{\partial x_n} + \frac{\partial g_l^\star}{\partial x_n} \right)^2, \quad (3.18)$$

where c is a constant (we used $c = 1.0$) and $w_l(\mathbf{x})$ is defined as in (3.13).

3.6 Temporal Weighting

In the proposed multi-frame registration approach, the image g_k is simultaneously registered to the N_l previous warped images $g_l^\star$ of an image sequence. To compute the deformation vector field $\mathbf{u}(g_k, g_{k-1})$, each image $g_l^\star$ contributes equally. However, generally it is advantageous to control the influence of each image $g_l^\star$ on the registration result. To this end, we compute a temporal weight W_l for each $g_l^\star$, and use the normalized weight $\overline{W}_l = W_l / \sum_l W_l$. For the multi-frame weighting approach we then have:

$$\sum_{\mathbf{x}\in\Omega} \sum_l \overline{W}_l \left(\nabla g_k^* \nabla g_k^{*T} + \mathbf{D}_l \right) \mathbf{U} = \sum_{\mathbf{x}\in\Omega} \sum_l \overline{W}_l \nabla g_k^* \left(g_l^\star - g_k^* \right), \tag{3.19}$$

which is an extension of (3.11). The extension for the two other variants of the multi-frame approach in (3.16), (3.17) is analogous. The weights W_l can be defined based on different criteria. In the following we describe two different possibilities for choosing W_l.

3.6.1 Temporal Distance

In the first temporal weighting scheme, we exploit the temporal distance between the time points l and the time point k. For example, the influence of image $g_{k-1}^\star$ is larger than for $g_{k-2}^\star$, thus $W_{k-1} > W_{k-2}$. This is meaningful if we assume that an image $g_l^\star$ at a time point closer to k is more similar to g_k^* than an image $g_l^\star$ at a more distant time point. Additionally, the computed deformation vector field for an image $g_l^\star$ at a time point closer to k represents a relatively small deformation, and can be considered to be more reliable. To determine the temporal weights we used a Gaussian function, which within the range $[k - N_l, k - 1]$ takes its maximum value at $k - 1$ and its minimum value at $k - N_l$:

$$W_l = \frac{1}{\sqrt{2\pi} N_l} e^{-\frac{(l-(k-1))^2}{2N_l^2}}. \tag{3.20}$$

3.6.2 Image Similarity

The second temporal weighting scheme is based on the similarity of the images $g_l^\star$ and the image g_k^*. As image similarity measure we use the mean Euclidean norm of the differences of the image gradients between g_k^* and each $g_l^\star$. The temporal weights are defined as follows:

$$W_l = \frac{1}{\frac{1}{n}\sum_{\mathbf{x}} \|\nabla g_l^\star - \nabla g_k^*\|^\alpha}, \tag{3.21}$$

where n denotes the total number of pixels in an image and the exponent $\alpha \in \mathbb{N}$ controls the strength of the image similarity (we used $\alpha = 4$). The difference to computing the weights in (3.20) is that the weights in (3.21) are computed at each iteration i since the image g_k^* is updated in (3.7) and thus requires longer computation times.

Chapter 4

Diffeomorphic Non-Rigid Multi-Frame Registration

In this chapter, we describe our diffeomorphic multi-frame approach for non-rigid registration of cell nuclei in 2D and 3D live cell fluorescence microscopy images. A diffeomorphic approach has the advantage that the determined transformations are invertible and smooth. First, we give an overview of our approach. Then, we introduce the multi-frame registration scheme based on a temporally weighted mean image. We describe the employed iterative log-domain diffeomorphic registration scheme as well as two intensity-based weighting approaches based on local optic flow estimation. Finally, we present the used flow boundary preserving method for regularization of the deformation vector fields. The work in this chapter was published in [120].

4.1 Overview of the Approach

An overview of our diffeomorphic multi-frame non-rigid registration approach is given in Fig. 4.1. In our approach, each image g_k of an image sequence at time point $k \geq 2$ is registered to the reference image g_1 at the first time point using the *diffeomorphic* transformation $\phi_{k,1}$ which is determined based on an incremental temporal registration

Figure 4.1: Diagram of the diffeomorphic multi-frame non-rigid registration approach. First, for registration of an image g_k at time point k the temporally weighted mean image $\overline{g}^{\star}_{k-1}$ is determined based on multiple consecutive images g_l and the previously computed inverse transformations $\phi^{-1}_{l+1,l}$. Then, the temporal mean image and the image g_k are used for computing the transformation $\phi_{k,k-1}$. The computation is performed iteratively, using a log-domain diffeomorphic scheme combined with an intensity-based approach, where $d\mathbf{v}^{(i)}_{k,k-1}$ is an update vector field. Finally, the computed transformation $\phi_{k,k-1}$ is used to determine the transformation $\phi_{k,1}$ to the first image.

scheme:

$$\phi_{k,1} = \phi_{k,k-1} \circ \phi_{k-1,1}, \tag{4.1}$$

where the transformation $\phi_{k-1,1}$ is computed analogously (recursively). The diffeomorphic transformation $\phi_{k,k-1}$ is determined by exploiting the information from $N \geq 3$ consecutive frames simultaneously, and can be described by a deformation vector field $\mathbf{u}_{k,k-1}$ which is added to the identity transformation, i.e., $\phi_{k,k-1} : \mathbf{x} \mapsto \mathbf{x} + \mathbf{u}_{k,k-1}(\mathbf{x})$. We determine $\phi_{k,k-1}$ using a temporally weighted mean image $\overline{g}^{\star}_{k-1}$ (see Section 4.2 below) based on the previous $N-1$ consecutive images (g_{k-N+1}, ..., g_{k-1}) and a log-domain diffeomorphic method [10] which allows efficient computation of the inverse transformation $\phi^{-1}_{k,k-1}$. This method uses a Lie group structure [55] which defines an exponential mapping from the vector space of smooth velocity fields to diffeomorphisms. Thus, the diffeomorphic transformation $\phi_{k,k-1}$ can be defined as an exponential of a smooth *stationary velocity vector field* $\mathbf{v}_{k,k-1}$ in the log-domain, i.e., $\phi_{k,k-1} = \exp(\mathbf{v}_{k,k-1})$, and the inverse transformation is given by $\phi^{-1}_{k,k-1} = \exp(-\mathbf{v}_{k,k-1})$. The velocity field $\mathbf{v}_{k,k-1}$ is determined iteratively based on an update velocity field $d\mathbf{v}^{(i)}_{k,k-1}$ (see Section 4.3 below). Finally, the determined $\phi_{k,1}$ is regularized using the corresponding deformation vector field:

$$\mathbf{u}_{k,1} \leftarrow F * \mathbf{u}_{k,1}, \tag{4.2}$$

where F is the flow boundary preserving operator (see Section 4.5 below).

4.2 Multi-Frame Non-Rigid Registration Using a Temporally Weighted Mean Image

To compute the diffeomorphic transformation $\phi_{k,k-1}$ in (4.1), the image g_k is registered to the temporally weighted mean image determined from the $N-1$ previous images which have been transformed using the computed inverse transformations from previous time

steps. Note, that for $k < N$ the temporally weighted mean image is determined based on the $k-1$ previous images. For a time point k, the temporal range of available previous images g_l is given by $\max(k-N+1,1) \leq l \leq k-1$, and the number of the available previous images is given by $N_l = \min(N-1, k-1)$. The required transformations can be computed recursively by composing the inverse transformations from previous time points:

$$\phi_{l,k-1} = \phi_{l+1,l}^{-1} \circ \phi_{l+1,k-1}, \tag{4.3}$$

where $\phi_{l+1,l}^{-1}$ denotes the inverse transformation for the image at time point $l+1$, and $\phi_{l+1,k-1}$ is computed analogously (recursively). Note, that $\phi_{l,k-1}$ is diffeomorphic since it is a composition of diffeomorphic transformations. The computed transformation is regularized using the corresponding deformation vector field $\mathbf{u}_{l,k-1}$:

$$\mathbf{u}_{l,k-1} \leftarrow F * \mathbf{u}_{l,k-1}, \tag{4.4}$$

where F is the flow boundary preserving operator (see Section 4.5 below). The temporally weighted mean image is given by:

$$\overline{g}_{k-1}^{\star} = \sum_l \overline{W}_l \left(g_l \circ \phi_{l,k-1} \right), \tag{4.5}$$

where $g_l \circ \phi_{l,k-1}$ denotes the image at time point l transformed with $\phi_{l,k-1}$ and $\overline{W}_l$ is a normalized weight factor which controls the influence of the previous images on the registration result. We determine the weights W_l using a Gaussian function and based on the temporal distance between the time points l and k:

$$W_l = \frac{1}{\sqrt{2\pi} N_l} e^{-\frac{(l-(k-1))^2}{2N_l^2}}. \tag{4.6}$$

The Gaussian function takes its maximum at $k-1$ and its minimum at $k-N_l$ within the range $[k-N_l, k-1]$. A weighted mean image based on diffeomorphic transformations has been also used for temporal groupwise registration of medical images (e.g., Lombaert et al. [121]). Note, that the temporal weighting scheme in (4.5) is analogous to the temporal weighting scheme used in the non-diffeomorphic multi-frame registration approach (see Section 3.6).

We compute the transformation $\phi_{k,k-1}$ by minimizing for each time point k and for each image point $\mathbf{x} = (x, y)$ or $\mathbf{x} = (x, y, z)$ the sum of squared intensity differences between the image g_k and the temporally weighted mean image $\overline{g}^{\star}_{k-1}$ in (4.5) within a neighborhood region Ω:

$$\sum_{\mathbf{x}\in\Omega} \left(\left(g_k \circ \phi_{k,k-1}\right)(\mathbf{x}) - \overline{g}^{\star}_{k-1}(\mathbf{x}) \right)^2 \tag{4.7}$$

where $g_k \circ \phi_{k,k-1}$ denotes the image at time point k transformed with the searched transformation $\phi_{k,k-1}$.

Note that our diffeomorphic multi-frame approach has several main differences to the non-diffeomorphic multi-frame approach in Chapter 3. First, according to (4.7) we compute the sum of squared intensity differences only between the image g_k at time point k and the temporal mean image $\overline{g}^{\star}_{k-1}$, whereas in (3.4) the sum of squared intensity differences are computed between $N-1$ pairs of consecutive images (g_k and each $g_l \circ \phi_{l,k-1}$). This reduces the computation time significantly and allows application to 3D image data. Second, our diffeomorphic multi-frame approach employs diffeomorphic transformations compared to the multi-frame approach in Chapter 3 which guarantees that the transformations as well as the compositions of transformations in (4.3) are smooth and invertible.

4.3 Computation of the Diffeomorphic Velocity Vector Field

The velocity vector field $\mathbf{v}_{k,k-1}$ used for determining the diffeomorphic transformation $\phi_{k,k-1}$ in (4.1) is computed iteratively in the log-domain. At each iteration i the current $\mathbf{v}_{k,k-1}^{(i)}$ is updated by [10]:

$$\mathbf{v}_{k,k-1}^{(i)} = F * \left(Z \left(\mathbf{v}_{k,k-1}^{(i-1)}, G * d\mathbf{v}_{k,k-1}^{(i)} \right) \right), \tag{4.8}$$

where $d\mathbf{v}_{k,k-1}^{(i)}$ is an *update vector field* for the transformation between the image $g_k^* = g_k \circ \exp\left(\mathbf{v}_{k,k-1}^{(i-1)}\right)$ and the temporal mean image $\overline{g}_{k-1}^{\star}$ (4.5), and G is a Gaussian kernel for regularization of the update field. The employed update scheme ensures that the computed transformation is diffeomorphic in contrast to the additive [42] or the compositive [122] update scheme. $Z\left(\mathbf{v}_{k,k-1}^{(i-1)}, G*d\mathbf{v}_{k,k-1}^{(i)}\right)$ denotes a velocity vector field such that:

$$\exp(Z(\mathbf{v}, d\mathbf{v})) \approx \exp(\mathbf{v}) \circ \exp(d\mathbf{v}), \tag{4.9}$$

where for simplicity $\mathbf{v} = \mathbf{v}_{k,k-1}^{(i-1)}$ and $d\mathbf{v} = G*d\mathbf{v}_{k,k-1}^{(i)}$. This velocity vector field is determined using the Baker-Campbell-Hausdorff formula [123]:

$$Z(\mathbf{v}, d\mathbf{v}) = \mathbf{v} + d\mathbf{v} + \frac{1}{2}\left[\mathbf{v}, d\mathbf{v}\right] + \frac{1}{12}\left[\mathbf{v}, \left[\mathbf{v}, d\mathbf{v}\right]\right], \tag{4.10}$$

where the Lie bracket $[\mathbf{v}, d\mathbf{v}]$ represents a vector field at each position $\mathbf{x}$:

$$[\mathbf{v}, d\mathbf{v}](\mathbf{x}) = \mathrm{Jac}(\mathbf{v})(\mathbf{x})\; d\mathbf{v}(\mathbf{x}) - \mathrm{Jac}(d\mathbf{v})(\mathbf{x})\; \mathbf{v}(\mathbf{x}), \tag{4.11}$$

where Jac denotes the Jacobian of the respective vector field. The iteration terminates either when a certain number of iterations is reached or when the sum of squared intensity differences in (4.7) is below a threshold value.

4.4 Intensity-Based Non-Rigid Diffeomorphic Multi-Frame Registration based on Local Optic Flow

For minimizing the sum of squared intensity differences in (4.7), we use two local intensity-based optimization variants of the non-rigid diffeomorphic multi-frame registration approach.

4.4.1 Weighting Approach

The first variant is based on a local *weighting* optimization scheme which was previously used in our non-diffeomorphic approach described in Chapter 3 above [118, 124]. In our *diffeomorphic multi-frame weighting* approach, we minimize for each image point $\mathbf{x}_c$ of an image the sum of squared intensity differences between the image $g_k^* = g_k \circ \exp\left(\mathbf{v}_{k,k-1}^{(i-1)}\right)$ and the temporally weighted mean image $\overline{g}_{k-1}^{\star}$ within the neighborhood region Ω. The approach includes a weighting matrix and performs an optimization similar to the method of Levenberg-Marquardt (e.g., [119]). The optimization is performed for each time point k over the neighborhood region Ω around each voxel $\mathbf{x}_c$ of an image, where a vector $\mathbf{V}$ at the position $\mathbf{x}_c$ of the update vector field $d\mathbf{v}_{k,k-1}^{(i)}$ (4.8) in the log-domain is computed by:

$$\sum_{\mathbf{x}\in\Omega} \left(\nabla g_k^* \nabla g_k^{*T} + \mathbf{D}\right) \mathbf{V} = \sum_{\mathbf{x}\in\Omega} \nabla g_k^* \left(\overline{g}_{k-1}^{\star} - g_k^*\right), \tag{4.12}$$

where ∇g_k^* denotes the gradient of the image g_k^* at voxel $\mathbf{x}$, and the weighting matrix $\mathbf{D}$ is a diagonal matrix which indicates whether the current estimate of $\mathbf{V}$ is close to the solution or not. The elements of $\mathbf{D}$ are given by:

$$\mathbf{D}_{nn} = c\, w(\mathbf{x}) \left(\frac{\partial g_k^*}{\partial x_n}\right)^2, \tag{4.13}$$

where c is a constant (in our experiments we used $c = 1.0$). The weighting function $w(\mathbf{x})$ is computed for each pixel $\mathbf{x}$ by:

$$w(\mathbf{x}) = \frac{\left(\|\nabla \overline{g}^{\star}_{k-1}\| - \|\nabla g^{*}_{k}\|\right)^2}{2\left(\|\nabla \overline{g}^{\star}_{k-1}\|^2 + \|\nabla g^{*}_{k}\|^2\right)} + \frac{\left|\arccos\left(\frac{\nabla \overline{g}^{\star}_{k-1} \nabla g^{*}_{k}}{\|\nabla \overline{g}^{\star}_{k-1}\| \|\nabla g^{*}_{k}\|}\right)\right|}{2\pi}, \tag{4.14}$$

and quantifies the similarity between the image g^{*}_{k} and the temporal mean image $\overline{g}^{\star}_{k-1}$ on the basis of the image gradient magnitude (first term) and the gradient orientation (second term). For identical gradients, $w(\mathbf{x})$ is zero and for dissimilar gradients, $w(\mathbf{x})$ is close to one.

4.4.2 Symmetric Weighting Approach

The second variant of our diffeomorphic multi-frame registration approach is based on a local *symmetric weighting* optimization scheme which was previously used in our non-diffeomorphic approach described in Chapter 3 above [118]. Our *diffeomorphic symmetric weighting* approach exploits the gradients of the image at time point k and the gradient of the temporally weighted mean image $\overline{g}^{\star}_{k-1}$. A vector $\mathbf{V}$ of the update vector field $d\mathbf{v}^{(i)}_{k,k-1}$ in (4.8) in the log-domain is computed by:

$$\sum_{\mathbf{x}\in\Omega} \left(\left(\nabla \overline{g}^{\star}_{k-1} + \nabla g^{*}_{k}\right) \left(\nabla \overline{g}^{\star}_{k-1} + \nabla g^{*}_{k}\right)^{T} + \mathbf{D} \right) \frac{\mathbf{V}}{2} = \sum_{\mathbf{x}\in\Omega} \left(\nabla \overline{g}^{\star}_{k-1} + \nabla g^{*}_{k}\right) \left(\overline{g}^{\star}_{k-1} - g^{*}_{k}\right), \tag{4.15}$$

with the elements of the weighting matrix $\mathbf{D}$ given by:

$$\mathbf{D}_{nn} = c\, w(\mathbf{x}) \left(\frac{\partial g^{*}_{k}}{\partial x_n} + \frac{\partial \overline{g}^{\star}_{k-1}}{\partial x_n} \right)^2, \tag{4.16}$$

where c is a constant (we used $c = 1$) and $w(\mathbf{x})$ is defined as in (4.14). The diffeomorphic multi-frame symmetric weighting approach allows to compute the vector $\mathbf{V}$ when at least

one of the two gradients ∇g_k^* or $\nabla \overline{g}_{k-1}^\star$ is not a zero vector (or not close to a zero vector).

4.5 Flow Boundary Preserving Smoothing of Vector Fields

In previous non-parametric registration approaches typically Gaussian filters were used for regularization of deformation vector fields (e.g., [10, 118]). In our diffeomorphic non-rigid registration approach, we use a method which prevents over-smoothing across flow boundaries. Flow boundaries represent discontinuities in a vector field, i.e., neighboring vectors have strongly different directions. In our diffeomorphic non-rigid registration approach we employ a flow boundary preserving method [125] which was previously used for optic flow computation and determines the smoothed vector $\mathbf{U}_{\mathbf{x}_c}^*$ at each position of the deformation vector field $\mathbf{u}_{k,k-1}$ as the weighted average of the vectors $\mathbf{U}_{\mathbf{x}_i}$ of $\mathbf{u}_{k,k-1}$ within the neighborhood Ω_{FB}:

$$\mathbf{U}_{\mathbf{x}_c}^* = \sum_{\mathbf{x}_i \in \Omega_{FB}} w_{\mathbf{x}_i} \mathbf{U}_{\mathbf{x}_i}, \tag{4.17}$$

where $\mathbf{x}_c$ denotes the center position and $\mathbf{x}_i$ are positions in the neighborhood Ω_{FB}. We compute the weight $w_{\mathbf{x}_i}$ for each vector based on the Euclidean distance between the positions $\mathbf{x}_c$ and $\mathbf{x}_i$, and the intensity difference between the corresponding positions in the image g_k:

$$w_{\mathbf{x}_i} = \exp\left(-\frac{\|\mathbf{x}_c - \mathbf{x}_i\|^2}{\sigma_{dist}^2} - \frac{|g_k(\mathbf{x}_c) - g_k(\mathbf{x}_i)|^2}{\sigma_{int}^2} \right), \tag{4.18}$$

where σ_{dist} and σ_{int} control the influence of the Euclidean distance between the positions and the intensity difference, respectively. The weight $w_{\mathbf{x}_i}$ describes how likely the voxels at positions $\mathbf{x}_i$ and $\mathbf{x}_c$ belong to the same image region.

In Fig. 4.2, an example for smoothing two deformation vector fields using the flow boundary preserving method in comparison to using a Gaussian kernel with standard

deviation σ_G is shown for cropped regions of two 2D vector fields for cell nuclei registration. For the Gaussian kernel we used $\sigma_G = 1$ pixel (we used a kernel size of 5×5 pixel), and for the flow boundary preserving method we used $\sigma_{dist} = 2$ pixel, $\sigma_{int} = 4$, and a 5×5 pixel neighborhood for Ω_{FB}. For both deformation vector fields, the region in the center of the figures is located on a flow boundary (the vectors in this region have very different directions). It can be seen, that using a Gaussian kernel in Figs. 4.2(a) and 4.2(c) results to over-smoothing, yielding close to zero vectors or vectors with significantly reduced magnitude in the center due to the averaging of the original vectors with very different directions (e.g., cf. the vector at coordinate $\mathbf{x} = (211, 239)$ in Fig. 4.2(a), and the vector at coordinate $\mathbf{x} = (174, 182)$ in Fig. 4.2(c)). In comparison, the flow boundary preserving method in Figs. 4.2(b) and 4.2(d) better preserved vectors on the flow boundary, and neighboring vectors at image points with similar intensities have similar direction. These examples demonstrate that the flow boundary preserving method is superior to Gaussian smoothing at flow boundaries, however, the computation time is also higher.

To reduce the computation time of our non-rigid registration approach we use the flow boundary preserving method only for vectors located at flow boundaries, while vectors in homogeneous regions of the vector field are smoothed using a Gaussian kernel [125]. We detect flow boundaries based on the gradient magnitude of the deformation vector field:

$$\mathbf{U}_{\mathbf{x}}^{FB} = \{\mathbf{U}_{\mathbf{x}} \mid \|\nabla \mathbf{U}_{\mathbf{x}}\| \geq \overline{\|\nabla \mathbf{u}\|} + c\, \sigma_{\|\nabla \mathbf{u}\|}\}, \tag{4.19}$$

where $\overline{\|\nabla \mathbf{u}\|}$ and $\sigma_{\|\nabla \mathbf{u}\|}$ denote the mean and standard deviation of the Euclidean norm of the gradients of the vector field, respectively, and c is a weighting factor (we used $c = 1$). In our non-rigid registration approach we use this smoothing scheme for regularization of the vector fields in (4.4), (4.8), and (4.2).

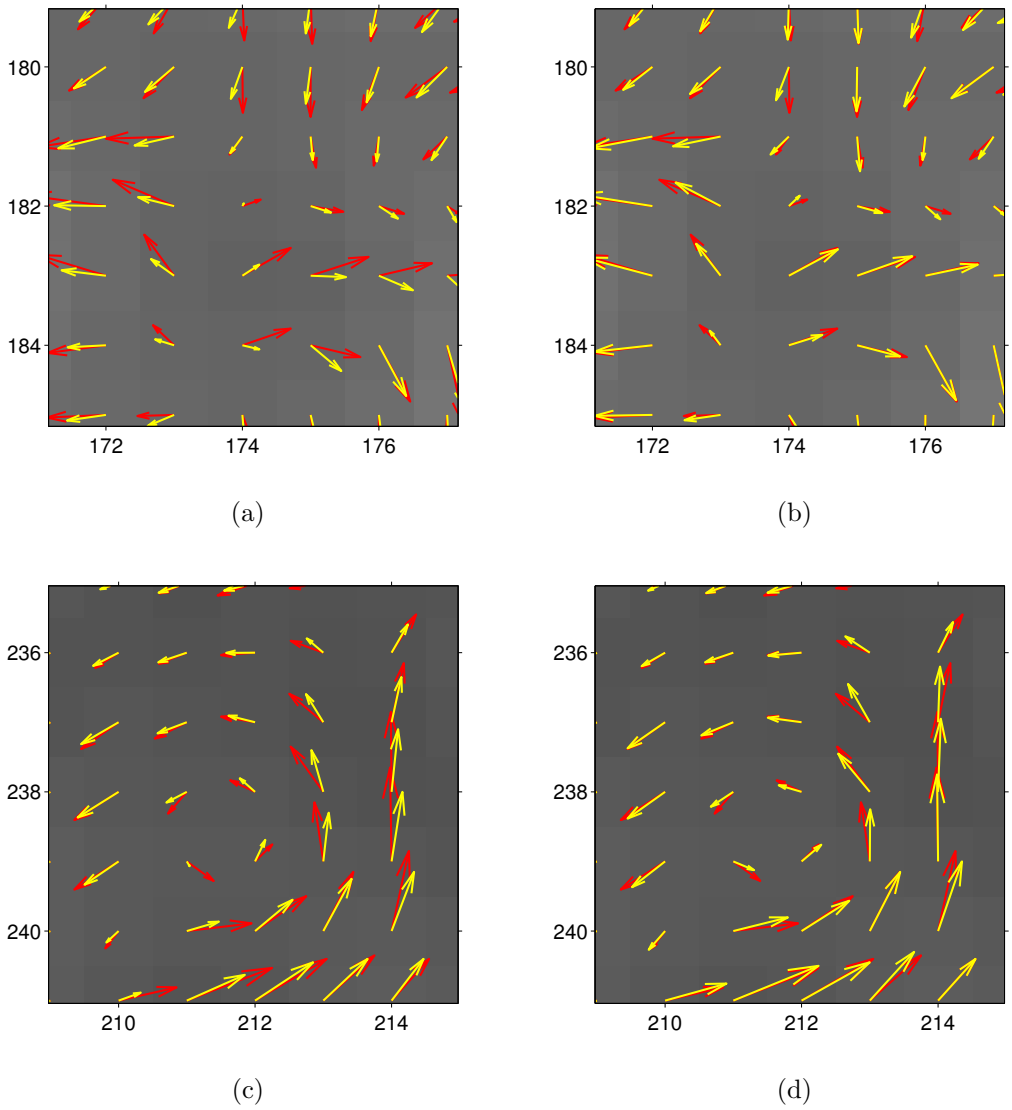

Figure 4.2: Examples demonstrating the smoothing of two deformation vector fields using a Gaussian kernel (a, c), and the flow boundary preserving method (b, d). Red arrows depict the original vectors and yellow arrows depict the smoothed vectors.

Chapter 5

Experimental Results

In this chapter, we present our experimental results for the developed multi-frame (Chapter 3) and the diffeomorphic multi-frame (Chapter 4) non-rigid registration approaches. We use synthetic as well as real microscopy image sequences displaying cell nuclei going into mitosis to study the performance of the approaches and to perform a quantitative comparison with previous non-rigid registration approaches. In Section 5.1, we first describe the used 2D and 3D live cell fluorescence microscopy image data, and in Sections 5.2 and 5.3 we present the results of applying our multi-frame and our diffeomorphic multi-frame registration approaches, respectively.

5.1 Image Data

We have used four 2D and two 3D real live cell microscopy image sequences (denoted as A, B, C, D, for the 2D, and E, F, for the 3D sequences). The 2D data consist of 100 up to 200 images with a size of 384×384 up to 512×512 pixel, and the 3D data consist of 100 images with a size of $512 \times 512 \times 10$ and $512 \times 512 \times 15$ voxel (see Table 5.1). The data has kindly been provided by Y.-C. Chen and D.L. Spector, Cold Spring Harbor Laboratory. For the acquisition of the images, a DeltaVision RT wide-field microscope (Applied Precision) at a resolution of $0.216\mu m \times 0.216\mu m$ for the 2D

	Real image sequence	Image size [pixel/voxel]	Number of time points
2D	A	512×512	150
	B	384×384	200
	C	512×512	100
	D	512×512	149
3D	E	$512 \times 512 \times 15$	100
	F	$512 \times 512 \times 10$	100

Table 5.1: Real live cell microscopy image data used for the experimental evaluation.

sequences, and $0.216\mu m \times 0.216\mu m \times 0.5\mu m$ as well as $0.216\mu m \times 0.216\mu m \times 1.5\mu m$ for the 3D sequences was used. The image sequences consist of two channels: the first channel displays nuclei of human live cells (U2OS cell line) with different chromatin stainings (H2A-mCherry, YFP-SP100 with Hoechst), and the second channel displays subcellular particles (CFP stained PML bodies). Our approaches are applied for registration of the nucleus channel. The cells depicted in the investigated image sequences are going into mitosis and therefore strong changes in the intensity structure and strong deformations occur. In addition, the intensities of the cell nuclei decrease over time due to photobleaching. The real image data was used for quantitative evaluation of our approaches and comparison with previous approaches (Sections 5.2.2 and 5.3.3). We also used the real image data for generating synthetic image sequences (see Sections 5.2.1 and 5.3.2). In the experiments based on synthetic data we investigated the influence of image noise as well as intensity scaling.

5.2 Non-Rigid Multi-Frame Registration

5.2.1 Synthetic Image Data

In this section, we describe experimental results of applying the non-rigid multi-frame registration approach described in Section 3 to synthetic image data. To simulate the

motion and deformation of cell nuclei over time, we have generated four 2D synthetic image sequences (denoted by S1, S2, S3, S4) using the first frame of different real 2D real microscopy image sequences (sequences A-D, see Table 5.1) and computed registration results for the real data. An advantage of the generated image sequences is that, on the one hand, we have ground truth for the evaluation, and, on the other hand, the image quality is very similar to real data. We used the first image g_1 from the nucleus channel of a real image sequence as well as the computed deformation vector fields $\mathbf{u}(g_k, g_1)$ over time using the pairwise weighting registration approach. To generate the synthetic image data, we used the inverted vector fields to transform the image g_1 yielding images at subsequent time points of an image sequence:

$$g_k^\bullet = g_1 \left(\mathbf{T} \left(\mathbf{x}, \mathbf{u}_{k,1}^{-1} \right) \right). \tag{5.1}$$

The inverse vector field is computed as follows. For each pixel of an image we determine a number of vectors (we used three vectors) of the original vector field which point closest to the pixel. Then, the weighted average of these vectors is computed (using the Euclidean distance as weight) and its negative vector is used as inverse vector for this pixel. Finally, for regularization we smooth the inverse vector field with a Gaussian kernel of $\sigma = 1$ pixel.

We have applied our non-rigid multi-frame registration approach to the synthetic image data and compared for each time point the computed vector field with the respective ground truth vector field. As performance measure we used the endpoint error (EE), which is often used for evaluation of optic flow approaches (e.g., [126]), and is defined by:

$$EE = \|\mathbf{U} - \mathbf{U}^{GT}\|, \tag{5.2}$$

where $\mathbf{U}$ and $\mathbf{U}^{GT}$ are vectors of the computed vector field and the ground truth vector field, respectively. The mean endpoint error EE_{mean} over all computed vectors of a cell

nucleus was determined for each time point. For our multi-frame registration approach we used different numbers of multiple frames ($N = 3, 5, 10, 20, 30, 50$) and compared the results with pairwise registration ($N = 2$). In all our experiments we used $\sigma = 2$ pixel for the standard deviation of the Gaussian kernel for regularization of the vector fields. The value for the standard deviation was determined empirically and is a good compromise. Generally, the width of the Gaussian kernel should not be chosen too small (since the regularization effect would be too weak) and should not be chosen too large (since this would result in oversmoothing of the vector fields).

As an example, in Fig. 5.1(a) the result of EE_{mean} over time for a synthetic image sequence using the multi-frame weighting registration approach is shown. It can be seen, that compared to the pairwise approach the error for the multi-frame approach is lower for all different values of N and for all time points. The registration result improves with increasing N. The lowest error averaged over all time points ($\overline{EE}_{mean}$) is obtained for $N = 50$, resulting an improvement of 29.8% compared to the pairwise approach. The results for all four synthetic image sequences and the three variants of the multi-frame registration approach are shown in Table 5.2 (columns "Original synthetic sequences"). In all cases, the multi-frame approach with $N = 3$ yields better results than the pairwise approach, and the result is further improved by increasing N up to a certain value. Averaging $\overline{EE}_{mean}$ over the four image sequences (column "Average"), the lowest error is obtained for $N = 30$ for all three variants of the multi-frame approach yielding an improvement of $24\% - 29\%$ compared to pairwise registration. The lowest error among the three variants is obtained with the multi-frame symmetric approach. Additionally, we have computed the standard deviation for the errors of the four image sequences for each N (columns "Std"). It turns out, that in all cases the standard deviation for the multi-frame approach is smaller compared to pairwise registration. Note, that the averaged errors differ significantly for the different image sequences. A main reason is that the strength of the deformations in the different image sequences

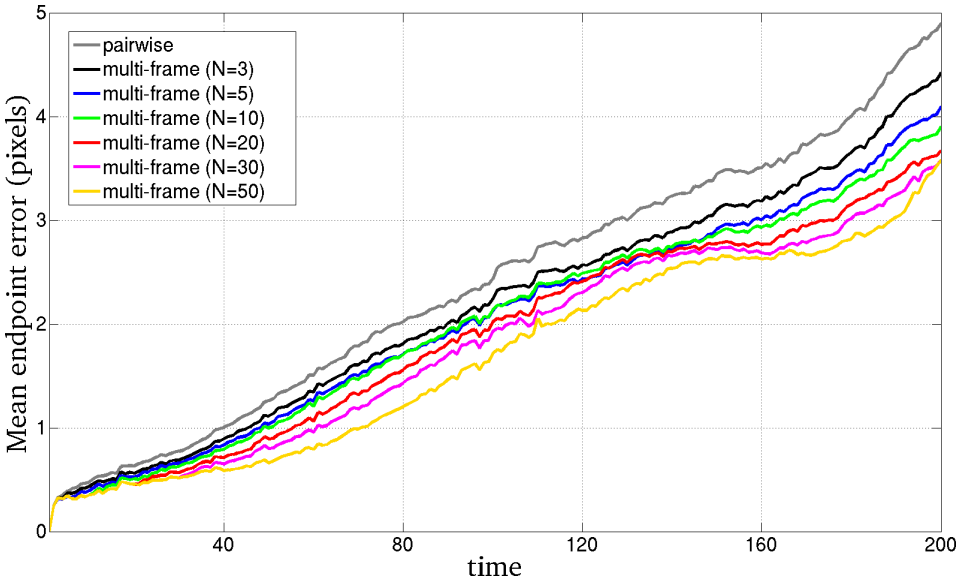

(a) Original synthetic sequence

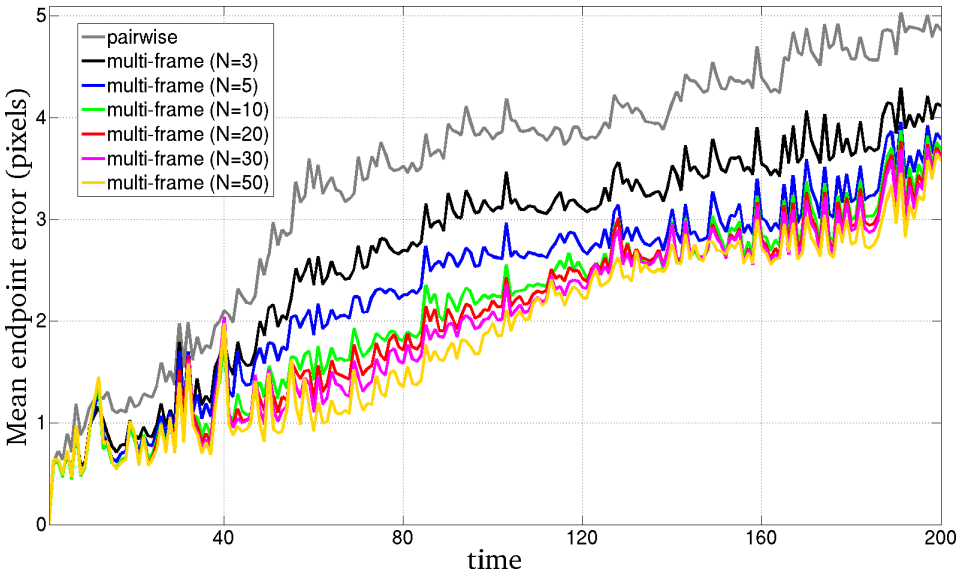

(b) Synthetic sequence with Gaussian noise and random intensity scaling

Figure 5.1: EE_{mean} for the (a) original and (b) modified synthetic image sequence S2 as a function of time for multi-frame registration (for different values of $N \geq 3$) and pairwise registration ($N = 2$). The weighting approach was used.

[pixels]		Original synthetic sequences						Sequences with Gaussian noise						Sequences with Gaussian noise and random intensity scaling					
		Sequence						Sequence						Sequence					
		S1	S2	S3	S4	Average	Std	S1	S2	S3	S4	Average	Std	S1	S2	S3	S4	Average	Std
Weighting	pairwise	1.62	2.39	3.60	2.72	2.58	0.82	1.77	2.57	4.19	4.18	3.18	1.21	2.08	3.41	4.76	4.65	3.72	1.26
	multi-frame $N = 3$	1.47	2.16	3.21	2.44	$2.32_{-10\%}$	0.72	1.55	2.29	3.54	3.49	$2.72_{-15\%}$	0.97	1.78	2.72	3.91	3.92	$3.08_{-17\%}$	1.04
	multi-frame $N = 5$	1.42	2.04	2.90	2.29	$2.16_{-16\%}$	0.61	1.45	2.13	3.09	2.96	$2.41_{-24\%}$	0.77	1.64	2.35	3.46	3.50	$2.74_{-26\%}$	0.91
	multi-frame $N = 10$	1.40	2.01	2.81	2.27	$2.12_{-18\%}$	0.59	1.40	1.97	2.71	2.62	$2.18_{-32\%}$	**0.61**	1.56	2.12	3.01	3.09	$2.44_{-34\%}$	0.74
	multi-frame $N = 20$	1.34	1.89	2.65	**2.16**	$2.01_{-22\%}$	**0.54**	1.37	1.90	2.70	**2.60**	$2.14_{-33\%}$	0.63	1.53	2.06	2.98	**2.93**	$2.38_{-36\%}$	**0.70**
	multi-frame $N = 30$	1.31	1.81	**2.62**	2.17	$\mathbf{1.98_{-24\%}}$	0.55	1.34	1.82	**2.64**	2.61	$\mathbf{2.10_{-34\%}}$	0.64	1.50	2.00	**2.92**	2.94	$\mathbf{2.34_{-37\%}}$	0.71
	multi-frame $N = 50$	**1.27**	**1.68**	2.86	2.24	$2.01_{-22\%}$	0.69	**1.29**	**1.70**	2.87	2.70	$2.14_{-33\%}$	0.77	**1.45**	**1.89**	3.09	3.02	$2.36_{-37\%}$	0.82
Symmetric	pairwise	1.71	2.51	3.85	3.05	2.78	0.90	1.91	2.74	4.60	4.58	3.46	1.35	2.26	3.59	5.25	5.22	4.08	1.44
	multi-frame $N = 3$	1.51	2.24	3.41	2.52	$2.42_{-13\%}$	0.78	1.58	2.32	3.77	3.66	$2.83_{-18\%}$	1.06	1.76	2.70	4.20	4.45	$3.27_{-20\%}$	1.27
	multi-frame $N = 5$	1.44	2.12	3.07	2.34	$2.24_{-19\%}$	0.67	1.48	2.15	3.20	3.10	$2.48_{-28\%}$	0.82	1.63	2.40	3.75	3.85	$2.91_{-29\%}$	1.08
	multi-frame $N = 10$	1.39	1.98	2.71	2.24	$2.08_{-25\%}$	0.55	1.42	2.00	2.81	2.68	$2.23_{-36\%}$	0.65	1.56	2.23	3.20	3.36	$2.59_{-37\%}$	0.85
	multi-frame $N = 20$	1.34	1.87	2.52	**2.23**	$1.99_{-28\%}$	**0.51**	1.36	1.91	2.61	**2.55**	$2.11_{-39\%}$	**0.59**	1.51	2.10	2.95	**3.15**	$2.43_{-40\%}$	**0.76**
	multi-frame $N = 30$	1.30	1.80	**2.48**	2.27	$\mathbf{1.96_{-29\%}}$	0.53	1.32	1.82	**2.54**	2.55	$\mathbf{2.06_{-40\%}}$	0.60	1.48	2.03	**2.87**	3.18	$\mathbf{2.39_{-41\%}}$	0.78
	multi-frame $N = 50$	**1.24**	**1.68**	3.05	2.50	$2.12_{-24\%}$	0.81	**1.27**	**1.70**	3.01	2.90	$2.22_{-36\%}$	0.87	**1.44**	**1.94**	3.45	3.44	$2.57_{-37\%}$	1.03
Symm. weighting	pairwise	1.70	2.49	3.72	2.85	2.69	0.84	1.82	2.65	4.31	4.34	3.28	1.25	2.04	3.31	4.94	4.85	3.78	1.38
	multi-frame $N = 3$	1.51	2.23	3.30	2.47	$2.38_{-12\%}$	0.74	1.56	2.35	3.63	3.47	$2.75_{-16\%}$	0.98	1.70	2.71	4.08	4.12	$3.15_{-17\%}$	1.17
	multi-frame $N = 5$	1.44	2.09	2.93	2.28	$2.18_{-19\%}$	0.61	1.47	2.16	3.12	2.94	$2.42_{-26\%}$	0.76	1.62	2.41	3.59	3.67	$2.82_{-26\%}$	0.99
	multi-frame $N = 10$	1.42	2.01	2.85	2.25	$2.13_{-21\%}$	0.59	1.41	2.00	2.71	**2.60**	$2.18_{-34\%}$	**0.60**	1.55	2.21	3.06	**3.16**	$2.50_{-34\%}$	**0.76**
	multi-frame $N = 20$	1.37	1.90	2.62	**2.20**	$2.02_{-25\%}$	**0.53**	1.40	1.95	2.71	2.64	$2.17_{-34\%}$	0.62	1.58	2.19	3.06	3.21	$2.51_{-34\%}$	0.77
	multi-frame $N = 30$	1.35	1.82	**2.60**	2.21	$\mathbf{2.00_{-26\%}}$	0.54	1.37	1.87	**2.64**	2.64	$\mathbf{2.13_{-35\%}}$	0.62	1.56	2.11	**2.99**	3.22	$\mathbf{2.47_{-35\%}}$	0.77
	multi-frame $N = 50$	**1.30**	**1.72**	3.09	2.47	$2.15_{-20\%}$	0.79	**1.32**	**1.75**	3.16	2.99	$2.31_{-30\%}$	0.91	**1.52**	**2.01**	3.40	3.47	$2.60_{-31\%}$	0.99

Table 5.2: $\overline{EE}_{mean}$ for four synthetic image sequences, for the three variants of the multi-frame and the pairwise registration approach. Percentages indicate the change compared to pairwise registration.

differs significantly. We computed the mean length of the ground truth displacements in the image sequences S1, S2, S3, S4 as a measure for the strength of the deformations, and obtained values of 6.78, 13.34, 29.90, and 20.45 pixel, respectively. These values correspond with the averaged errors, for example, for S3 and S4 the relatively large errors correspond to large values of the mean displacements (Table 5.2, first four columns of "Original synthetic sequences").

To increase the level of difficulty for registration, we added Gaussian noise with standard deviation $\sigma_n = 3$ pixel. In addition, we generated synthetic image data which simulates cell nucleus intensity variations over time by scaling the intensities of the noisy data by a uniformly distributed random factor ρ_k ($0.95 \leq \rho_k \leq 1.05$) multiplied with the intensity values. The random factor is determined for each time point independently. The results for these more difficult synthetic image sequences can be found in the corresponding columns of Table 5.2. It can be seen, that the error increased (as expected), but also in this case the multi-frame approach outperforms the pairwise approach (for all values of N). Averaging the errors over all four image sequences, the best result is obtained by the multi-frame approach for $N = 30$, for all three variants. The improvements are $34\% - 40\%$ for the sequences with Gaussian noise, and $35\% - 41\%$ for the sequences with Gaussian noise and intensity scaling. The lowest error in the first case is obtained by the symmetric approach and in the second case by the weighting approach. In Fig. 5.1(b) an example of EE_{mean} over time using the pairwise and the multi-frame weighting approach for a synthetic sequence with added Gaussian noise and intensity scaling is shown. The image sequence used in this example is the same as for Fig. 5.1(a). We can observe, that the multi-frame approach yields a better result than the pairwise approach. The lowest value of $\overline{EE}_{mean}$ is obtained for $N = 50$, yielding an improvement of 44.6%.

To investigate whether the improvement of the multi-frame approach compared to pairwise registration is statistically significant, we performed a Wilcoxon signed-rank

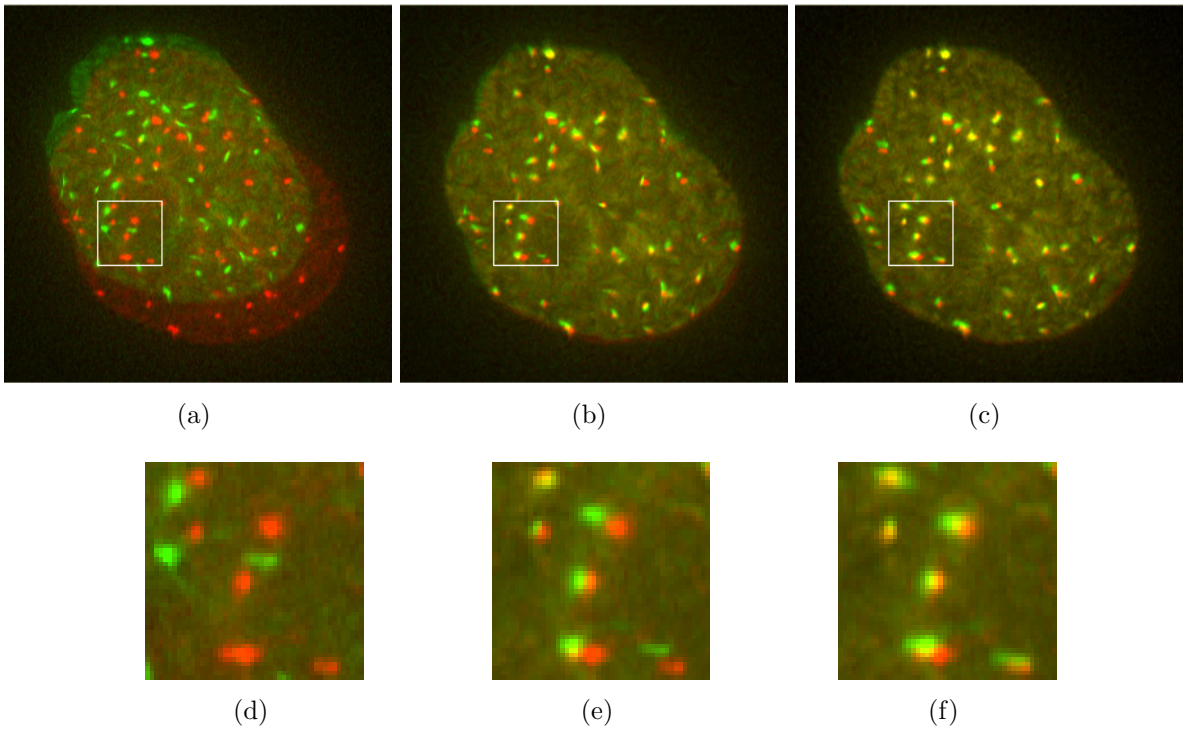

Figure 5.2: Overlays of images for time points 1 (red) and 50 (green) of the synthetic image sequence S4 with Gaussian noise and random intensity scaling for (a) the unregistered images, and for the registered images using (b) the pairwise weighting approach and (c) the multi-frame weighting approach ($N = 20$). (d)-(f) Enlarged sections for the marked regions in (a)-(c). Yellow indicates overlapping intensities.

test (non-parametric test). Prior application of a Shapiro-Wilk test showed that the data does not follow a normal distribution in all 54 cases (3 registration variants, 3 classes of image sequences, 6 different values of N). Using the Wilcoxon signed-rank test we obtained $p < 0.063$ in all 54 cases. Thus, the multi-frame approach yields a statistically significant improvement compared to pairwise registration. For a visual inspection of the results we show an overlay of the cell nuclei for two different time points, before and after registration using the pairwise and the multi-frame approach for $N = 20$ (Fig. 5.2). It can be seen, that the alignment of the nuclei improved using the multi-frame approach.

To quantify the influence of Gaussian noise and intensity scaling on the registration results we averaged $\overline{EE}_{mean}$ of Table 5.2 (columns "Average") over the three variants

		Gaussian noise	Gaussian noise and intensity scaling
pairwise		+23.1%	+43.8%
multi-frame	$N = 3$	+16.7%	+33.6%
	$N = 5$	+11.0%	+28.5%
	$N = 10$	+3.9%	+18.8%
	$N = 20$	+6.6%	+21.4%
	$N = 30$	+6.0%	+21.3%
	$N = 50$	+6.3%	+20.1%

Table 5.3: Changes in percentage of $\overline{EE}_{mean}$ for the modified synthetic image sequences w.r.t. the error in the original synthetic sequences. The changes have been computed using the $\overline{EE}_{mean}$ values from Table 5.2 (columns "Average") averaged over the three variants of the registration approach.

of the pairwise and the multi-frame approach, and compared the errors for the more difficult synthetic sequences (Gaussian noise, Gaussian noise and intensity scaling) with those for the original synthetic sequences. The differences in percentage can be found in Table 5.3. We can observe, that for both cases the error has been increased, as expected. However, the increase is higher for the pairwise approach and the multi-frame approach for small N ($N = 3, 5$), while for larger values of N ($N = 10, 20, 30, 50$) the increase of the error is lower. This shows that the multi-frame approach is more robust to Gaussian noise and intensity scaling than the pairwise approach, and a larger N increases the robustness.

Furthermore, we studied the influence of the standard deviation σ_n of the Gaussian noise on the registration result for different values of N. We added Gaussian noise with different values of σ_n ($\sigma_n = 1, 3, 5, 7, 9$ pixel) to the synthetic image sequence S2 and applied the pairwise as well as the multi-frame weighting approach. The results can be found in Fig. 5.3. It can be seen, that for all values of σ_n the error for the multi-frame approach is lower compared to pairwise registration, and the error is decreasing for increasing N.

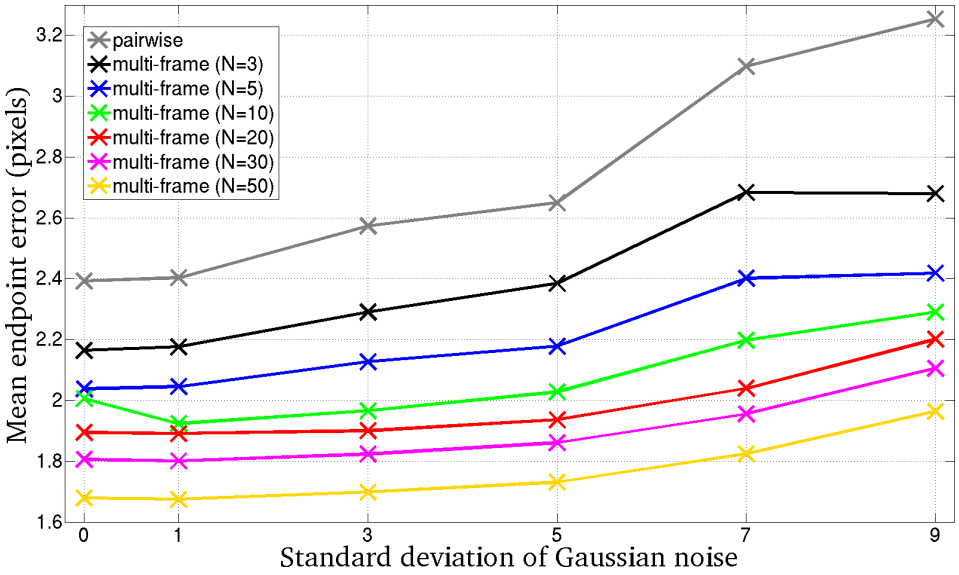

Figure 5.3: $\overline{EE}_{mean}$ as a function of the standard deviation σ_n of Gaussian image noise for the synthetic image sequence S2, for the pairwise and the multi-frame weighting approach.

5.2.2 Real Image Data

We have also applied our non-rigid multi-frame registration approach to the 2D real microscopy image data of live cells. First, we studied the convergence properties of the multi-frame registration approach based on two metrics: The root mean squared (RMS) intensity differences and the correlation coefficient (CC). For the multi-frame approach we used different numbers of multiple frames ($N = 3, 5, 10, 20, 30, 50$), and in all our experiments we used $\sigma = 2.0$ pixels for the standard deviation of the Gaussian kernel for regularization of the vector fields. We computed the mean RMS and the mean CC for each iteration (we used 10 iterations) averaged over all image pairs of the transformed g_k and $g_l^\star$ (using (3.4)) as well as over all time points of an image sequence. Fig. 5.4 shows an example of both metrics for the multi-frame and the pairwise symmetric weighting approach applied to one real image sequence. It can be seen, that the multi-frame approach (for the different values of N) and the pairwise approach converge and have a similar rate. We can also observe, that the RMS values of the multi-frame approach are larger and the CC values are smaller than the corresponding values

of the pairwise approach (except for $N = 3$ for which the multi-frame approach yields a slightly better result than pairwise registration). This is what we expect, since the multi-frame approach is based on the minimization of the sum of mean squared intensity differences between several images, while in pairwise registration the minimization is computed only between two images. To provide further evidence on this, we computed the mean RMS between each registered image and the reference image (first image) for the same real image sequence (Fig. 5.5). This metric describes the quality of the registration for the whole image sequence. It can be seen that the multi-frame approach yields a lower error than pairwise registration.

Second, we performed a quantitative evaluation of the multi-frame approach based on manually tracked structures in the nucleus channel of the image sequences. For each sequence, positions of 9 spot-like structures within cell nuclei were tracked for 38 up to 125 subsequent time points. For each structure and each time point we computed the registration error as the Euclidean distance of the current position of the structure (center of gravity) to its position in the image at the first tracked time point. In Fig. 5.6 we show an example of the registration error for one spot-like structure in the image sequence B when applying the multi-frame symmetric weighting approach for different values of N ($N = 3, 5, 10, 20, 30, 50$). It can be seen, that the multi-frame approach yields a better result compared to the pairwise approach (grey line) and the error decreases with increasing N. We also computed the mean registration error e_{mean} over all time points. It turns out, that multi-frame registration with $N = 10$ reduces e_{mean} by 16% compared to pairwise registration, and for $N = 20$ and $N = 50$ the improvement is 22% and 40%, respectively. In Fig. 5.7 the original and the registered images at time point 60 overlaid with the positions of the 9 tracked spot-like structures are displayed. It can be seen, that the displacements of the positions over time w.r.t. the ground truth positions at the first frame (which represent the registration error) for the multi-frame approach are much smaller compared to the unregistered case and smaller compared to pairwise

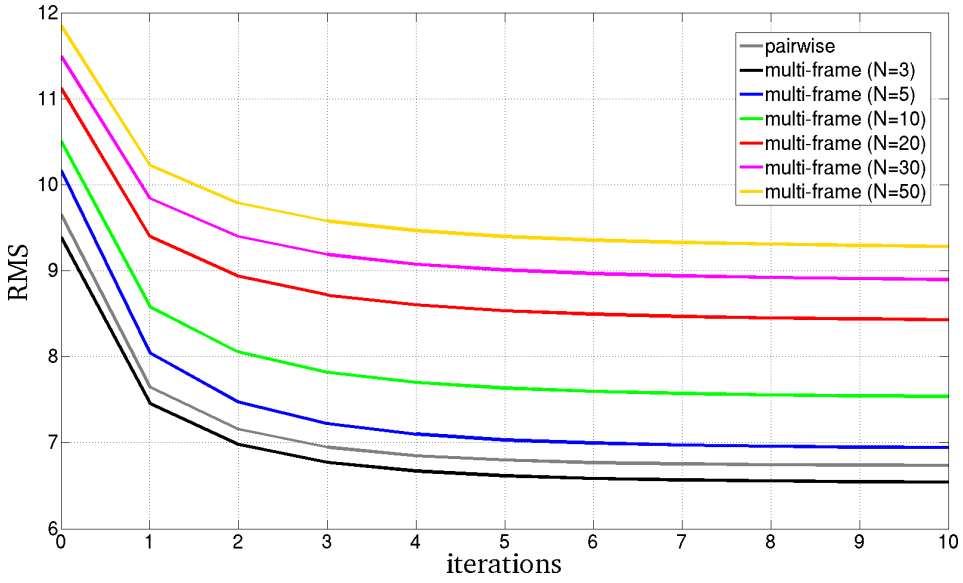

(a) Mean RMS

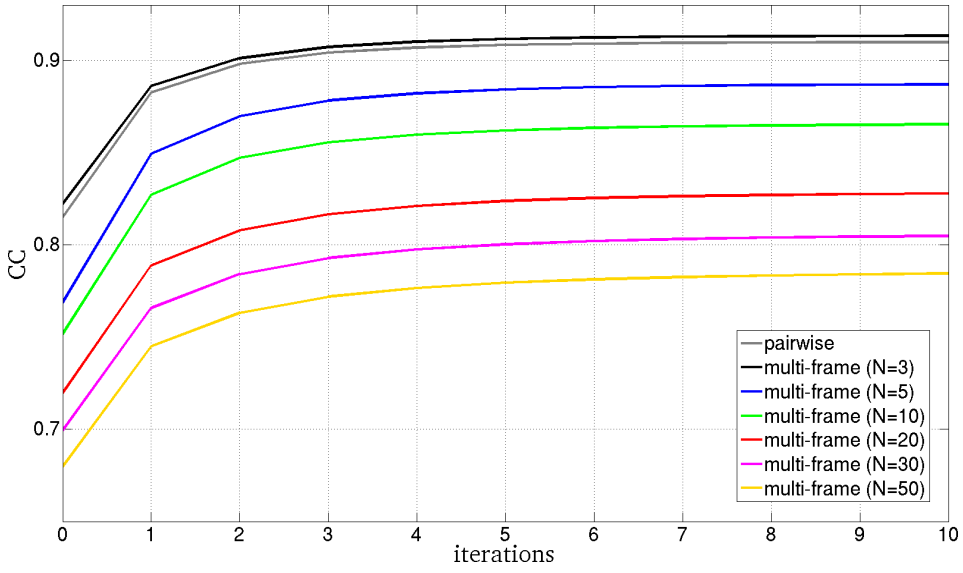

(b) Mean CC

Figure 5.4: (a) Mean of root mean squared (RMS) intensity error and (b) mean of correlation coefficient (CC) averaged over all time points for each iteration step. The multi-frame and the pairwise symmetric weighting approach was applied to the real image sequence C.

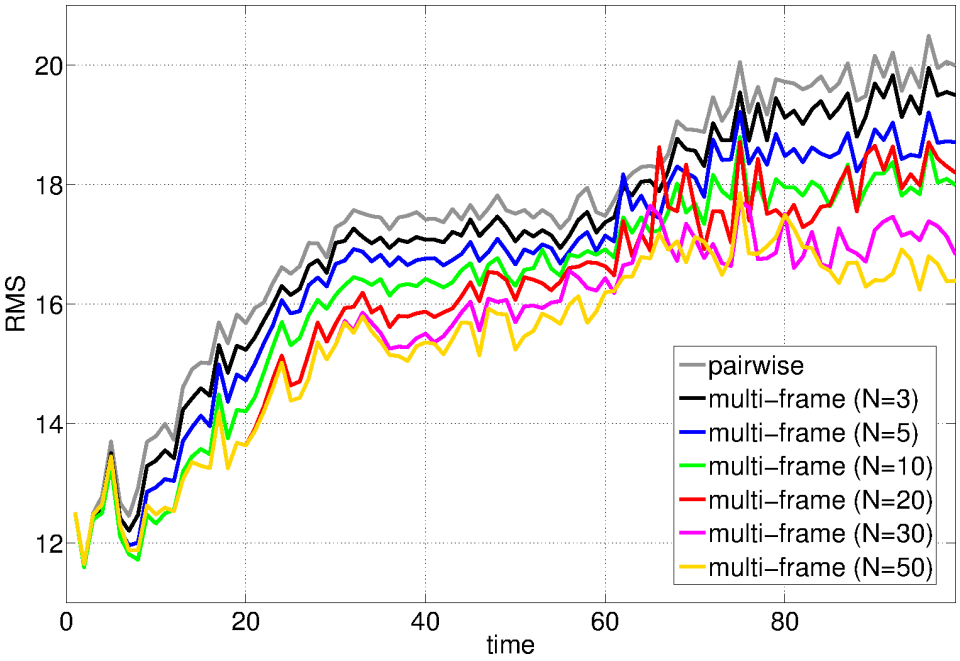

Figure 5.5: Mean of root mean squared (RMS) intensity error between each registered image and the reference image of the image sequence C using the multi-frame and the pairwise symmetric weighting approach.

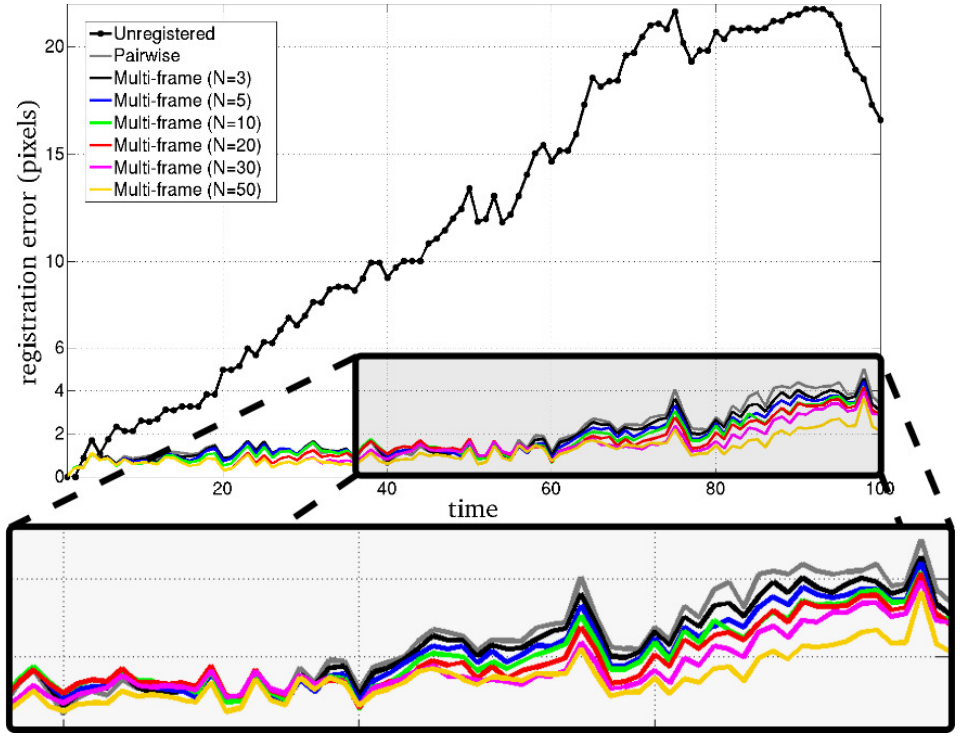

Figure 5.6: Registration error for one spot-like structure in the real image sequence B as a function of time for the multi-frame and the pairwise symmetric weighting approach.

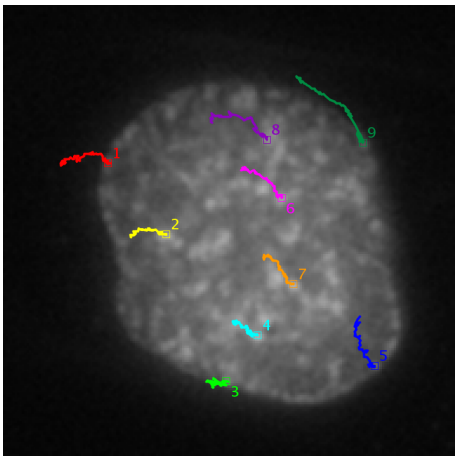

(a) Unregistered

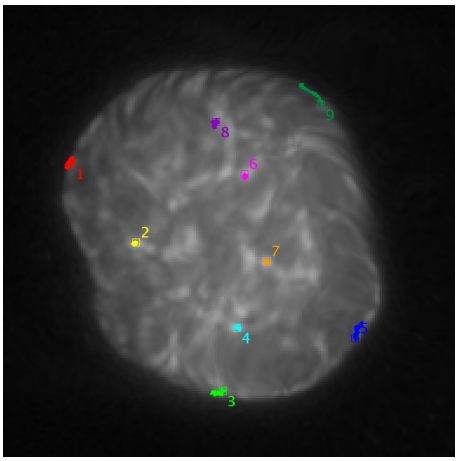

(b) Pairwise weighting approach

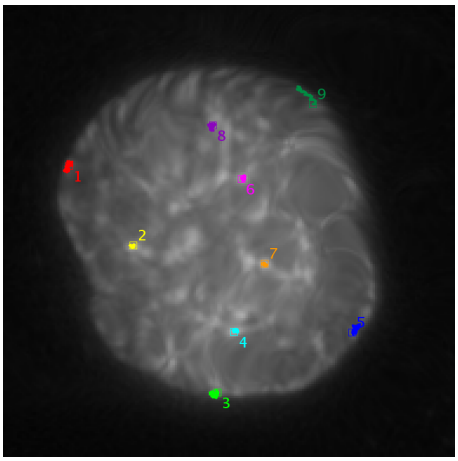

(c) Multi-frame weighting approach ($N = 10$)

Figure 5.7: Positions over time for 9 spot-like structures overlaid with an image ($t = 60$) from image sequence B (nucleus channel). In (a) the original image and positions over time for the unregistered case are shown, and in (b) and (c) the registered images and positions over time for the pairwise and the multi-frame registration approaches are shown.

registration (in particular for the structures 3, 5, and 9). Note that at the border of a nucleus the deformations are generally larger than in the center and therefore also the registration improvement is larger there.

The results for the mean error averaged over all 9 spot-like structures ($\overline{e}_{mean}$) for the image sequence B are shown in Table 5.4 (column "Without temporal weighting") for each of the three variants of the multi-frame approach. It can be seen that for all three

[pixels]			Without temporal weighting		Temporal weighting based on temporal distance		Temporal weighting based on image similarity	
			$\overline{e}_{mean}$	$\overline{e}_{max}$	$\overline{e}_{mean}$	$\overline{e}_{max}$	$\overline{e}_{mean}$	$\overline{e}_{max}$
unregistered			13.97	26.16	13.97	26.16	13.97	26.16
Weighting	pairwise		2.87	6.09	2.87	6.09	2.87	6.09
	multi-frame	$N = 3$	$2.76_{-4\%}$	$5.83_{-4\%}$	$2.78_{-3\%}$	$5.91_{-3\%}$	$2.79_{-3\%}$	$5.80_{-5\%}$
		$N = 5$	$2.52_{-12\%}$	$5.56_{-9\%}$	$2.58_{-10\%}$	$5.61_{-8\%}$	$2.60_{-10\%}$	$5.61_{-8\%}$
		$N = 10$	$2.33_{-19\%}$	$\mathbf{5.21_{-14\%}}$	$\mathbf{2.47_{-14\%}}$	$\mathbf{5.43_{-11\%}}$	$2.45_{-15\%}$	$\mathbf{5.32_{-13\%}}$
		$N = 20$	$2.21_{-13\%}$	$8.07_{+32\%}$	$2.51_{-12\%}$	$5.45_{-11\%}$	$2.42_{-16\%}$	$5.33_{-12\%}$
		$N = 30$	$\mathbf{2.14_{-25\%}}$	$8.47_{+39\%}$	$2.48_{-14\%}$	$5.67_{-7\%}$	$\mathbf{2.38_{-17\%}}$	$5.98_{-2\%}$
		$N = 50$	$2.53_{-12\%}$	$9.75_{+60\%}$	$2.49_{-13\%}$	$6.60_{+8\%}$	$2.45_{-14\%}$	$7.00_{+15\%}$
Symmetric	pairwise		2.97	6.20	2.97	6.20	2.97	6.20
	multi-frame	$N = 3$	$2.74_{-8\%}$	$5.80_{-7\%}$	$2.77_{-7\%}$	$5.91_{-5\%}$	$2.70_{-9\%}$	$5.66_{-9\%}$
		$N = 5$	$2.46_{-17\%}$	$5.48_{-12\%}$	$2.32_{-22\%}$	$5.23_{-16\%}$	$2.47_{-17\%}$	$5.37_{-13\%}$
		$N = 10$	$2.32_{-22\%}$	$\mathbf{5.33_{-14\%}}$	$2.27_{-24\%}$	$\mathbf{5.09_{-18\%}}$	$2.27_{-23\%}$	$5.04_{-19\%}$
		$N = 20$	$2.32_{-22\%}$	$7.97_{+28\%}$	$2.27_{-24\%}$	$5.16_{-17\%}$	$2.23_{-25\%}$	$4.97_{-20\%}$
		$N = 30$	$2.29_{-23\%}$	$8.10_{+31\%}$	$2.27_{-24\%}$	$5.26_{-15\%}$	$\mathbf{2.18_{-27\%}}$	$\mathbf{4.85_{-22\%}}$
		$N = 50$	$\mathbf{2.10_{-29\%}}$	$7.95_{+28\%}$	$\mathbf{2.26_{-24\%}}$	$5.95_{-4\%}$	$2.20_{-26\%}$	$5.33_{-14\%}$
Symmetric weighting	pairwise		2.84	6.05	2.84	6.05	2.84	6.05
	multi-frame	$N = 3$	$2.70_{-5\%}$	$5.79_{-4\%}$	$2.73_{-4\%}$	$5.86_{-3\%}$	$2.74_{-3\%}$	$5.88_{-3\%}$
		$N = 5$	$2.47_{-13\%}$	$\mathbf{5.45_{-10\%}}$	$2.49_{-12\%}$	$5.46_{-10\%}$	$2.54_{-10\%}$	$5.51_{-9\%}$
		$N = 10$	$\mathbf{2.32_{-18\%}}$	$5.51_{-9\%}$	$\mathbf{2.40_{-16\%}}$	$\mathbf{5.36_{-11\%}}$	$\mathbf{2.40_{-15\%}}$	$\mathbf{5.37_{-11\%}}$
		$N = 20$	$2.53_{-11\%}$	$8.12_{+34\%}$	$2.53_{-11\%}$	$5.89_{-3\%}$	$2.52_{-11\%}$	$5.56_{-8\%}$
		$N = 30$	$2.54_{-11\%}$	$8.79_{+45\%}$	$2.56_{-10\%}$	$7.21_{+19\%}$	$2.48_{-13\%}$	$5.63_{-7\%}$
		$N = 50$	$2.70_{-5\%}$	$10.17_{+68\%}$	$2.59_{-9\%}$	$7.76_{+28\%}$	$2.57_{-9\%}$	$7.25_{+20\%}$

Table 5.4: Registration error for 9 spot-like structures of the real image sequence B using three variants of the multi-frame and pairwise registration combined with different temporal weighting schemes. Percentages indicate the change to pairwise registration.

variants the multi-frame approach with $N = 3$ yields a lower error than the pairwise approach, and the error is further reduced by increasing N up to a certain value. The value of N for which the result is best generally varies depending on the image sequence and on the variant of the multi-frame approach. For the weighting, the symmetric, and the symmetric weighting approach the best result is obtained for $N = 30$, $N = 50$,

and $N = 10$, respectively, yielding an improvement of 25%, 29%, and 18% compared to pairwise registration. The lowest error is obtained with the symmetric approach ($\overline{e}_{mean} = 2.10$ pixel).

To study the reliability of the registration results in terms of outliers we also determined the maximum registration error e_{max} for all 9 spot-like structures. The maximum error averaged over all structures ($\overline{e}_{max}$) of the image sequence B is shown in Table 5.4 (column "Without temporal weighting"). Compared to pairwise registration, multi-frame registration with $N = 3, 5$, and 10 reduces $\overline{e}_{max}$ for all three variants, and the best result is obtained for either $N = 10$ or $N = 5$ (depending on the variant) yielding an improvement of $10\% - 14\%$. For $N = 20, 30, 50$, $\overline{e}_{max}$ is larger than for pairwise registration, which is an indication of outliers due to the very different intensity structure of the nuclei within the relatively large temporal range ($N \geq 20$ time points).

An example for outliers in the results for a tracked structure using the multi-frame symmetric approach for image sequence B is shown in Fig. 5.8(a). It can be seen, that in this image sequence for certain time points around $t = 100$ and for the multi-frame approach with $N = 20, 30, 50$ the errors are very large. To reduce the errors we have used the two temporal weighting schemes (temporal distance, image similarity) described in Section 3.6. From the results in Fig. 5.8(b) and 5.8(c) it can be seen, that the outliers have been significantly reduced for both temporal weighting schemes. The errors at the other time points have been slightly increased. Note that for this image sequence the errors at the end of the sequence decrease for all approaches as well as for the unregistered case since the cell is moving back to its initial location. The results for all 9 spot-like structures and for both temporal weighting schemes are shown in Table 5.4. We can observe, that for both schemes and for all three variants with $N = 3, 5, 10$, the values for $\overline{e}_{max}$ are similar as in the case without temporal weighting. On the other hand, $\overline{e}_{max}$ is significantly lower for $N = 20, 30, 50$. For the symmetric and symmetric weighting approach the lowest values for $\overline{e}_{max}$ are obtained by the temporal weighting

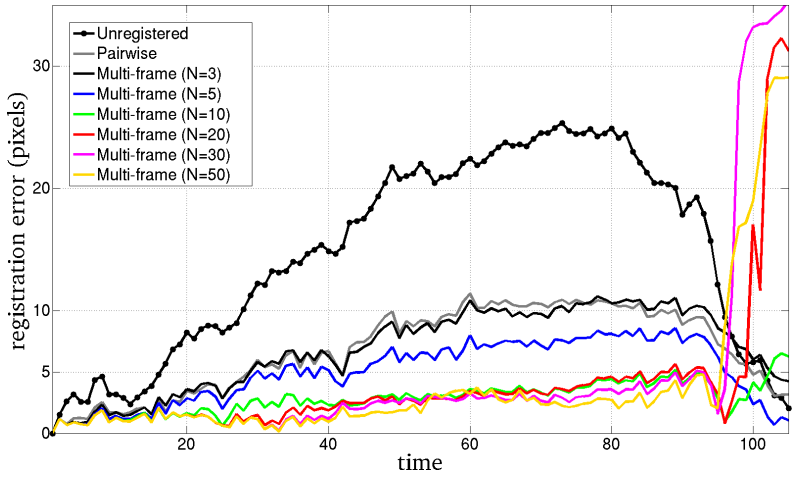

(a) Without temporal weighting

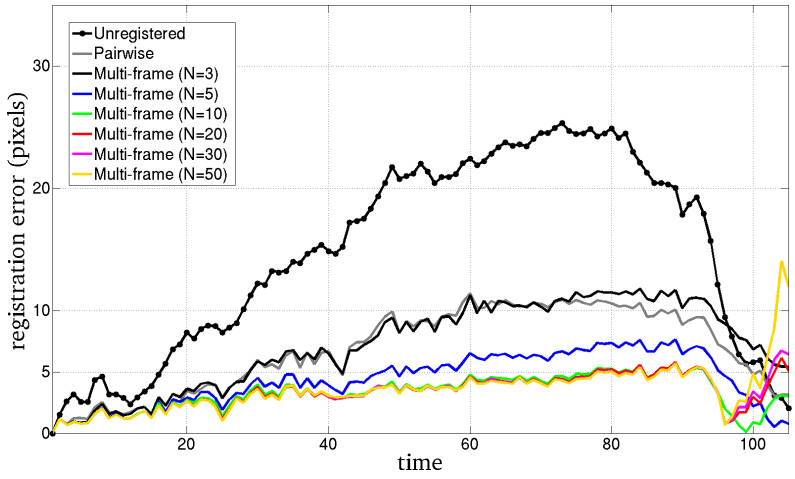

(b) Temporal weighting based on temporal distance

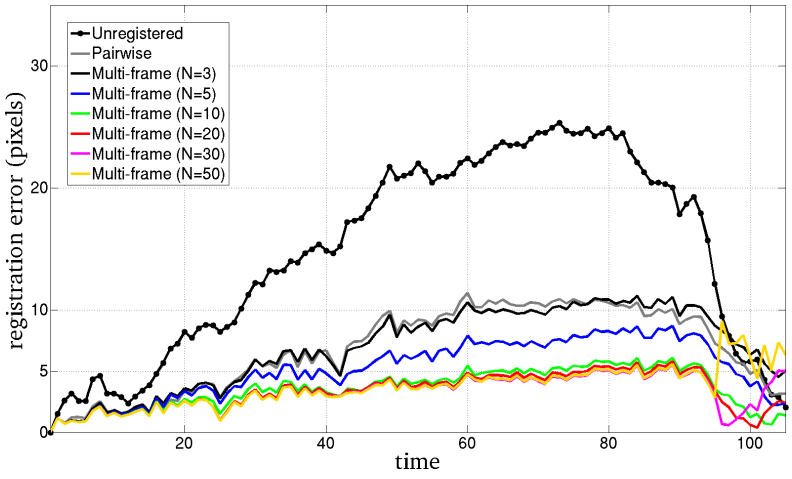

(c) Temporal weighting based on image similarity

Figure 5.8: Registration error for one spot-like structure in the real image sequence B as a function of time for the multi-frame symmetric approach without and with temporal weighting, and the pairwise symmetric approach.

		Temporal weighting based on temporal distance		Temporal weighting based on image similarity	
		$\overline{e}_{mean}$	$\overline{e}_{max}$	$\overline{e}_{mean}$	$\overline{e}_{max}$
multi-frame	$N = 3$	+1.1%	+1.5%	+0.4%	−0.5%
	$N = 5$	−0.9%	−1.2%	+2.1%	−0.0%
	$N = 10$	+2.5%	−1.1%	+2.3%	−2.0%
	$N = 20$	+3.8%	−31.7%	+1.7%	−34.3%
	$N = 30$	+5.0%	−28.5%	+1.0%	−35.1%
	$N = 50$	+0.1%	−27.1%	−1.5%	−29.7%

Table 5.5: Changes in percentage of $\overline{e}_{mean}$ and $\overline{e}_{max}$ for the multi-frame registration approach using temporal weighting compared to the errors without temporal weighting. The changes have been computed using the error values for the real image sequence B from Table 5.4 averaged over the three variants of the multi-frame approach.

schemes. For $\overline{e}_{mean}$, in most cases we can observe a slight increase for the temporal weighting schemes compared to using no temporal weighting.

We also computed the changes in percentage for the registration error for the multi-frame approach using the two temporal weighting schemes in comparison to using no temporal weighting. The results averaged over the three variants of the multi-frame approach can be found in Table 5.5. We can observe, that for both temporal weighting schemes and for $N = 3$, 5, 10, $\overline{e}_{max}$ has not changed significantly while for $N = 20$, 30, 50, $\overline{e}_{max}$ is significantly lower. For both temporal weighting schemes we can observe for most values of N a slight increase of $\overline{e}_{mean}$. It also turns out, that the temporal weighting scheme based on image similarity with gradient differences yields in most cases better results than the scheme based on temporal distance.

Finally we have applied the multi-frame registration approach with temporal weighting based on image similarity for different values of N to all four real image sequences (Table 5.6). It can be seen, that we obtain similar results for the different image sequences. The best result for $\overline{e}_{mean}$ averaged over all four sequences is obtained for $N = 10$ or $N = 50$ (depending on the variant) and yields an improvement of $20\% - 24\%$, com-

pared to the respective pairwise registration. Note, that the results for $N = 10$, 20, 30, 50 are very similar. For $\overline{e}_{max}$ the best result is obtained for $N = 20$ or $N = 30$, which is an improvement of $11\% - 16\%$, compared to pairwise registration. The lowest value for $\overline{e}_{mean}$ is obtained with the multi-frame weighting approach ($N = 50$), and the lowest value for $\overline{e}_{max}$ is obtained with the multi-frame symmetric weighting approach ($N = 30$).

To investigate whether the improvement of the multi-frame approach compared to pairwise registration for the real image sequences is statistically significant, we performed a Wilcoxon signed-rank test (non-parametric test). Prior application of a Shapiro-Wilk test showed that the data does not follow a normal distribution in all 18 cases (3 registration variants, 6 different values of N). Using the Wilcoxon signed-rank test we obtained $p < 0.0009$ in all 18 cases. Thus, the multi-frame approach yields a statistically significant improvement compared to pairwise registration. We also performed a statistical test on the improvement between the multi-frame approach and pairwise registration compared (normalized) to the unregistered case (Wilcoxon signed-rank test, symmetric weighting approach) which yielded $p < 0.008$ in all 18 cases. Thus, the improvement of the multi-frame approach is statistically significant compared to the unregistered case as well.

In addition, we have performed an experimental comparison with the temporal groupwise registration approach of Metz et al. [12] which is based on B-splines and was previously applied for the registration of medical image data (CT, MR, and US images of the heart and the lung). With this approach, all images of an image sequence are registered simultaneously by minimizing the sum of mean squared intensity differences between all images and the mean image of the whole sequence. For our comparison, we used the implementation of the approach in elastix [127]. We have applied the temporal groupwise registration approach to image sequence B using a grid spacing of 16×16 pixel and each time point as well as three multiresolution levels. We tested different val-

[pixels]			$\overline{e}_{mean}$					$\overline{e}_{max}$
			Sequence					
			A	B	C	D	Average	Average
unregistered			6.56	13.97	26.65	27.84	18.76	33.26
Weighting	pairwise		3.23	2.87	4.39	7.08	4.39	9.61
	multi-frame	$N = 3$	3.03	2.79	3.87	6.51	$4.05_{-8\%}$	$9.16_{-5\%}$
		$N = 5$	3.09	2.60	3.67	5.81	$3.79_{-14\%}$	$8.90_{-7\%}$
		$N = 10$	2.99	2.45	3.56	5.31	$3.58_{-19\%}$	$8.58_{-11\%}$
		$N = 20$	2.83	2.42	3.60	5.35	$3.55_{-19\%}$	$\mathbf{8.58_{-11\%}}$
		$N = 30$	2.78	**2.38**	3.54	5.27	$3.49_{-20\%}$	$8.78_{-9\%}$
		$N = 50$	**2.75**	2.45	**3.52**	**5.23**	$\mathbf{3.49_{-21\%}}$	$9.13_{-5\%}$
Symmetric	pairwise		3.70	2.97	4.95	7.06	4.67	10.13
	multi-frame	$N = 3$	3.44	2.70	4.26	6.03	$4.11_{-12\%}$	$9.27_{-9\%}$
		$N = 5$	3.31	2.47	3.94	5.70	$3.85_{-18\%}$	$9.03_{-11\%}$
		$N = 10$	3.20	2.27	3.91	5.30	$3.67_{-21\%}$	$8.74_{-14\%}$
		$N = 20$	3.11	2.23	3.79	5.18	$3.58_{-23\%}$	$8.49_{-16\%}$
		$N = 30$	**3.11**	**2.18**	3.74	5.14	$3.54_{-24\%}$	$\mathbf{8.46_{-16\%}}$
		$N = 50$	3.11	2.20	**3.73**	**5.12**	$\mathbf{3.54_{-24\%}}$	$8.47_{-16\%}$
Symmetric Weighting	pairwise		3.39	2.84	4.79	6.90	4.48	9.63
	multi-frame	$N = 3$	3.21	2.74	4.03	6.30	$4.07_{-9\%}$	$9.08_{-6\%}$
		$N = 5$	3.14	2.54	3.71	5.73	$3.78_{-16\%}$	$8.89_{-8\%}$
		$N = 10$	**3.14**	**2.40**	3.53	**5.19**	$\mathbf{3.57_{-20\%}}$	$8.57_{-11\%}$
		$N = 20$	3.15	2.52	3.56	5.35	$3.65_{-19\%}$	$8.36_{-13\%}$
		$N = 30$	3.18	2.48	3.48	5.28	$3.60_{-20\%}$	$\mathbf{8.26_{-14\%}}$
		$N = 50$	3.20	2.57	**3.46**	5.19	$3.61_{-20\%}$	$8.96_{-7\%}$

Table 5.6: Registration error for 9 tracked spot-like structures for four real image sequences using the three variants of the multi-frame approach with temporal weighting based on image similarity and the pairwise approach. Percentages indicate the change compared to pairwise registration.

ues for the grid spacing and used the grid with the best result. In Fig. 5.9 we show an example of the registration error for a spot-like structure in image sequence B using the temporal groupwise registration approach in comparison to our multi-frame symmetric weighting approach ($N = 10$, with temporal weighting based on image similarity). It can be seen, that the temporal groupwise registration approach yields the lowest errors for time points in about the middle of the sequence, which is what we expect since the

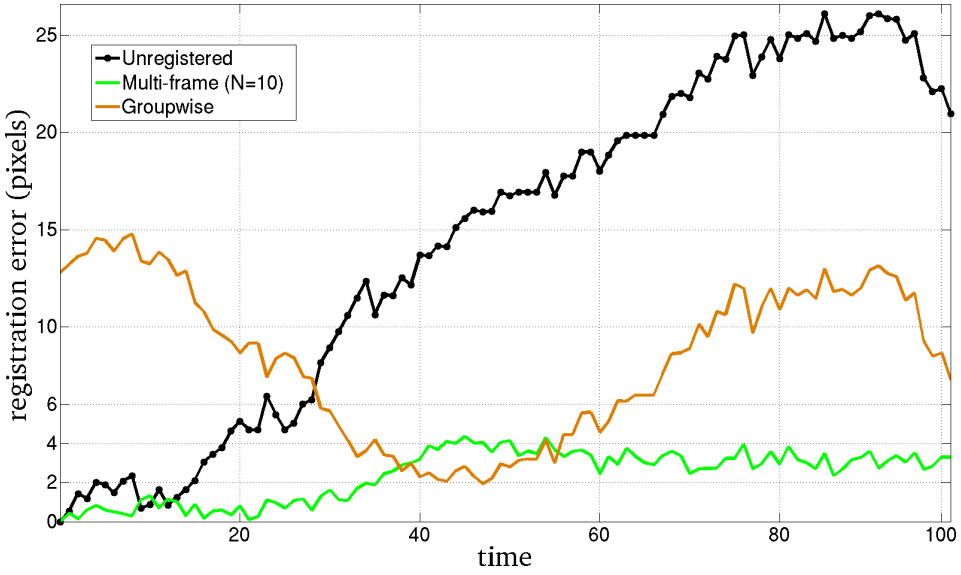

Figure 5.9: Registration error for one spot-like structure in the real image sequence B as a function of time for the temporal groupwise approach of Metz et al. [12] and the multi-frame symmetric weighting approach ($N = 10$).

images at these time points are most similar to the mean image. However, for time points away from the middle time point the error increases strongly. In comparison, our multi-frame registration approach yields significantly lower errors (except for time points in the middle) and the variation of the errors is smaller over the image sequence. The mean error for the temporal groupwise approach computes to $e_{mean} = 8.38$ pixel, while our approach yields a significantly lower error of $e_{mean} = 2.34$ pixel. When considering all 9 spot-like structures for image sequence B, the temporal groupwise approach yields $\overline{e}_{mean} = 8.38$ pixel (same value as before), while for our approach we obtain $\overline{e}_{mean} = 2.40$ pixel (cf. Table 5.4). We also computed the mean error over all four real image sequences (analogously to the result in Table 5.6). The temporal groupwise approach yields $\overline{e}_{mean} = 12.91$ pixel and for our approach we obtain $\overline{e}_{mean} = 3.57$ pixel. Thus our approach yields a better result.

The computation time for the multi-frame registration approach is proportional to the chosen number of frames N. We determined the computation time for 100 images of the live cell microscopy image sequence B with a size of 384 $\times$ 384 pixels. The

experiments were run on a workstation under Linux with an Intel Xeon E5530 CPU (2.4 GHz). The computation time for the pairwise weighting approach was 40 min, while the multi-frame weighting approach with $N = 3, 10$, and 30 took 1 h 16 min, 4 h 26 min, and 12 h 49 min, respectively. Note, that our implementation is currently not parallelized and further optimization is possible, thus the computation time can be further reduced.

5.3 Diffeomorphic Non-Rigid Multi-Frame Registration

In this section, we present experimental results for the diffeomorphic multi-frame non-rigid registration approach described in Chapter 4.

5.3.1 Parameter Setting

For our diffeomorphic multi-frame non-rigid registration approach the same parameter setting was used for all 2D and 3D image data. We have determined the parameter setting based on the real and synthetic image sequences (see Sections 5.3.2 and 5.3.3). We first used an extensive range of parameter values for one real image sequence. Then, the result for the other image sequences was checked and a subset of the parameters was refined. Finally, this parameter setting was applied for all real and synthetic data in our experiments. The evaluation was based on the minimization of the registration errors and also the smoothness of the computed transformations was taken into account. Generally, a certain amount of smoothness is necessary, however, too strong smoothing results in over-smoothing. Below, we provide the parameters for the 3D case, the parameters for the 2D case are obtained by omitting the z-dimension. For computing the velocity vector field $\mathbf{v}_{k,k-1}$ in (4.8) we have used a maximum number of 10 iterations and a threshold of 0.0001 for the sum of squared intensity differences in (3.4) (in most cases

the maximum number of iterations was used since the threshold is relatively small), and for regularization of the computed deformation vector field we have used the flow boundary preserving operator ($\sigma_{dist} = 5$ voxel, $\sigma_{int} = 7$, $5 \times 5 \times 3$ voxel neighborhood for Ω_{FB}) at flow boundaries combined with Gaussian smoothing with standard deviation $\sigma_G = (2, 2, 1)$ voxel (for the x-, y-, and z-dimension, respectively, we used a kernel size of $7 \times 7 \times 5$ voxel) in other image parts (see Section 4.5 above). For regularization of the deformation vector fields $\mathbf{u}_{l,k-1}$ in (4.4) and $\mathbf{u}_{k,1}$ in (4.2) we have used the flow boundary preserving operator ($\sigma_{dist} = 2$ voxel, $\sigma_{int} = 4$, $5 \times 5 \times 3$ voxel neighborhood for Ω_{FB}) combined with a Gaussian kernel of $\sigma_G = (1, 1, 0.5)$ voxel (we used a kernel size of $5 \times 5 \times 3$ voxel). We found, that less strong smoothing of these deformation vector fields compared to smoothing of the computed vector field in (4.8) generally improves the result. This is expected, since the deformation vector fields in (4.4) and (4.2) are based on the composition of transformations which are represented by already smoothed deformation vector fields. The update field in (4.8) was regularized using a Gaussian kernel with $\sigma_G = (2, 2, 1)$ voxel since for this vector field the flow boundary preserving method did not yield a significant improvement but requires more computation time. For the 3D data we reduced the smoothing strength (size of the operators) w.r.t. the z-dimension because of the lower resolution compared to the x- and y-dimensions. We found, that this generally improves the result. In (4.10) we used the two first terms of the Baker-Campbell-Hausdorff formula (as suggested in [10]) since adding more terms did not significantly change the result. For computing the update vector $\mathbf{V}$ in (3.11) a $5 \times 5 \times 3$ voxel neighborhood was used.

For optimizing the parameter values we mainly used one real image sequence. Using this parameter setting, the result for other real image sequences (e.g., see the sensitivity analysis for the parameters σ_{dist} and σ_{int} in Section 5.3.3) as well as for the synthetic image sequences was checked and a subset of the parameters was refined. Then this parameter setting was applied for all real and synthetic data in our experiments (i.e., we

did not tune the parameters for single image sequences). Note that the synthetic data is quite different from the real data (e.g., higher noise level and intensity scaling, see Section 5.3.2). Generally, the optimal parameter setting depends on different factors, for example, the cell motion, the cell deformations, the noise level, and the intensity changes.

5.3.2 Synthetic Image Data

In this section, we describe experimental results of our diffeomorphic multi-frame registration approach for synthetic 2D and 3D image data. To simulate the motion and deformation of cell nuclei over time, we have generated four 2D (denoted by S1, S2, S3, S4) and two 3D (denoted by S5, S6) synthetic image sequences using the first frame of the different real microscopy image sequences (sequences A-D for 2D and sequences E, F for 3D, see Table 5.1) and computed registration results. An advantage of the generated image sequences is that we have ground truth for the evaluation and that the image quality is similar to real data. We used the first image g_1 from the nucleus channel of a real image sequence as well as the transformations $\phi_{1,k}$:

$$\phi_{1,k} = \phi_{k,k-1}^{-1} \circ \phi_{1,k-1}, \tag{5.3}$$

which are obtained based on the previously computed inverse transformations $\phi_{k,k-1}^{-1}$. The used inverse deformation fields were computed using the pairwise weighting variant of our diffeomorphic non-rigid registration approach. To generate the synthetic data, we used the smoothed transformation $\phi_{1,k}$ to transform g_1 yielding an image $g_k^\bullet$ for each time point k of an image sequence:

$$g_k^\bullet = \phi_{1,k} \circ g_1. \tag{5.4}$$

We have applied our multi-frame registration approach to the synthetic data and

compared for each time point the computed vector field with the ground truth vector field. As performance measure we used the endpoint error (EE) which is defined as the Euclidean distance between the vectors of the computed vector field and the ground truth vector field (see Eq. (5.2)). For each time point we determined the mean endpoint error EE_{mean} over all computed vectors of a cell nucleus. For our approach we used different numbers of multiple frames ($N = 3, 5, 10, 20$) and compared the results with pairwise registration ($N = 2$), for the weighting as well as for the symmetric weighting registration approach.

As an example, in Fig. 5.10(a) the result of the mean registration error EE_{mean} over time for a 3D synthetic image sequence using the diffeomorphic multi-frame weighting registration approach is shown. It can be seen, that the multi-frame approach yields a lower registration error compared to pairwise registration, for all values of N. The improvement for the registration error compared to pairwise registration is 9%, 15%, 19%, and 20%, for $N = 3$, 5, 10, and 20, respectively. The registration error for our weighting approach averaged over all time points of each image sequence ($\overline{EE}_{mean}$) and over the four 2D and the two 3D synthetic image sequences for different values of N is shown in Table 5.7 (columns "Original synthetic sequences"). It can be seen, that the error using multiple frames ($N \geq 3$) is lower for all N compared to the pairwise registration ($N = 2$), for the 2D as well as for the 3D case. In both cases, the result improves with increasing N, and the lowest error is obtained for $N = 20$. The improvement is 30% for the 2D image data and 17% for the 3D image data, compared to pairwise registration. In addition, the registration error for our multi-frame symmetric weighting approach for $N = 10$ and pairwise registration is also shown in Table 5.7. It can be seen, that the improvement for the multi-frame registration compared to pairwise registration is very similar with the improvement for the weighting approach (32% and 18%, for the 2D data and for the 3D data, respectively). An example of EE_{mean} over time for a 2D synthetic image sequence using the weighting and the symmetric weighting registration

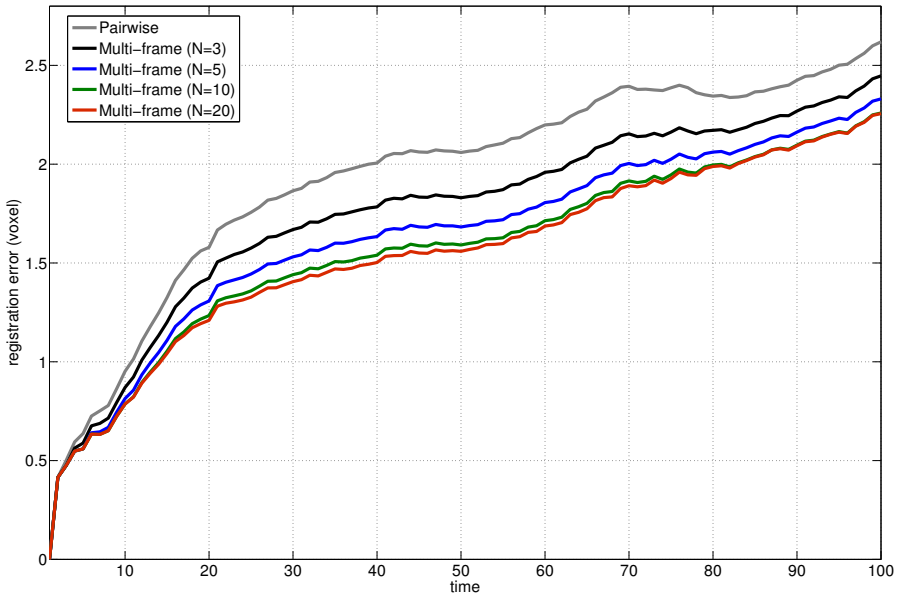

(a) 3D original synthetic sequence S6

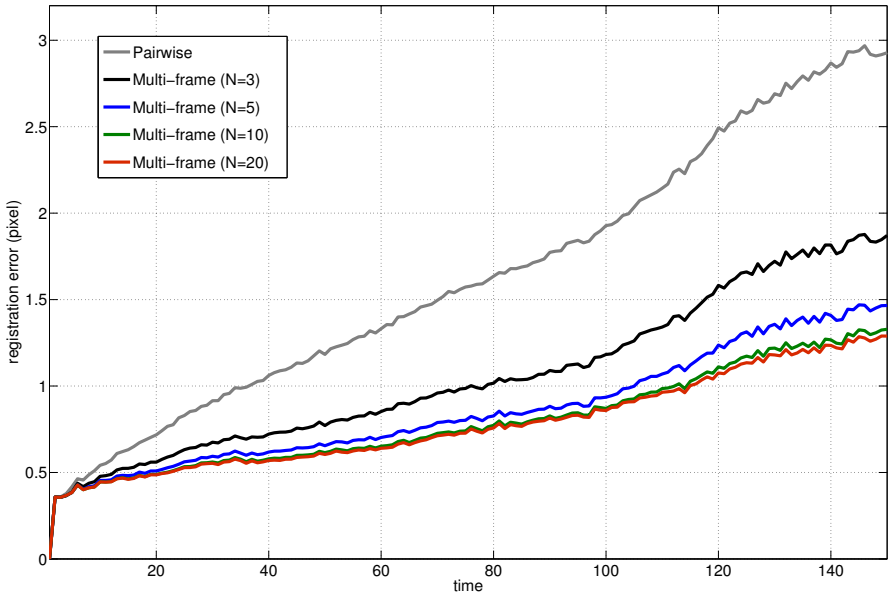

(b) 2D synthetic sequence S1 with Gaussian noise

Figure 5.10: Mean registration error EE_{mean} for a 2D and a 3D synthetic sequence as a function of time for multi-frame registration (for different values of $N \geq 3$) and pairwise registration ($N = 2$). The weighting approach was used.

[pixel] / [voxel]		Original synthetic sequences		Sequences with Gaussian noise		Sequences with linear intensity decrease and Gaussian noise	
		2D	3D	2D	3D	2D	3D
Weighting							
pairwise		2.05	2.41	2.87	2.55	4.28	2.84
multi-frame	$N = 3$	$1.65_{-19\%}$	$2.21_{-8\%}$	$2.26_{-21\%}$	$2.33_{-9\%}$	$3.19_{-25\%}$	$2.49_{-12\%}$
	$N = 5$	$1.51_{-26\%}$	$2.09_{-13\%}$	$1.94_{-32\%}$	$2.18_{-15\%}$	$2.78_{-35\%}$	$2.31_{-19\%}$
	$N = 10$	$1.47_{-28\%}$	$2.02_{-16\%}$	$1.73_{-40\%}$	$2.08_{-18\%}$	$2.66_{-38\%}$	$2.24_{-21\%}$
	$N = 20$	$\mathbf{1.44}_{-30\%}$	$\mathbf{2.01}_{-17\%}$	$\mathbf{1.66}_{-42\%}$	$\mathbf{2.05}_{-20\%}$	$\mathbf{2.65}_{-38\%}$	$\mathbf{2.23}_{-22\%}$
Symmetric weighting							
pairwise		2.14	2.44	2.94	2.59	4.12	2.88
multi-frame (N=10)		$1.45_{-32\%}$	$2.01_{-18\%}$	$1.71_{-42\%}$	$2.06_{-20\%}$	$2.68_{-35\%}$	$2.24_{-22\%}$

Table 5.7: Mean endpoint error $\overline{EE}_{mean}$ averaged over four 2D and two 3D synthetic image sequences for the new diffeomorphic multi-frame registration approach and its pairwise variant. Percentages indicate the change compared to pairwise registration and bold values indicate the lowest error. The detailed error values for each image sequence can be found in Table 5.9.

approach is shown in Fig. 5.11. It can be seen, that the errors over time are very similar for the two multi-frame approaches, as well as for the two pairwise approaches.

We also studied synthetic image data with added Gaussian noise (standard deviation $\sigma_n = 3$ voxel). The results are provided in Table 5.7 (columns "Sequences with Gaussian noise"). It can be seen, that the error increases compared to the data without noise (as expected), but also in this case the multi-frame weighting approach (for all values of N) and the multi-frame symmetric weighting approach (for $N = 10$) outperform the respective pairwise registration (for the 2D as well as for the 3D image data). Averaging the errors over the four 2D image sequences and the two 3D image sequences, the best result for the multi-frame weighting approach is obtained for $N = 20$. The improvements are 42% and 20% for the 2D and the 3D image data, respectively. For the multi-frame symmetric weighting approach ($N = 10$) the improvements w.r.t. pairwise registration

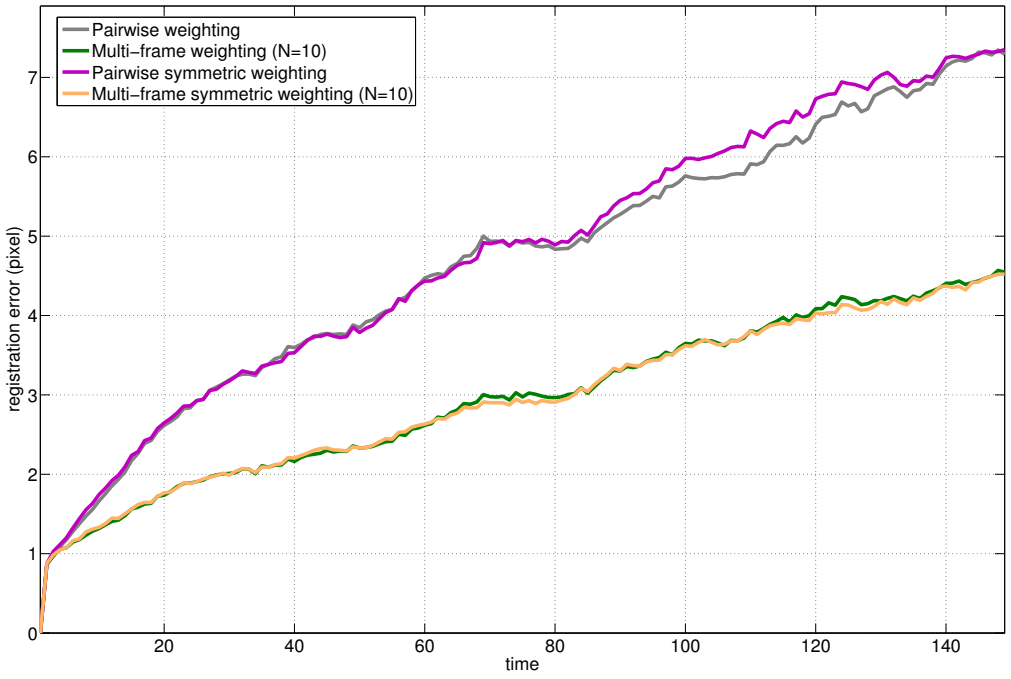

Figure 5.11: Mean registration error EE_{mean} for the 2D synthetic sequence S4 as a function of time applying our diffeomorphic multi-frame weighting and symmetric weighting registration approach (for $N = 10$) and pairwise registration ($N = 2$).

are 42% and 20% for the 2D and the 3D image data, respectively. Also for the synthetic image sequences with Gaussian noise the errors for the symmetric weighting approach are similar with the errors for the weighting approach. In Fig. 5.10(b) we show an example of the registration error over time for a 2D synthetic sequence with Gaussian noise. It can be seen, that the multi-frame weighting approach yields a better result than pairwise registration for all time points, and the improvement increases with increasing N (for $N = 20$ the improvement is 52%). For visual inspection of the results we show a 2D and a 3D example for a cropped region of a ground truth and the computed inverse vector field using the pairwise and the multi-frame weighting approach for $N = 10$ (Figs. 5.12 and 5.13). It can be seen, that in both examples the computed vectors using the diffeomorphic multi-frame approach are more similar to the ground truth vectors compared to pairwise registration, where the vectors are very different from the ground truth.

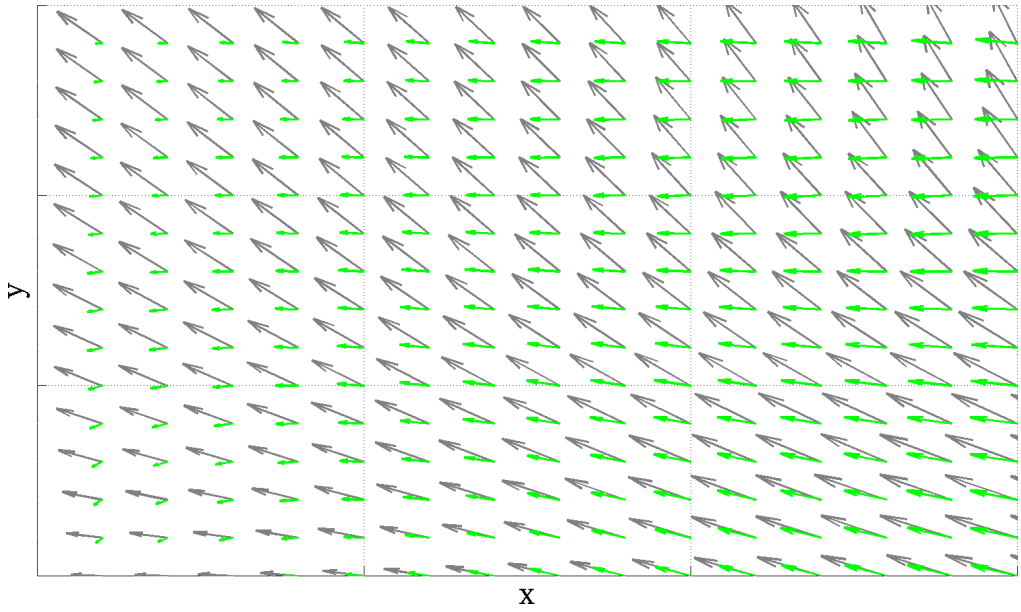

(a) Ground truth vectors and vectors for the pairwise approach

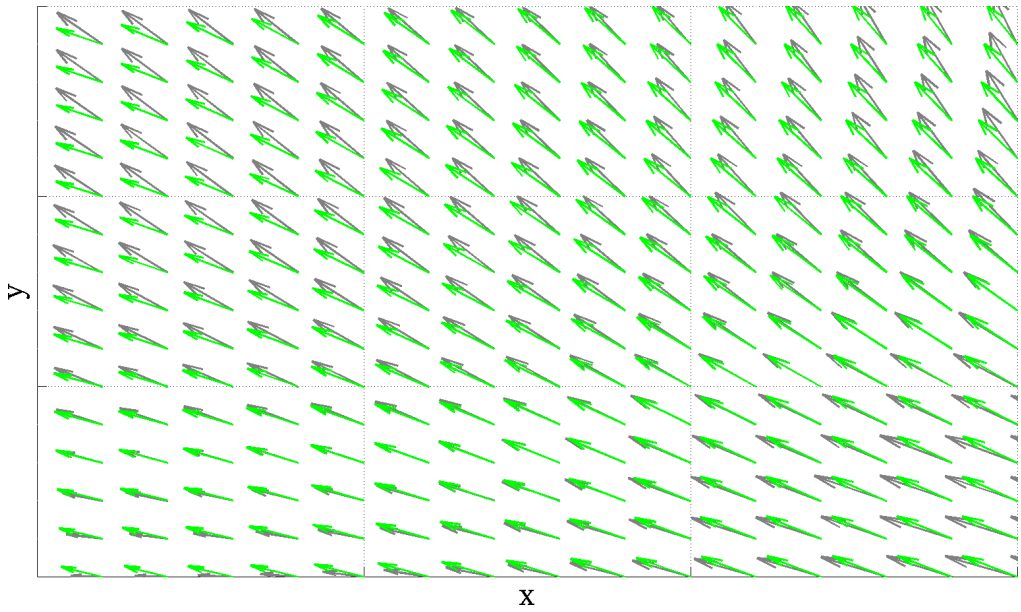

(b) Ground truth vectors and vectors for the multi-frame ($N = 10$) approach

Figure 5.12: Region of the ground truth inverse deformation vector field for the 3D synthetic sequence S5 with Gaussian noise for $t = 50$ (gray arrows) and computed inverse vector field (green arrows) using the diffeomorphic pairwise registration approach (a) and the symmetric weighting diffeomorphic multi-frame registration approach (b).

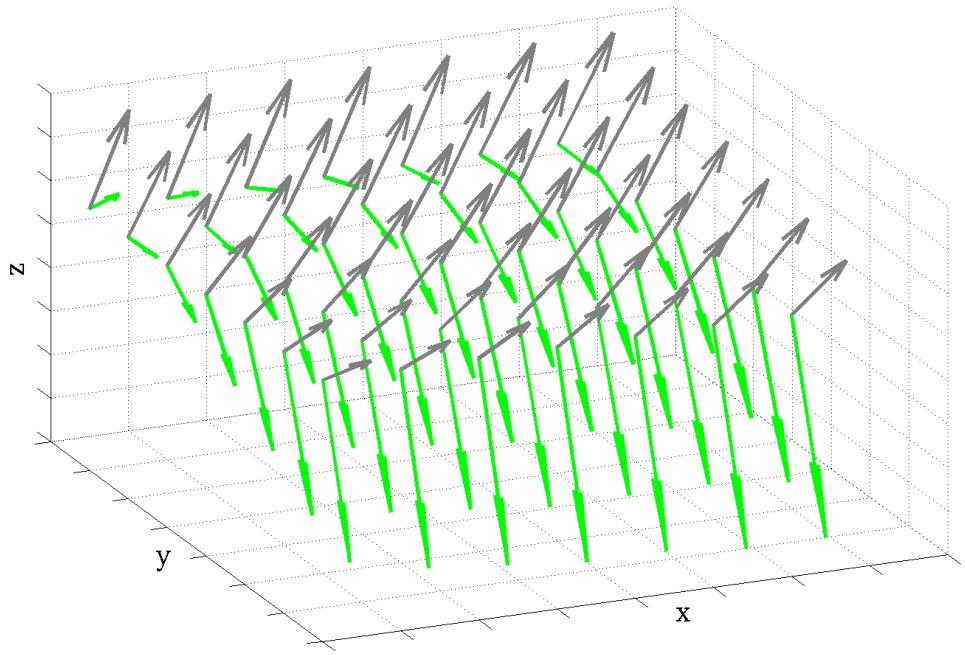

(a) Ground truth vectors and vectors for the pairwise approach

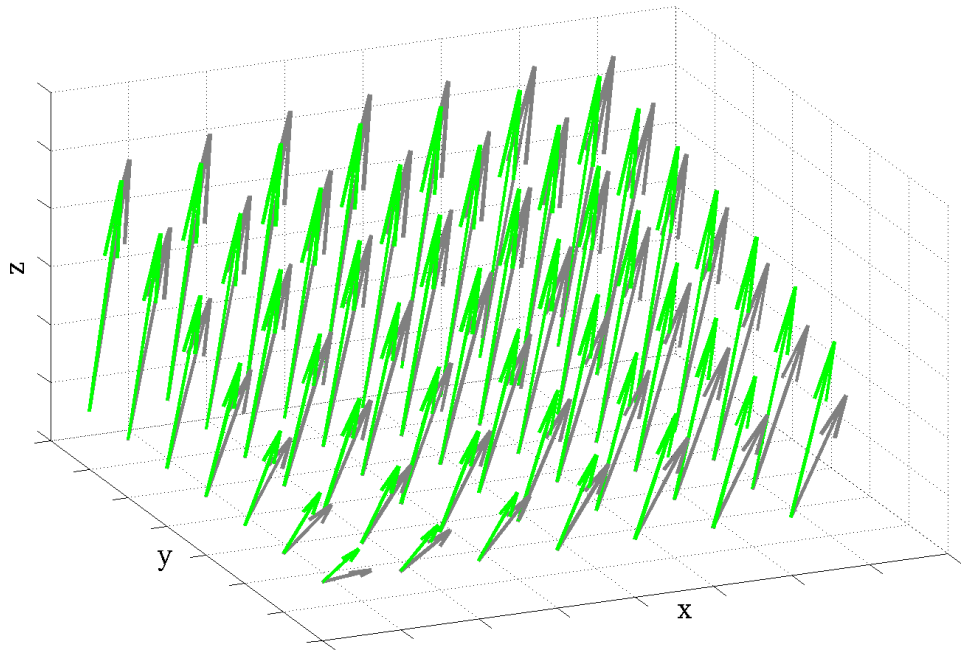

(b) Ground truth vectors and vectors for the multi-frame ($N = 10$) approach

Figure 5.13: Region of the ground truth inverse deformation vector field for the 3D synthetic sequence S5 with Gaussian noise for $t = 50$ (gray arrows) and computed inverse vector field (green arrows) using the diffeomorphic pairwise registration approach (a) and the weighting diffeomorphic multi-frame registration approach (b).

To simulate photobleaching in fluorescence microscopy image sequences, we also generated data where the image intensities are linearly scaled over time. We used a scaling factor $\lambda_k = 1 - 0.001k$, i.e. the intensities are linearly decreased by 10% for every 100 time points (we have determined this value based on the real image data). In addition, to introduce a random component, the scaling factor λ_k was multiplied by a uniformly distributed random factor ρ_k ($0.95 \leq \rho_k \leq 1.05$) which is determined for each time point independently. We also added Gaussian noise with $\sigma_n = 3$ voxel. Note, that photobleaching is difficult to simulate, since the scale of the intensity decrease is different for the different molecules. The results for these synthetic image sequences can be found in Table 5.7 (last two columns). We can observe, that the diffeomorphic multi-frame weighting approach (for all values of N) and the multi-frame symmetric weighting approach (for $N = 10$) outperform the respective pairwise registration (for the 2D as well as for the 3D image data). The best result for the weighting approach is obtained for $N = 20$ for the 2D and the 3D data, and the improvement is 38% and 22%, respectively. The results of the symmetric weighting approach are very similar with the results of the weighting approach, and the improvement compared to pairwise registration is 35% and 22% for the 2D and for the 3D data, respectively. Interestingly, the error for the 3D data is smaller compared to the 2D data. The reason for this is that the linear intensity decrease is a *global* change of an image, and for 3D data there are more measurements compared to the 2D data. Therefore, the registration approach can cope better with the intensity changes. In Fig. 5.14 an example of EE_{mean} over time for a 3D synthetic sequence with linear intensity decrease and added Gaussian noise is shown. We can observe, that the multi-frame approach for all values of N outperforms the pairwise approach. The lowest value of $\overline{EE}_{mean}$ is obtained for $N = 10$, yielding an improvement of 19%.

To investigate whether the improvement of the diffeomorphic multi-frame approach compared to pairwise registration in Table 5.7 is statistically significant, we performed

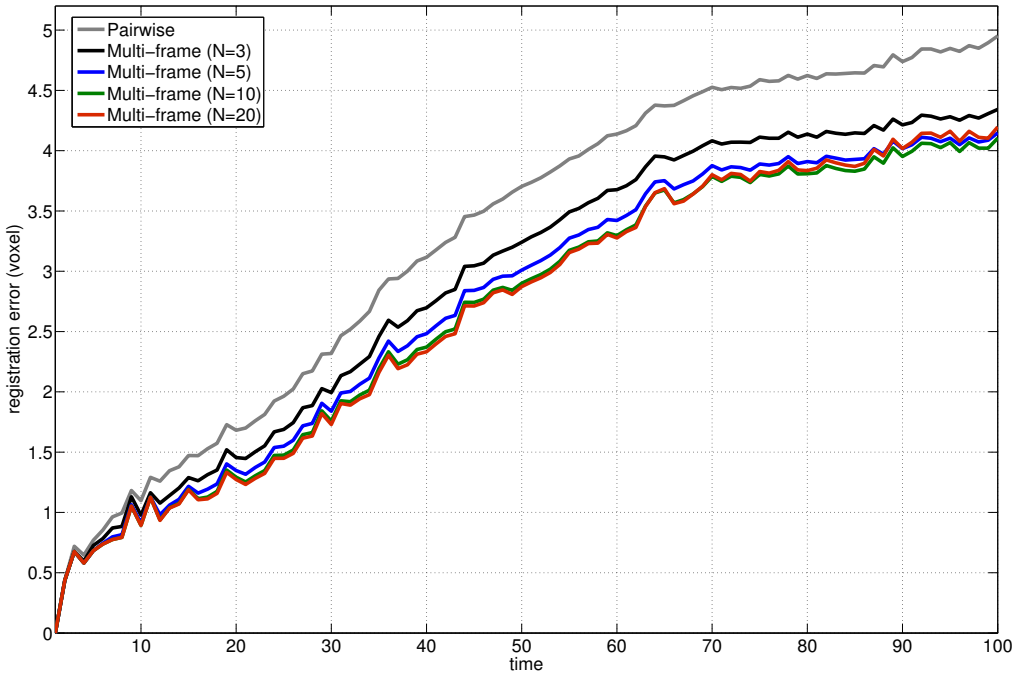

Figure 5.14: Mean registration error EE_{mean} for a 3D synthetic sequences as a function of time for multi-frame registration (for different values of $N \geq 3$) and pairwise registration ($N = 2$). The weighting approach was used.

a Wilcoxon signed-rank test (non-parametric test). Prior application of a Shapiro-Wilk test showed that the data does not follow a normal distribution in all 15 cases (3 types of image sequences, 2 registration variants, 4 different values of N for the weighting variant and one value of N for the symmetric weighting variant). Using a significance level of 5% we obtained $p < 0.016$. Thus, the multi-frame approach yields a statistically significant improvement compared to pairwise registration, for both the weighting as well as for the symmetric weighting variant.

Furthermore, we quantified the influence of Gaussian noise and the linear intensity decrease scaling on the registration results for the weighting (for different values of N) as well as for the symmetric weighting approach (for $N = 10$). We compared the errors for the more difficult synthetic sequences with those for the original synthetic sequences using the values of Table 5.7. The differences in percentage can be found in Table 5.8. We can observe, that for all cases the error increased, as expected. The increase for

		Sequences with Gaussian noise		Sequences with linear intensity decrease and Gaussian noise	
		2D	3D	2D	3D
Weighting					
pairwise		+40%	+6%	+109%	+18%
multi-frame	$N = 3$	+37%	+5%	+93%	+13%
	$N = 5$	+28%	+4%	+84%	+11%
	$N = 10$	+18%	+3%	+81%	+11%
	$N = 20$	+15%	+2%	+84%	+11%
Symmetric weighting					
pairwise		+37%	+6%	+93%	+18%
multi-frame (N=10)		+18%	+2%	+85%	+11%

Table 5.8: Changes in percentage of $\overline{EE}_{mean}$ for the new diffeomorphic weighting and the symmetric weighting registration approach for the modified synthetic image sequences w.r.t. the error in the original synthetic sequences. The changes have been computed using the $\overline{EE}_{mean}$ values from Table 5.7.

the 2D data is significantly larger compared to the respective increase for the 3D image data. The reason is that for the 3D image data there are more measurements available than for the 2D data, and therefore, registration can cope better with the performed changes. In addition, it can be seen, that the increase is higher for the pairwise approach compared to the multi-frame approach, and that for most cases the percentages decrease for increasing N. This shows that the multi-frame approach is more robust to Gaussian noise and intensity scaling than the pairwise approach, and a larger N generally increases the robustness.

5.3.3 Real Image Data

We have also applied our diffeomorphic multi-frame registration approach to four 2D and two 3D real microscopy image data (image sequences A, B, C, D, E, F, see Section 5.1 above). We performed a quantitative evaluation based on manually determined

[pixels] / [voxels]	2D Sequences						3D Sequences			
	$\overline{EE}_{mean}$					$\overline{EE}_{std}$	$\overline{EE}_{mean}$			$\overline{EE}_{std}$
	S1	S2	S3	S4	Average	Average	S5	S6	Average	Average
Original synthetic sequences										
Weighting										
pairwise	1.38	1.63	2.54	2.64	2.05	0.84	2.88	1.94	2.41	0.90
multi-frame $N = 3$	0.92	1.21	2.18	2.30	$1.65_{-19\%}$	$0.64_{-23\%}$	2.66	1.76	$2.21_{-8\%}$	$0.83_{-7\%}$
multi-frame $N = 5$	0.77	1.10	2.02	2.16	$1.51_{-26\%}$	$0.59_{-30\%}$	2.54	1.64	$2.09_{-13\%}$	$0.80_{-11\%}$
multi-frame $N = 10$	0.75	1.08	1.95	2.09	$1.47_{-28\%}$	$0.58_{-31\%}$	2.47	1.57	$2.02_{-16\%}$	$\mathbf{0.78}_{-13\%}$
multi-frame $N = 20$	**0.75**	**1.07**	**1.89**	**2.06**	$\mathbf{1.44}_{-30\%}$	$\mathbf{0.57}_{-31\%}$	**2.47**	**1.55**	$\mathbf{2.01}_{-17\%}$	$0.79_{-12\%}$
Symmetric weighting										
pairwise	1.41	1.66	2.66	2.84	2.14	0.89	2.93	1.96	2.44	0.91
multi-frame (N=10)	0.73	1.09	1.91	2.10	$1.45_{-32\%}$	$0.57_{-36\%}$	2.45	1.56	$2.01_{-18\%}$	$0.78_{-14\%}$
Sequences with Gaussian noise										
Weighting										
pairwise	1.63	2.00	3.15	4.68	2.87	1.19	2.97	2.12	2.55	0.94
multi-frame $N = 3$	1.06	1.48	2.53	3.96	$2.26_{-21\%}$	$0.91_{-24\%}$	2.74	1.91	$2.33_{-9\%}$	$0.88_{-7\%}$
multi-frame $N = 5$	0.86	1.28	2.20	3.44	$1.94_{-32\%}$	$0.76_{-36\%}$	2.60	1.75	$2.18_{-15\%}$	$0.84_{-11\%}$
multi-frame $N = 10$	0.79	1.17	2.02	2.94	$1.73_{-40\%}$	$0.65_{-45\%}$	2.51	1.65	$2.08_{-18\%}$	$0.81_{-14\%}$
multi-frame $N = 20$	**0.78**	**1.14**	**1.93**	**2.78**	$\mathbf{1.66}_{-42\%}$	$\mathbf{0.61}_{-48\%}$	**2.48**	**1.62**	$\mathbf{2.05}_{-20\%}$	$\mathbf{0.80}_{-15\%}$
Symmetric weighting										
pairwise	1.65	2.02	3.33	4.77	2.94	1.24	3.04	2.14	2.59	0.97
multi-frame (N=10)	0.78	1.15	1.98	2.93	$1.71_{-42\%}$	$0.65_{-48\%}$	2.49	1.64	$2.06_{-20\%}$	$0.80_{-18\%}$
Sequences with linear intensity decrease and Gaussian noise										
Weighting										
pairwise	3.22	4.49	4.20	5.21	4.28	1.51	3.29	2.40	2.84	1.04
multi-frame $N = 3$	2.08	3.16	3.35	4.18	$3.19_{-25\%}$	$1.14_{-24\%}$	2.92	2.07	$2.49_{-12\%}$	$0.92_{-11\%}$
multi-frame $N = 5$	1.77	2.64	3.02	3.70	$2.78_{-35\%}$	$1.01_{-33\%}$	2.74	1.88	$2.31_{-19\%}$	$0.86_{-17\%}$
multi-frame $N = 10$	1.66	2.46	2.85	**3.66**	$2.66_{-38\%}$	$\mathbf{1.01}_{-33\%}$	2.67	1.81	$2.24_{-21\%}$	$\mathbf{0.84}_{-18\%}$
multi-frame $N = 20$	**1.63**	**2.45**	**2.80**	3.69	$\mathbf{2.65}_{-38\%}$	$1.03_{-32\%}$	**2.67**	**1.79**	$\mathbf{2.23}_{-22\%}$	$0.86_{-17\%}$
Symmetric weighting										
pairwise	2.95	4.02	4.11	5.39	4.12	1.51	3.30	2.46	2.88	1.04
multi-frame (N=10)	1.55	2.38	2.86	3.92	$2.68_{-35\%}$	$1.08_{-29\%}$	2.62	1.86	$2.24_{-22\%}$	$0.83_{-20\%}$

Table 5.9: Detailed mean endpoint error $\overline{EE}_{mean}$ values for the 2D and 3D synthetic image sequences in Table 5.7 applying our diffeomorphic registration approach.

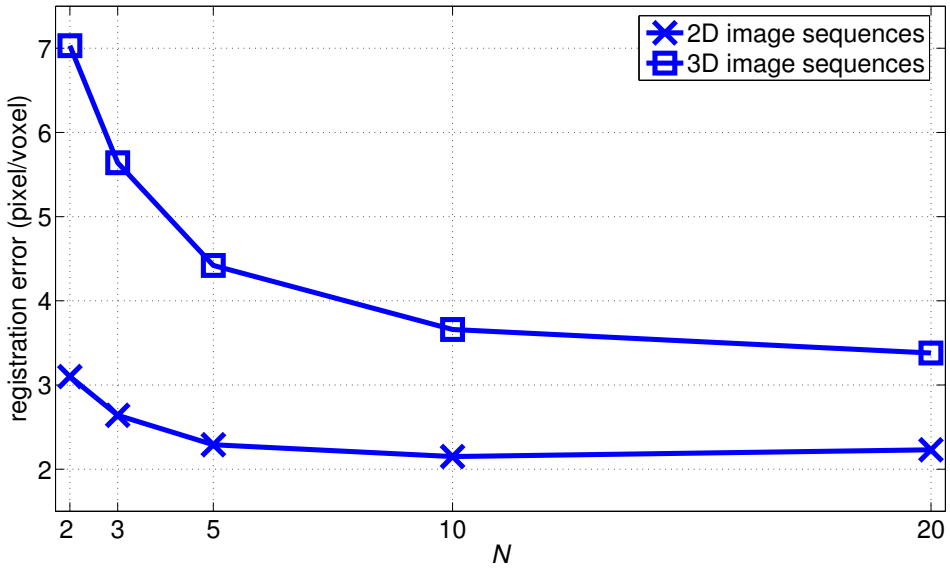

Figure 5.15: Mean registration error ($\overline{e}_{mean}$) averaged over all spot-like structures of all four 2D image sequences as a function of N.

structures in the nucleus channel of the image sequences. For each sequence of the 2D image data, positions of 9 spot-like structures within cell nuclei were determined for 38 up to 125 subsequent time points, and for the 3D data positions of 6 spot-like structures were determined for 28 up to 83 subsequent time points. For each structure and each time point we computed the registration error as the Euclidean distance of the current position (center of gravity) to its position at the first time point.

For our diffeomorphic multi-frame weighting approach we used different numbers of multiple frames ($N = 3, 5, 10, 20$) and we computed for each spot-like structure the mean registration error e_{mean} over all time points. The results for the mean error averaged over all spot-like structures for the four 2D and the two 3D image sequences ($\overline{e}_{mean}$) are shown in Fig. 5.15 as a function of N. It can be seen, that for the 2D data the multi-frame approach with $N = 3$ yields a lower error than the pairwise approach, and the error is further reduced by increasing N up to $N = 10$, where the error reaches its minimum. For $N = 20$ the error is slightly higher. Similarly, for the 3D data the error decreases with increasing N, and the lowest error is reached for $N = 20$.

In Table 5.10 we show the results for $\overline{e}_{mean}$ for each 2D and each 3D real image se-

[pixel] / [voxel]		2D Sequences						3D Sequences			
		$\overline{e}_{mean}$					$\overline{\sigma}_{e_{mean}}$	$\overline{e}_{mean}$			$\overline{\sigma}_{e_{mean}}$
		A	B	C	D	Average	Average	E	F	Average	Average
Unregistered		6.56	13.97	26.65	27.84	18.76	9.53	24.94	21.24	23.09	11.69
Weighting	pairwise	2.20	1.94	3.27	4.99	3.10	2.06	9.03	5.02	7.03	4.55
	multi-frame $N = 3$	2.08	1.55	2.61	4.34	$2.64_{-15\%}$	$1.88_{-9\%}$	7.66	3.62	$5.64_{-20\%}$	$3.87_{-15\%}$
	multi-frame $N = 5$	**2.06**	1.40	2.40	3.30	$2.29_{-26\%}$	$1.68_{-18\%}$	6.05	2.80	$4.42_{-37\%}$	$3.22_{-29\%}$
	multi-frame $N = 10$	2.10	**1.38**	**2.19**	2.93	$\mathbf{2.15}_{-31\%}$	$\mathbf{1.64}_{-20\%}$	4.90	2.41	$3.66_{-48\%}$	$2.66_{-41\%}$
	multi-frame $N = 20$	2.11	1.41	2.51	**2.89**	$2.23_{-28}\%$	$1.66_{-19\%}$	**4.49**	**2.27**	$\mathbf{3.38}_{-52\%}$	$\mathbf{2.44}_{-46\%}$

Table 5.10: Registration error and standard deviation for spot-like structures in four 2D real image sequences and two 3D real image sequences. Results for the diffeomorphic multi-frame weighting approach for different values of N and the pairwise variant. Percentages indicate the change compared to pairwise registration, and bold values indicate the lowest error.

quence (image sequences A-F, see Table 5.1 and Section 5.3.1) using the diffeomorphic multi-frame weighting registration approach for different values of N and the pairwise approach. We also computed the standard deviation of the mean error $\sigma_{e_{mean}}$ for each spot-like structure as well as the average over all structures and the four 2D and the two 3D image sequences ($\overline{\sigma}_{e_{mean}}$). It turned out that for all 2D and 3D image sequences our multi-frame weighting approach with $N = 3$ yields a lower error compared to pairwise registration, and the error is further reduced by increasing N up to a certain value of N. The value of N for which the result is best generally varies depending on the image sequence. For the 2D image data, the best result for $\overline{e}_{mean}$ and for $\overline{\sigma}_{e_{mean}}$ averaged over all image sequences is obtained for $N = 10$, yielding an improvement of 31% and 20%, respectively, compared to pairwise registration. For the 3D image data, the best results averaged over all image sequences are obtained for $N = 20$, yielding an improvement of 52% and 46%, respectively, compared to pairwise registration. In Fig. 5.16 we show examples of the registration error for one spot-like structure in the 2D image sequence C and for one spot-like structure in the 3D image sequence F, when applying the diffeomor-

phic multi-frame weighting registration approach with different values of N. It can be seen, that for both examples the multi-frame approach yields a better result compared to the pairwise approach (grey line) and the error generally decreases with increasing N. We also computed the mean registration error e_{mean} over all time points. It turns out, that for the 2D example (Fig. 5.16(a)) multi-frame registration with $N = 2$ reduces e_{mean} by 57% compared to pairwise registration, and for $N = 10$ and $N = 20$ the improvement is 71% and 75%, respectively. For the 3D example (Fig. 5.16(b)), multi-frame registration with $N = 2$ reduces e_{mean} by 31% compared to pairwise registration, and for $N = 10$ and $N = 20$ the improvement is 61% and 64%, respectively. In Figs. 5.17 and 5.18 we have visualized the positions of the spot-like structures (used as ground truth) over time for the 3D image sequences E and F for the unregistered case as well as for registration using our multi-frame approach and the pairwise approach (weighting and symmetric weighting approach, for the image sequence E and F, respectively). It can be seen, that in both examples the displacements of the positions over time w.r.t. the ground truth positions at the first frame (which represent the registration error) for the multi-frame approach are much smaller compared to the unregistered case and smaller compared to pairwise registration.

To confirm that our registration approach is diffeomorphic, we have computed for each position of each 2D and 3D deformation vector field $\mathbf{u}_{k,k-1}$ the determinant of the Jacobian. It turned out, that the determinant is positive, except for a negligible number of image points (less than 0.01%) of a small number of deformation fields (less than 2%), which have a negative determinant due to discretization issues. Thus, the determined deformation fields can be considered diffeomorphic.

We also performed a study on the convergence properties of our diffeomorphic multi-frame registration approach. We computed the mean RMS and the mean CC for each iteration (we used 10 iterations) averaged over all time points of an image sequence. Fig. 5.19 shows an example for both metrics for the multi-frame and the pairwise weight-

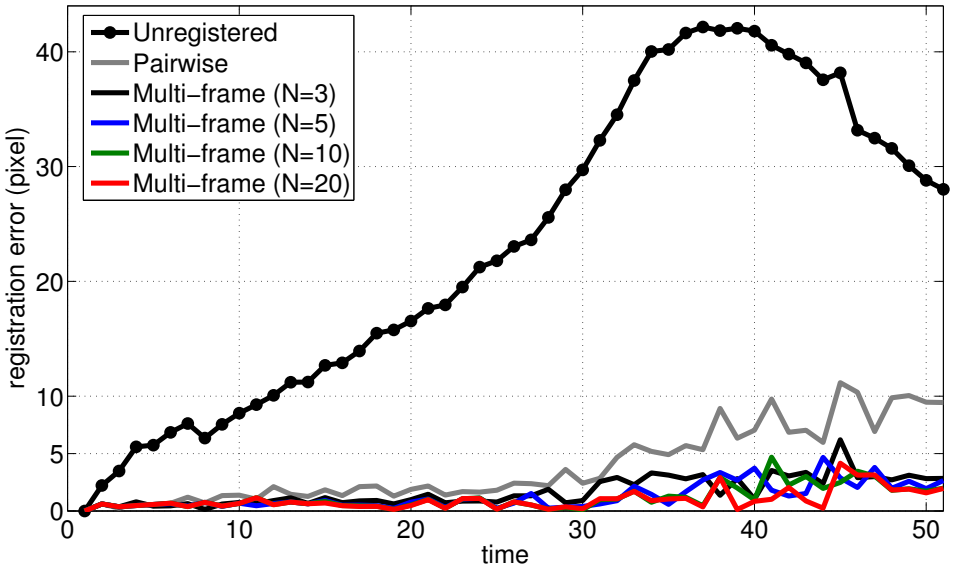

(a) 2D image sequence C

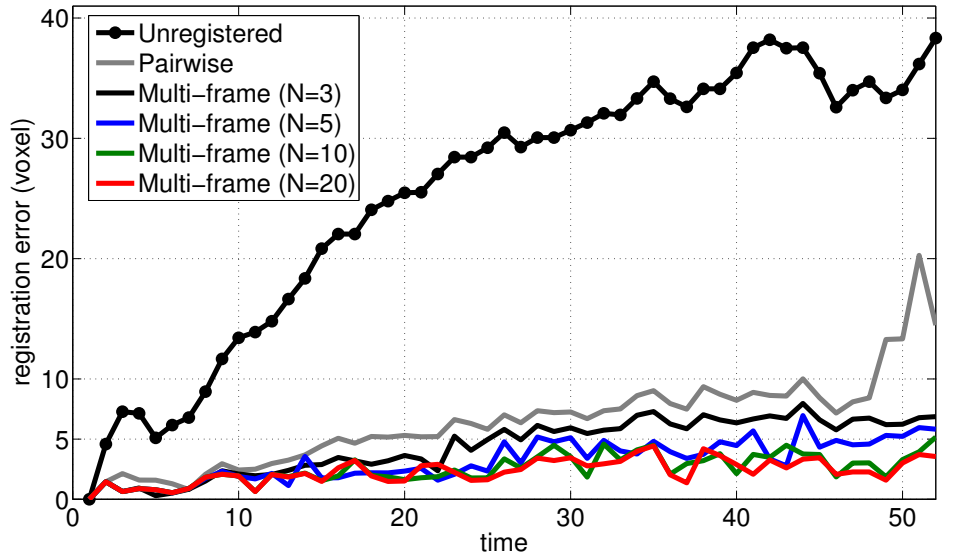

(b) 3D image sequence F

Figure 5.16: Registration error for spot-like structures in a 2D and a 3D real image sequence as a function of time for the diffeomorphic multi-frame weighting approach and its pairwise variant.

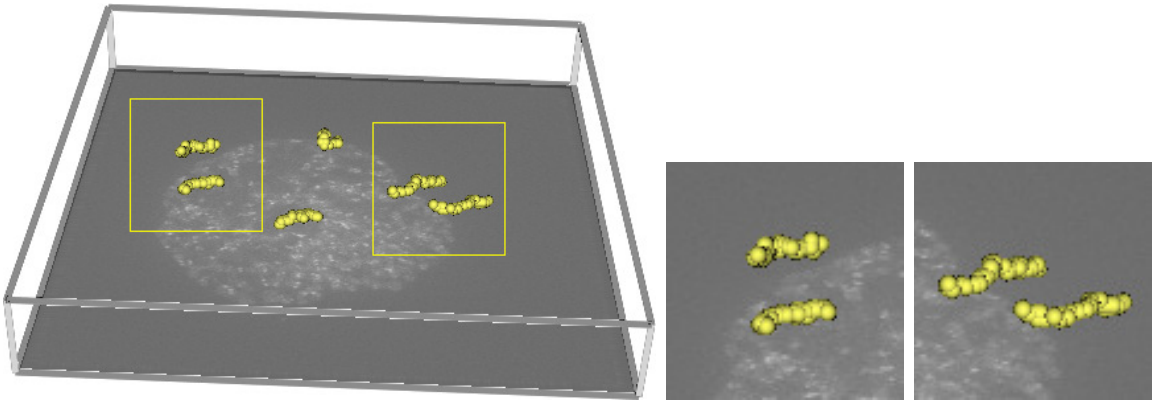

(a) Unregistered

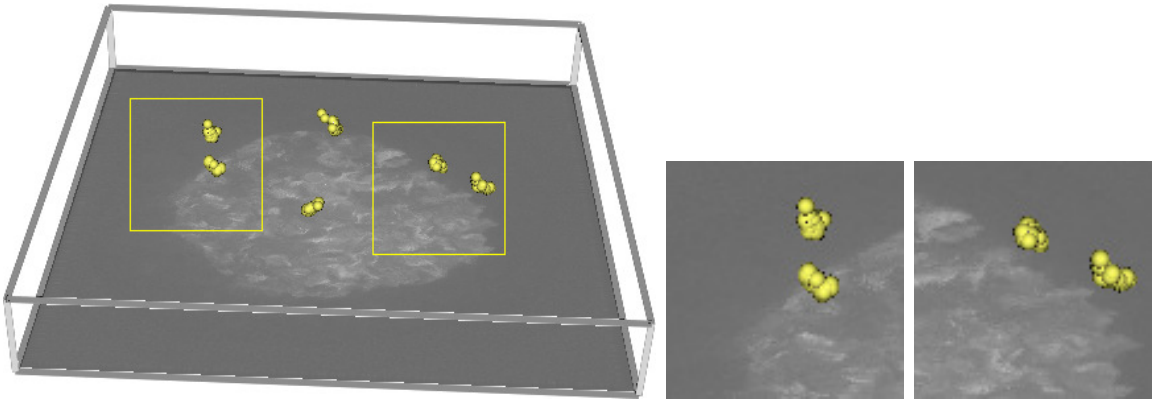

(b) Diffeomorphic pairwise weighting approach

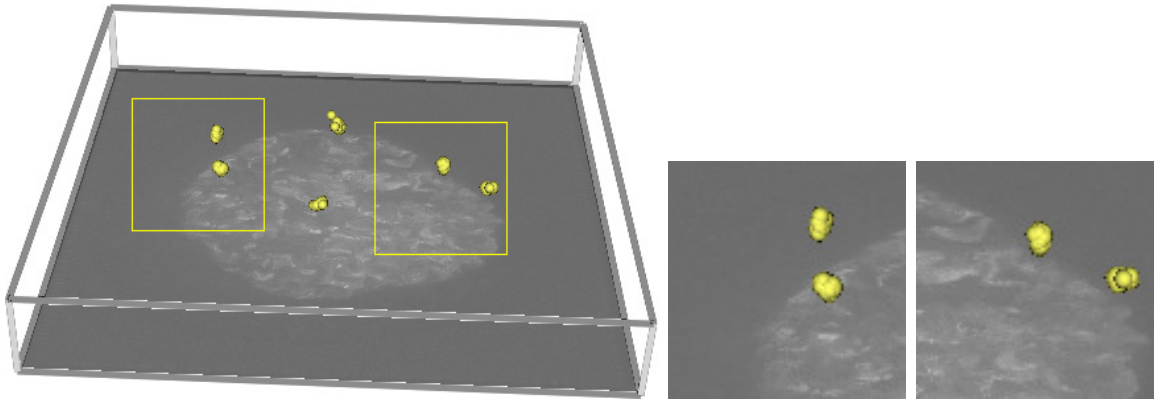

(c) Diffeomorphic multi-frame weighting approach

Figure 5.17: Positions over time for 6 spot-like structures overlaid with an MIP image ($t = 50$) from the 3D image sequence E (nucleus channel). In (a) the original image and positions over time for the unregistered case are shown, and in (b) and (c) the registered images and positions over time for the diffeomorphic multi-frame weighting approach and its pairwise variant are shown.

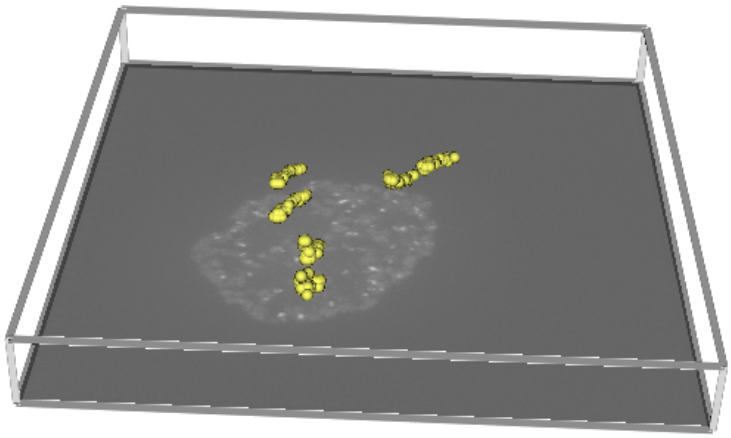

(a) Unregistered

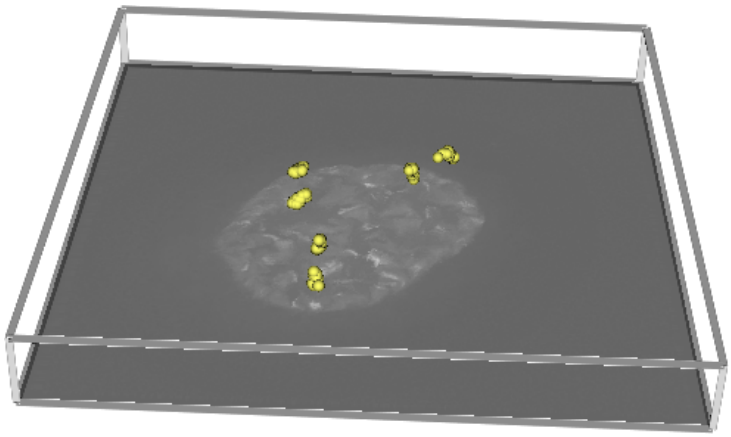

(b) Diffeomorphic pairwise symmetric weighting approach

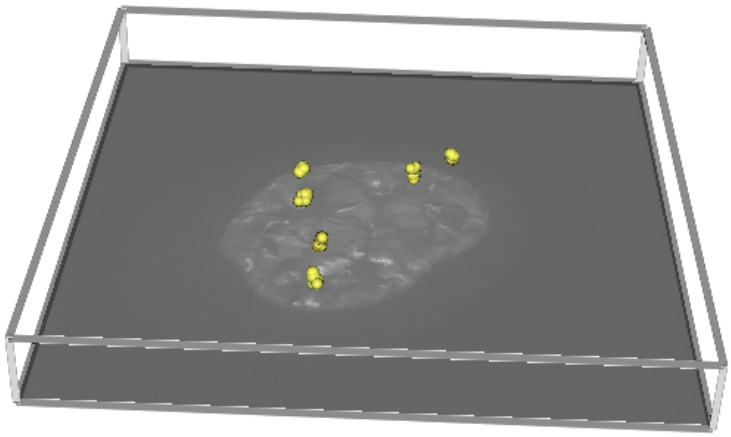

(c) Diffeomorphic multi-frame symmetric weighting approach

Figure 5.18: Positions over time for 6 spot-like structures overlaid with an MIP image ($t = 70$) from the 3D image sequence F (nucleus channel). In (a) the original image and positions over time for the unregistered case are shown, and in (b) and (c) the registered images and positions over time for the diffeomorphic multi-frame symmetric weighting approach and its pairwise variant are shown.

ing approach applied to one real image sequence. It can be seen, that the multi-frame approach (for the different values of N) and the pairwise approach converge and have a similar rate. We can also observe, that the RMS values of the multi-frame approach decrease and the CC values increase with increasing N, compared to the corresponding values of the pairwise approach. In our experiments, in most cases the number of iterations was 10 (see Sections 4.3 and 5.3.1). It can be seen that the error converges after few iterations and that a maximum number of 10 iterations is sufficient.

In Table 5.11 we show the results for $\overline{e}_{mean}$ and $\overline{\sigma}_{e_{mean}}$ for each 2D and each 3D real image sequence using the diffeomorphic multi-frame registration approach ($N = 10$) and pairwise registration, for both the weighting and the symmetric weighting variant. It turned out that the symmetric weighting approach yields larger errors for most 2D images sequences compared to the weighting approach, for both multi-frame as well as pairwise registration. For the 3D image sequences, the symmetric weighting approach yields lower errors, for both multi-frame as well as pairwise registration. However, the differences between the errors for the weighting and the symmetric weighting approach are relatively small. Compared to pairwise registration, also the multi-frame symmetric weighting approach yields lower errors and the improvement for $\overline{e}_{mean}$ and $\overline{\sigma}_{e_{mean}}$ averaged over all four 2D sequences is 30% and 21%, respectively. For the 3D image data the respective improvement for $\overline{e}_{mean}$ and $\overline{\sigma}_{e_{mean}}$ averaged over the two 3D image sequences is 51% and 44%, respectively. In Fig. 5.20 we show an example of the registration error for one spot-like structure in the 3D real image sequence E using our diffeomorphic multi-frame approach for the weighting as well as for the symmetric weighting variant, and pairwise registration. It can be seen, that the errors over time are very similar for the multi-frame weighting and for the multi-frame symmetric weighting approach. Similarly, the errors over time are very similar for the pairwise variants of the approaches.

In addition, we have performed an experimental comparison with previous non-rigid registration approaches for the 2D and 3D data. We have used the pairwise weighting

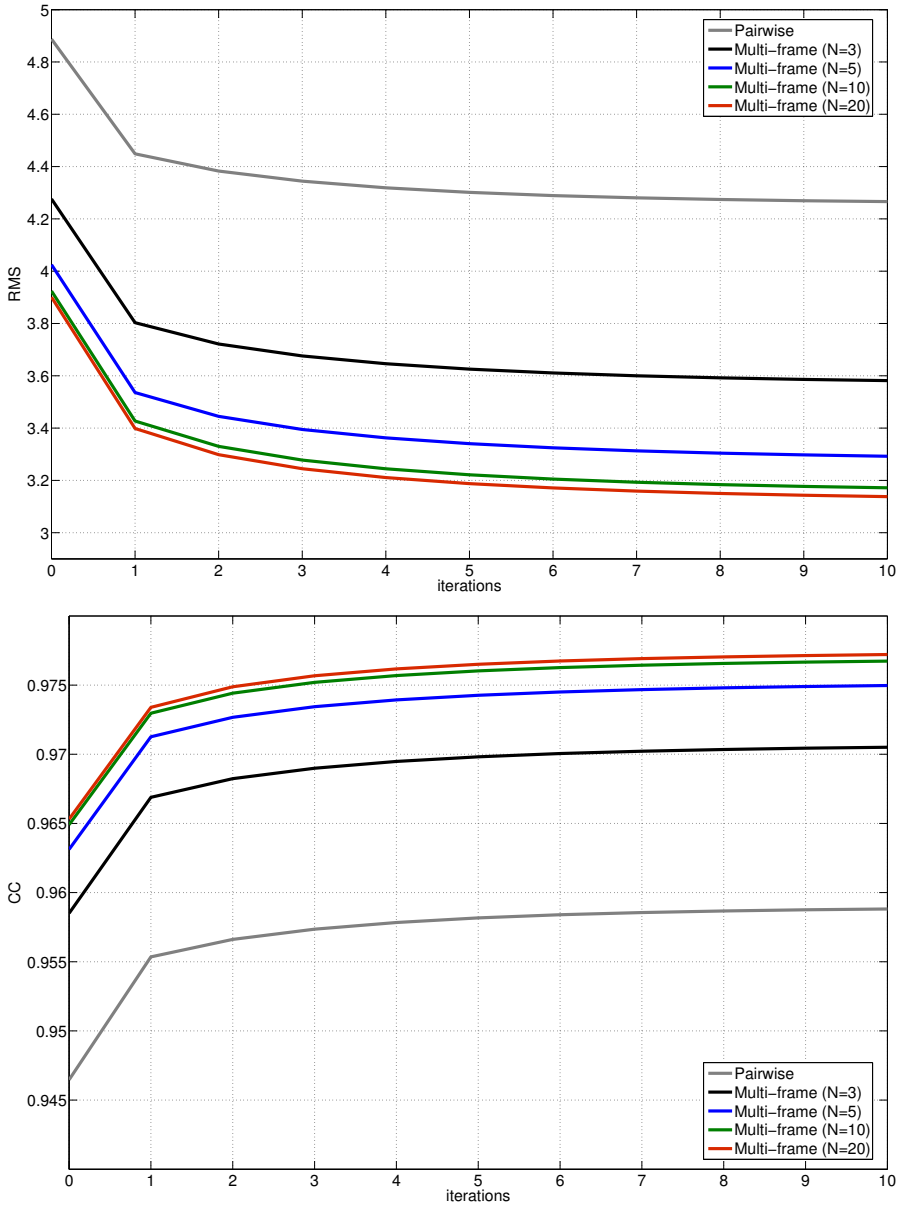

Figure 5.19: Mean of root mean squared (RMS) intensity error (top) and mean of correlation coefficient (CC, bottom) averaged over all time points for each iteration step. The multi-frame (for different values of $N \geq 3$) and the pairwise weighting approach was applied to the 3D real image sequence E.

[pixel] / [voxel]	2D Sequences						3D Sequences			
	$\overline{e}_{mean}$					$\overline{\sigma}_{e_{mean}}$	$\overline{e}_{mean}$			$\overline{\sigma}_{e_{mean}}$
	A	B	C	D	Average	Average	E	F	Average	Average
Unregistered	6.56	13.97	26.65	27.84	18.76	9.53	24.94	21.24	23.09	11.69
Pairwise weighting [11]	3.23	2.87	4.39	7.08	4.39	2.49	10.01	7.15	8.58	5.15
Multi-frame weighting [118]	2.99	2.45	3.56	5.31	$3.58_{-19\%}$	$2.11_{-15\%}$	6.98	4.63	$5.81_{-32\%}$	$3.75_{-27\%}$
Pairwise symmetric weighting [11]	3.39	2.84	4.79	6.90	4.48	2.59	9.35	6.79	8.07	4.82
Multi-frame symmetric weighting [118]	3.14	2.40	3.53	5.19	$3.57_{-20\%}$	$2.09_{-19\%}$	6.05	4.22	$5.13_{-36\%}$	$3.25_{-33\%}$
Log-Demons [10] pairwise extension	2.78	2.93	7.83	11.14	6.17	3.54	17.51	12.66	15.08	8.87
Log-Demons [10] multi-frame extension	2.31	2.47	4.11	7.55	$4.11_{-33\%}$	$2.37_{-33\%}$	13.15	8.97	$11.06_{-27\%}$	$6.96_{-22\%}$
Temporal groupwise [12]	4.78	8.38	17.20	21.29	12.91	4.69	-	-	-	-
Diffeomorphic pairwise weighting (Gaussian smoothing)	2.66	2.20	3.40	5.44	3.43	2.01	8.27	6.32	7.29	4.92
Diffeomorphic multi-frame weighting (Gaussian smoothing)	2.35	1.80	2.77	3.95	$2.72_{-21\%}$	$1.74_{-13\%}$	5.28	3.93	$4.60_{-37\%}$	$3.37_{-32\%}$
Diffeomorphic pairwise weighting	2.20	1.94	3.27	4.99	3.10	2.06	9.03	5.02	7.03	4.55
Diffeomorphic multi-frame weighting	**2.10**	1.38	**2.19**	**2.93**	$\mathbf{2.15}_{-31\%}$	$\mathbf{1.64}_{-20\%}$	4.90	2.41	$3.66_{-48\%}$	$2.66_{-41\%}$
Diffeomorphic pairwise symmetric weighting	2.22	1.76	3.93	5.13	3.26	2.17	8.43	4.73	6.58	4.22
Diffeomorphic multi-frame symmetric weighting	2.12	**1.32**	2.48	3.21	$2.28_{-30\%}$	$1.71_{-21\%}$	**4.31**	**2.18**	$\mathbf{3.25}_{-51\%}$	$\mathbf{2.38}_{-44\%}$

Table 5.11: Registration error and standard deviation for spot-like structures in four 2D real image sequences and two 3D real image sequences. Results for the diffeomorphic multi-frame weighting and symmetric weighting approach ($N = 10$) and their pairwise variants, as well as for other approaches. Percentages indicate the change compared to the corresponding pairwise registration approach, and bold values indicate the lowest error.

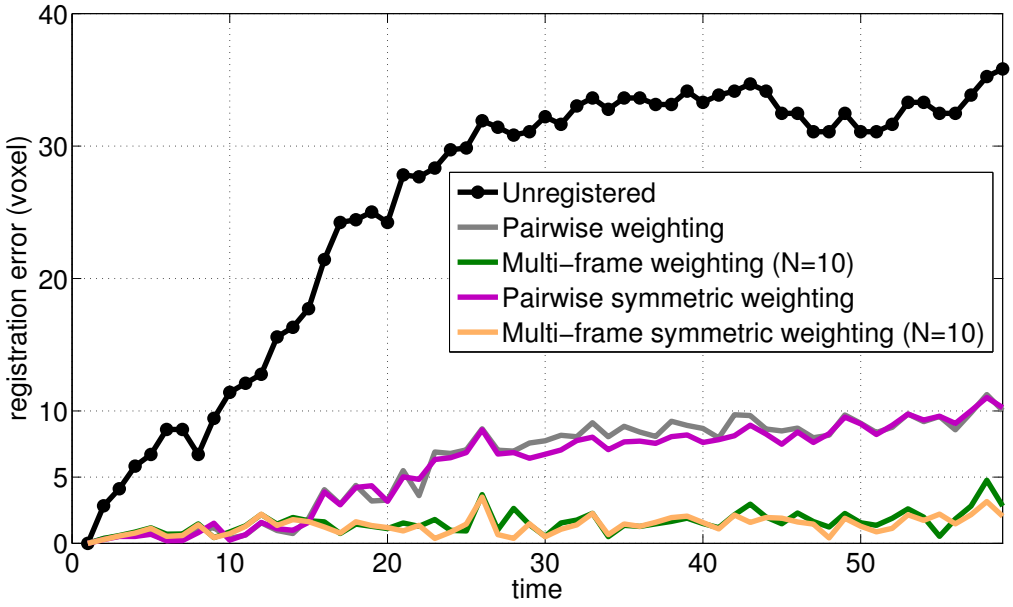

Figure 5.20: Registration error for a spot-like structure in the 3D real image sequence E as a function of time for the weighting and the symmetric weighting variant of our diffeomorphic multi-frame approach as well as pairwise registration.

and symmetric weighting approach of Kim et al. [11] and our non-diffeomorphic multi-frame weighting and symmetric weighting approach (with $N = 10$, see Chapter 4.2). Both approaches are based on local optic flow estimation and have been previously used for registration of cell microscopy images. Moreover, we have used the log-domain diffeomorphic demons registration approach of Vercauteren et al. [10] (denoted with Log-Demons) which was previously used for pairwise registration of static medical images (MR images of the brain). We have extended this approach for application to temporal images using a pairwise as well as a multi-frame (with $N = 10$) consecutive scheme (analogously to the pairwise and the multi-frame variant of our diffeomorphic approach) and have included it in our comparison. For regularization of the vector fields, we used a Gaussian kernel with $\sigma_G = (2, 2, 1)$ voxel for the update velocity fields $d\mathbf{v}^{(i)}_{k,k-1}$ as well as the velocity fields $\mathbf{v}^{(i)}_{k,k-1}$, and $\sigma_G = (1, 1, 0.5)$ voxel for the inverse deformation fields $\mathbf{u}_{l,k-1}$ as well as the deformation fields $\mathbf{u}_{k,1}$. We tested different parameters for the Gaussian kernel and used the ones which yielded the best results. For

Non-rigid registration approaches	Temporal registration	Spatial optimization	Diffeo-morphic	Flow boundary preserving regularization
Pairwise [11]	pairwise	local	No	No
Multi-frame [118]	multi-frame	local	No	No
Log-Demons [10]	pairwise	global	Yes	No
Temporal groupwise [12]	groupwise	global	Yes	No
Diffeomorphic pairwise	pairwise	local	Yes	Yes
Diffeomorphic multi-frame	multi-frame	local	Yes	Yes

Table 5.12: Non-rigid registration approaches investigated in the experiments.

the multi-frame extension we have used a temporally weighted mean image based on Gaussian weighting (see Section 4.2). For the evaluation based on 2D data we have also applied the temporal groupwise diffeomorphic registration approach of Metz et al. [12] which is based on B-splines and was previously used for temporal registration of medical images (CT, MR, and US images of the heart and the lung). With this approach, all images of an image sequence are registered simultaneously by minimizing the sum of squared intensity differences between all images and the mean image of the whole sequence. For our comparison, we used the implementation of the approach in elastix [127]. We used a grid spacing of 16×16 pixel, each time point of the sequences, and three multiresolution levels. We tested different values for the grid spacing and used the grid with the best result. An overview of the investigated non-rigid registration approaches and their main characteristics is given in Table 5.12. In Fig. 5.21(a) we show an example of the registration error for one spot-like structure in the 2D real image sequence C using our diffeomorphic multi-frame weighting approach and its pairwise variant in comparison to four previous approaches. It can be seen, that the temporal groupwise approach [12] yields the largest errors and a mean error of $e_{mean} = 16.4$ pixel. For time points in about the middle of the sequence, [12] yields the lowest errors,

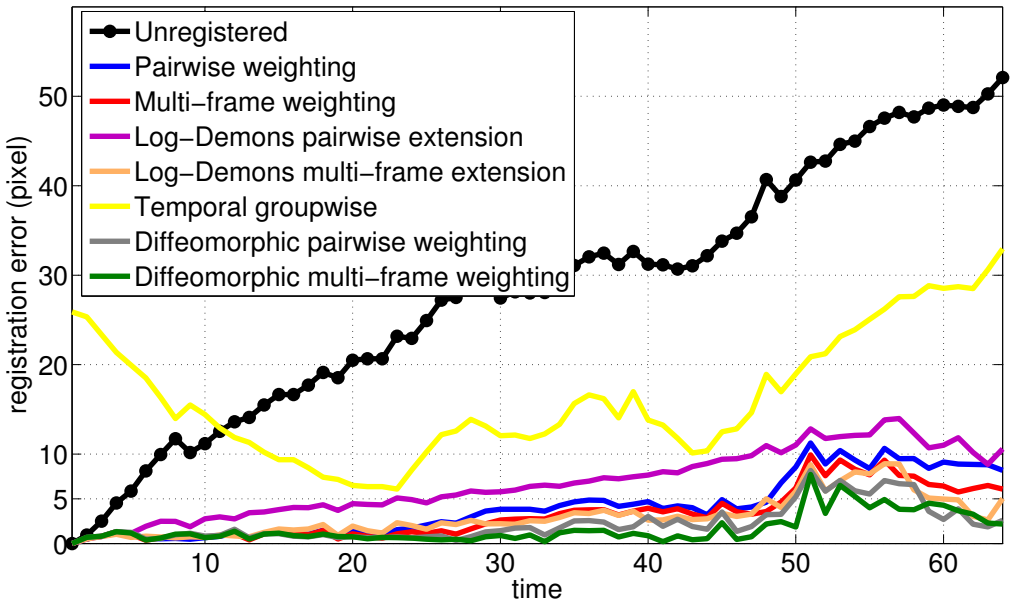

(a) 2D image sequence C

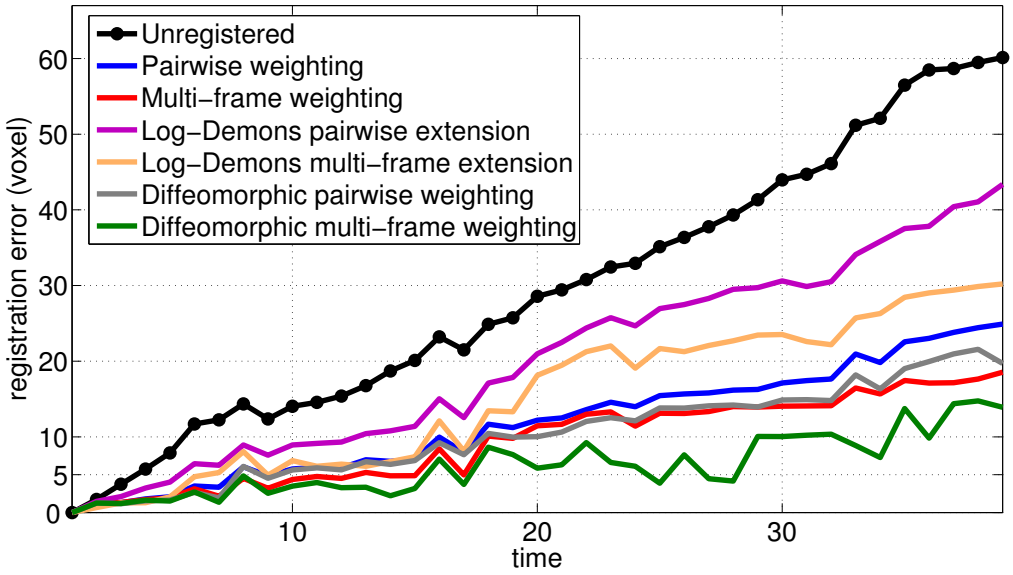

(b) 3D image sequence E

Figure 5.21: Registration error for a spot-like structure in two real image sequences as a function of time for the diffeomorphic multi-frame approach (N=10) and its pairwise variant as well as for other registration approaches.

which is what we expect since the images at these time points are most similar to the employed mean image. In contrast, for time points away from the middle time point the error increases strongly. The mean errors for the Log-Demons [10] pairwise extension, the Log-Demons [10] multi-frame extension, the pairwise weighting approach [11], and the multi-frame weighting approach [118] are $e_{mean} = 6.73$ pixel, $e_{mean} = 3.01$ pixel, $e_{mean} = 4.09$ pixel, and $e_{mean} = 3.26$ pixel, respectively. Our diffeomorphic multi-frame weighting approach yields the lowest error ($e_{mean} = 1.63$ pixel). When averaging over all spot-like structures of all four 2D real image sequences our diffeomorphic multi-frame registration approach yields the lowest values for $\overline{e}_{mean}$ and $\overline{\sigma}_{e_{mean}}$ (either by the weighting or the symmetric weighting approach) compared to the six previous approaches, and the improvement is 40% and 37%, respectively, compared to the lowest error obtained by six previous approaches (cf. Table 5.11). In Fig. 5.21(b) we show an example of the registration error for one spot-like structure in the 3D real image sequence E using our approach in comparison to three previous approaches. Also in this example our diffeomorphic multi-frame weighting approach yields the lowest error $e_{mean} = 6.19$ voxel, and the pairwise variant yields $e_{mean} = 10.3$ voxel. In comparison, the Log-Demons [10] pairwise extension, the Log-Demons [10] multi-frame extension, the pairwise weighting approach [11], and the multi-frame weighting approach [118] yield $e_{mean} = 20.1$ voxel, $e_{mean} = 15.2$ voxel, $e_{mean} = 11.8$ voxel, and $e_{mean} = 9.53$ voxel, respectively. When averaging over all spot-like structures of the two 3D real image sequences our symmetric weighting approach yields the lowest errors for $\overline{e}_{mean}$ and $\overline{\sigma}_{e_{mean}}$, and the improvement is 37% and 31%, respectively, compared to the lowest error obtained by the three previous approaches (cf. Table 5.11).

To investigate whether the improvement of the diffeomorphic multi-frame approach (for both the weighting and the symmetric weighting variant) compared to the previous registration approaches as well as compared to pairwise registration for the 2D and 3D real data is statistically significant, we performed Wilcoxon signed-rank tests

(non-parametric test). Prior application of a Shapiro-Wilk test showed that the data do not follow a normal distribution in all 12 cases (2 registration variants, 6 image sequences). Using a significance level of 5% we obtained $p < 0.016$ for all tests. Thus, the multi-frame approach yields a statistically significant improvement compared to the previous registration approaches as well as compared to pairwise registration, for both the weighting as well as the symmetric weighting variant.

In Fig. 5.22 we show a comparison of results for our diffeomorphic multi-frame weighting approach and the Log-Demons [10] multi-frame extension as well as for the respective pairwise registration approaches, for the 2D real image sequence D (time points 1 and 20). It can be seen, that the alignment of the nucleus in the registered images is significantly improved compared to the unregistered case for all approaches. It can be also seen, that the alignment of subcellular structures in the inner part of the nucleus is better for multi-frame registration, compared to pairwise registration, for both registration approaches. In addition, the alignment of subcellular structures is better for our diffeomorphic multi-frame and pairwise weighting approach, compared to the respective Log-Demons extensions. There are two reasons for the improved performance. First, the local optimization employed in our approach copes better with the strong local structural changes compared to the global optimization used in [10]. Second, the flow boundary preserving smoothing of deformation vector fields avoids oversmoothing and improves registration accuracy, compared to smoothing using a Gaussian kernel.

To provide further evidence on this and to investigate the influence of the local optimization scheme and the flow boundary preserving scheme separately, we have implemented a modified version of our diffeomorphic registration approach which uses Gaussian kernels for smoothing of deformation vector fields (with the same parameters as in [10], see above) instead of the flow boundary preserving scheme. The results of applying our modified approach can be found in Table 5.11, for the diffeomorphic multi-frame weighting registration approach, as well as for pairwise registration. First, it can

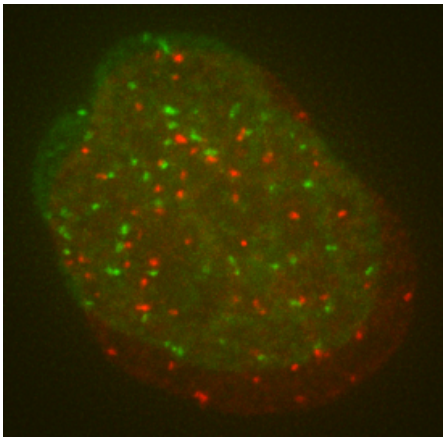

(a) Unregistered

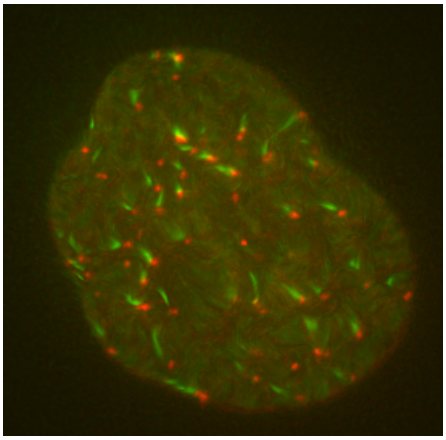

(b) Log-Demons pairwise extension

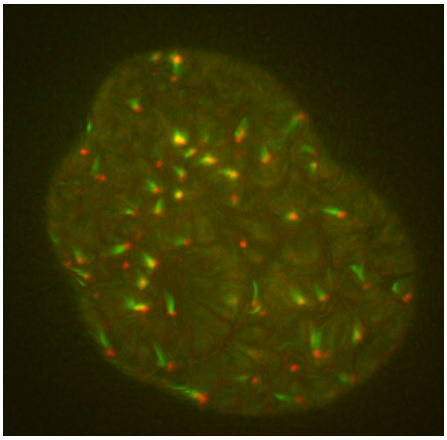

(c) Log-Demons multi-frame extension

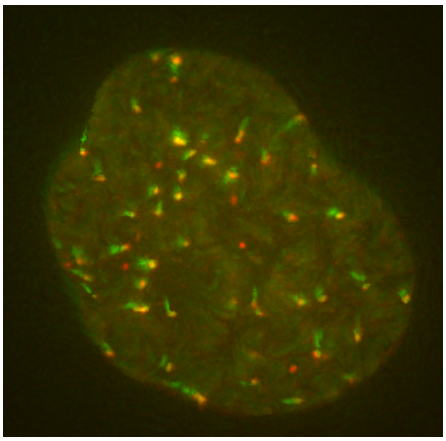

(d) New diffeomorphic pairwise

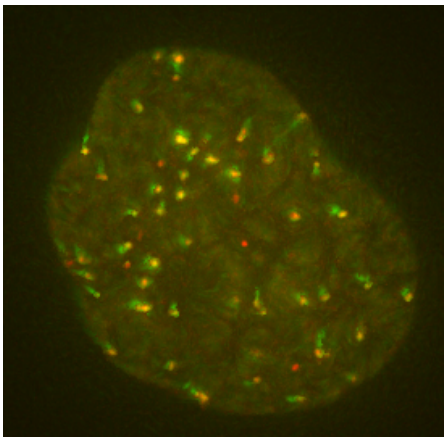

(e) New diffeomorphic multi-frame

Figure 5.22: Overlays of images for time points 1 (red) and 20 (green) of the 2D real image sequence D for (a) the unregistered images, and for the registered images using (b,c) the Log-Demons [10] extensions and (d,e) the new diffeomorphic weighting approach. Yellow indicates overlapping intensities.

be seen, that for almost all cases the registration error for the diffeomorphic weighting approach using Gaussian kernels is larger compared to our original diffeomorphic weighting approach with flow boundary preserving regularization (for pairwise as well as multi-frame registration). The improvement for pairwise registration averaged over the four 2D and the two 3D image sequences is 10% and 4%, respectively, and the respective improvement for multi-frame registration is 21% and 20%, for the 2D and the 3D image data, respectively. Thus, flow boundary preserving regularization is superior compared to regularization based on Gaussian kernels. Second, compared to [10], our modified approach yields lower errors, and the improvement for pairwise registration averaged over the four 2D and the two 3D image sequences is 43% and 52%, respectively. The improvement for multi-frame registration is 33% and 58% for the 2D and the 3D image data, respectively. We also show an example of the registration error for one spot-like structure in the 3D real image sequence F using our modified pairwise and multi-frame approach in comparison to the respective Log-Demons approaches (Fig. 5.23). It can be seen, that our modified pairwise and multi-frame approach yields lower errors compared to the Log-Demons extensions, for all time points of the image sequence. Thus, the main reason for the improved performance of our approach for the used image data compared to [10] is the employed local optimization scheme.

We have also performed a sensitivity analysis of the parameters σ_{dist} and σ_{int} which control the smoothing of the deformation vector fields in Eq. (4.2). These parameters influence the registration result most compared to the other parameters. We used different values for σ_{dist} and σ_{int} and applied them for all 2D and 3D real image sequences ($N = 10$) for the weighting variant of our diffeomorphic multi-frame registration approach. We computed the mean registration error as well as the gradient norm of the deformation vector fields which characterizes the smoothness averaged over all image sequences (see Fig. 5.24). For the diagrams of σ_{dist} in Figs. 5.24(a) and 5.24(c) we used $\sigma_{int} = 4$, and for the diagrams of σ_{int} in Figs. 5.24(b) and 5.24(d) we used $\sigma_{dist} = 2$ voxel

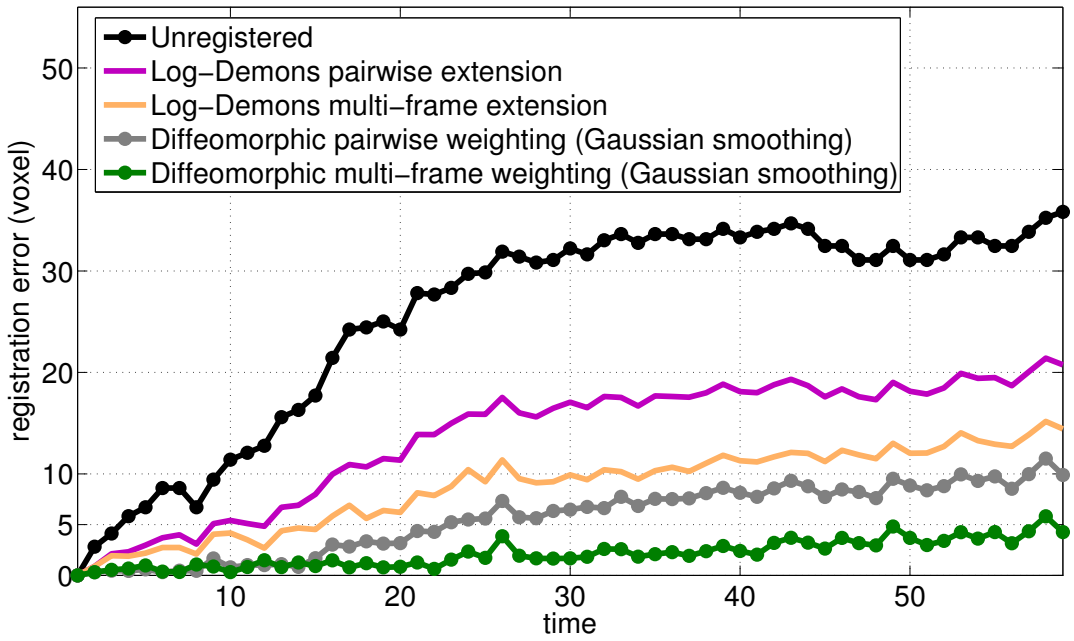

Figure 5.23: Registration error for a spot-like structure in the 3D real image sequence F as a function of time for our diffeomorphic multi-frame weighting approach (using Gaussian smoothing) and the Log-Demons multi-frame extension, as well as for the respective pairwise registrations.

(as in the parameter setting used for our approach, see Section 5.3.1). In Fig. 5.24(c) it can be seen, that for achieving a certain level of smoothness for the deformation vector fields, a value of $\sigma_{dist} \geq 2$ voxel is required. Note, that a certain amount of smoothness is necessary, however, too strong smoothing results to over-smoothing. We have chosen $\sigma_{dist} = 2$ voxel since increasing the value to $\sigma_{dist} = 3$ voxel significantly increases the mean registration error in Fig. 5.24(a). Generally, we considered changes of more than about 5% as significant. Analogously, based on the diagrams in Figs. 5.24(c) and 5.24(d) a good choice for σ_{int} are the values 3 or 4. Taking also into account a sensitivity analysis for the 2D and 3D synthetic data, we have chosen values of $\sigma_{dist} = 2$ voxel and $\sigma_{int} = 4$ in our experiments.

Finally, we determined the computation time for registration of the first 100 images of the 2D real image sequence B (384×384 pixel) and the first 50 images of the 3D image sequence F ($512 \times 512 \times 10$ voxel). We compared our diffeomorphic multi-frame

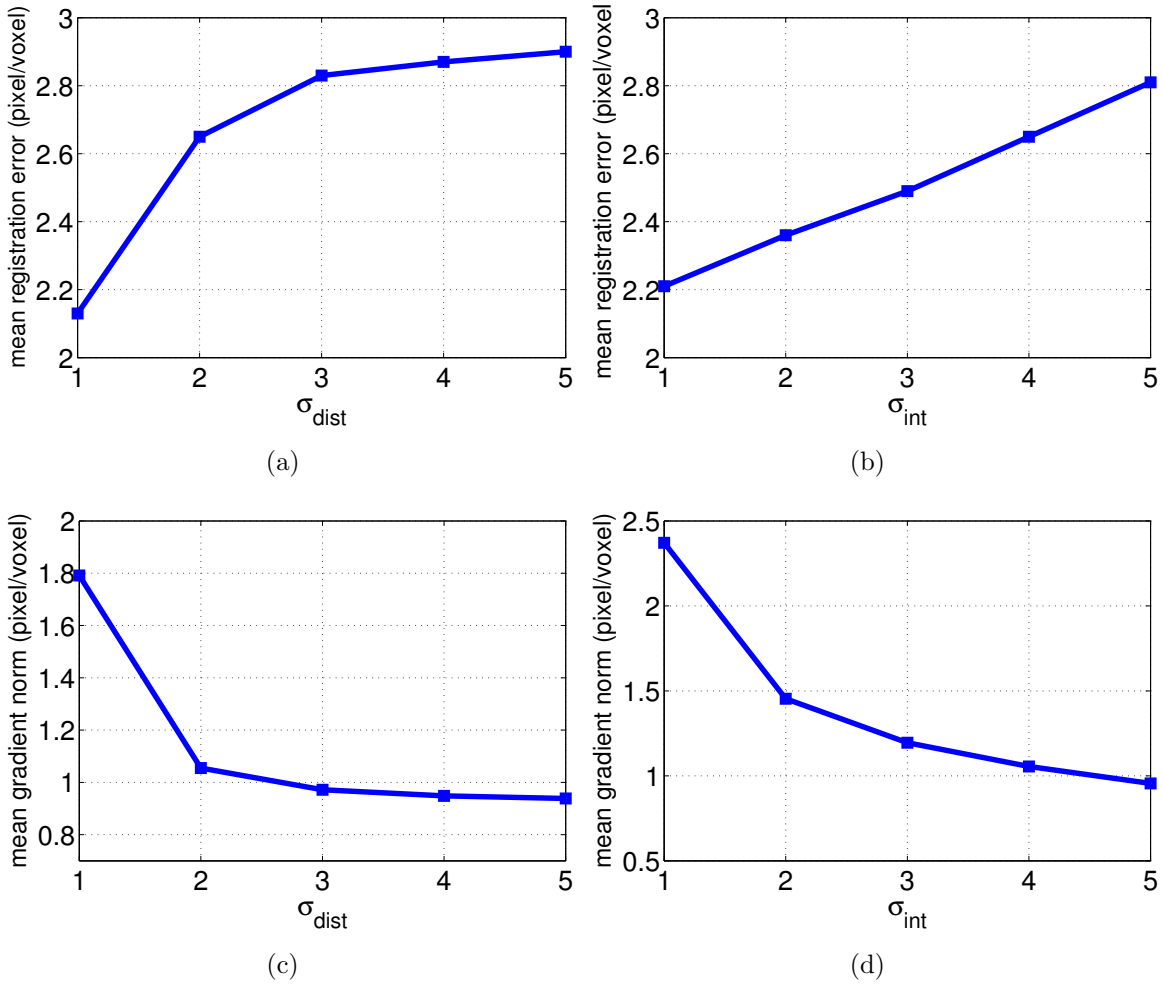

Figure 5.24: Registration error (top) and mean gradient norm (bottom) averaged over the 2D and the 3D real image sequences as a function of the parameters σ_{dist} and σ_{int} for the new diffeomorphic multi-frame weighting registration approach ($N = 10$). For the different values of σ_{dist} we have used $\sigma_{int} = 4$, and for the different values of σ_{int} we have used $\sigma_{dist} = 2$ voxel.

weighting approach with its pairwise variant as well as with the pairwise and the multi-frame weighting approaches in [118] (see Chapter 3). For the 2D data the computation times can be found in Table 5.13. For both multi-frame approaches the computation time is increasing with increasing N, however, the increase is significantly smaller for our diffeomorphic multi-frame approach compared to [118]. For example, the increase of the computation time for $N = 10$ is 565% for [118] and 36% for our approach, compared to the respective pairwise registration. We have determined the differences of computation

		Multi-frame weighting [118]	New diffeomorphic multi-frame	Difference
pairwise		0 h 40	1 h 36	+140%
multi-frame	$N = 3$	1 h $16_{+90\%}$	1 h $37_{+1\%}$	+27%
	$N = 5$	2 h $04_{+210\%}$	1 h $47_{+11\%}$	−14%
	$N = 10$	4 h $26_{+565\%}$	2 h $11_{+36\%}$	−51%
	$N = 20$	8 h $23_{+1158\%}$	2 h $41_{+68\%}$	−68%

Table 5.13: Computation time for the registration of the first 100 images from the 2D real image sequence B using the new diffeomorphic multi-frame weighting approach compared to the multi-frame weighting approach [118] for different values of N. Percentages indicate the increase compared to pairwise registration. The percentages in the last column indicate the difference of the computation time between the diffeomorphic multi-frame approach and the approach in [118].

times in percentage between our diffeomorphic multi-frame approach and [118] for each value of N (column "Difference" in Table 5.13). For $N = 2$ (pairwise registration) the computation time of our approach is higher compared to [118], and the difference is +140%. For $N = 3$ the difference decreases to +27%, and further decreases with increasing N. For $N \geq 5$ the differences are negative, i.e., the computation time is lower for our approach compared to [118]. For the 3D data, our diffeomorphic multi-frame approach with $N = 10$ yields a computation time of 27 h 50 min. The change compared to pairwise registration is +49%, and the change compared to [118] is −91%. We used a workstation under Linux with an Intel Xeon E5530 CPU (2.4 GHz). Note, that our implementation is currently not parallelized and further optimization is possible, thus the computation time can be further reduced.

Chapter 6

Discussion and Conclusion

6.1 Discussion

6.1.1 Non-Rigid Multi-Frame Registration

From the experimental results based on synthetic as well as real microscopy image sequences, it turned out that our multi-frame registration approach outperforms pairwise registration. The main reason for the improved performance of the multi-frame approach is the exploitation of the information from multiple images which improves the accuracy of the registration results.

Based on synthetic image sequences we showed that the multi-frame approach is more robust to image noise and intensity variations compared to pairwise registration. The reason for the higher robustness is that the multi-frame approach takes advantage of the additional temporal information and the previously computed transformations which are used to warp the multiple consecutive images. The multiple warped images exploited by the multi-frame approach act as a kind of regularization that constrains the registration result compared to the pairwise approach. This improves the robustness to noise and structural changes of the intensities.

Based on real microscopy image sequences, we showed that using the multi-frame

approach the registration error is significantly lower compared to pairwise registration and outliers are significantly reduced using $N \geq 20$ number of image frames and temporal weighting. The temporal weighting schemes reduce the influence of less relevant images, i.e. images that are more distant or less similar to the image at the current time point. Temporal weighting does not only reduce outliers, but also reduces the influence of N on the results since the variation of the registration error for the different values of N (particularly for $5 \leq N \leq 30$ and for the maximum registration error) is smaller compared to the multi-frame approach without temporal weighting. The number of frames N for multi-frame registration should be chosen based on the application, i.e. whether the mean or the maximum registration error is more important. For our application, considering the mean and maximum error and the computation time, a good choice based on the experimental results is $N = 10$ or $N = 20$ for the multi-frame approach with temporal weighting based on image similarity. These values for N are a good compromise between the computation time and the registration accuracy. Compared to, for example, $N = 30$, the computation time is much lower and the difference in performance is not so large. In general, the main factors for determining the optimal value of N are the strength of the cell motion, the strength of the cell deformations, and the strength of the intensity changes. However, finding a quantitative relation between all these factors (that change over time) and the optimal value of N is difficult, and the question is whether for a new data one can estimate these factors beforehand. Generally, the larger the changes the smaller the value for N should be chosen. The reason is that in case of large changes the images differ more. In addition, N should not be chosen too large because of computational complexity, for example, for $N = 30$ the computation time is relatively high. Thus, in other applications, where the cell motion, the cell deformations, and the intensity changes are not as large as in our case, a larger value of N could be chosen or vice versa.

All three variants of the multi-frame approach yield a significant improvement com-

pared to pairwise registration, however, there is no clear preference for one of the variants. The symmetric variant generally yields the best result for the synthetic image data, while the weighting approach yields the best result for the real image data (e.g., based on the average value). However, the differences between the three variants are generally not very large. Moreover, we investigated the convergence rate of the optimization scheme of the multi-frame approach and found that the convergence rate is similar to the pairwise approach. Finally, we showed that our approach yields better results than a temporal groupwise registration approach which was previously used for the registration of medical image data.

6.1.2 Non-Rigid Diffeomorphic Multi-Frame Registration

From the experiments based on synthetic as well as real 2D and 3D microscopy image sequences, it turned out that our diffeomorphic multi-frame non-rigid registration approach yields better results than pairwise registration and our non-diffeomorphic multi-frame registration approach. There are two main reasons for the improved performance. First, our approach is diffeomorphic which guarantees that the determined transformations are invertible and smooth. This is important since our approach uses inverse transformations to construct a temporal mean image which is used to register single frames of the image sequence. In contrast, our non-diffeomorphic multi-frame registration approach uses a scheme for inversion of transformations which are not guaranteed to be invertible. Second, the employed flow boundary preserving smoothing method prevents over-smoothing of deformation vector fields, leading to more accurate registration results compared to standard Gaussian smoothing. In addition, our diffeomorphic multi-frame registration approach is computationally more efficient than our non-diffeomorphic approach, for two main reasons. First, our diffeomorphic approach is based on the minimization of the sum of squared intensity differences between each frame of an image sequence and a temporal mean image, in contrast to the non-diffeomorphic approach,

where the sum of squared intensity differences between each frame and multiple previous frames are minimized. Second, in our diffeomorphic approach the inverse transformations are efficiently computed using vector fields computed in the log-domain. From our experimental results we found that the reduction of computation time due to these two reasons is larger for multiple frames $N \geq 5$ than the increase in computation time due to the use of the log-domain diffeomorphic update rule (compared to the additive update rule in our non-diffeomorphic approach) and due to the use of the flow boundary preserving smoothing (compared to Gaussian smoothing in our non-diffeomorphic approach). From a comparison of the two intensity-based variants (weighting and symmetric weighting) of our diffeomorphic registration approach it turns out that the results are similar. In most cases the weighting approach yields slightly lower registration errors for the 2D image data, and the symmetric weighting approach yields lower errors for the 3D image data. However, the differences are relatively small.

We have also shown that our diffeomorphic multi-frame registration approach outperforms a pairwise as well as a multi-frame temporal extension of the diffeomorphic registration approach in [10]. The first reason is that our approach is based on local optic flow estimation which is advantageous for our application since the image data contain many local structural changes, compared to the global optimization in [10]. Second, employing flow boundary preserving smoothing in our approach prevents oversmoothing of deformation vector fields, compared to Gaussian smoothing in [10]. Based on a quantitative comparison, we have shown that the improvement is mainly due to the local optimization scheme, compared to the flow boundary preserving smoothing. Compared to a temporal groupwise approach [12] which is based on B-splines and was previously used for registration of medical images, our approach yields better results. The reason is, that the simultaneous registration of all frames of an image sequence with large temporal structural changes as in our case is disadvantageous since the frames of an image sequence differ significantly, and the difference generally increases with time

(e.g., compared to medical images of periodic movements such as respiratory motion).

It also turned out that the multi-frame temporal extension (using the proposed multi-frame registration scheme) of the diffeomorphic registration approach in [10] significantly outperforms the pairwise extension. Thus, our proposed multi-frame registration scheme can be used also in conjunction with other approaches for registration of temporal image data, yielding significantly improved results compared to pairwise registration.

6.2 Conclusion

We have presented two multi-frame approaches for temporal non-rigid registration of cell nuclei in live cell microscopy images. Compared to pairwise registration, both multi-frame registration approaches use information from multiple consecutive images simultaneously and take into account computed transformations from previous time points. For our non-diffeomorphic multi-frame registration approach we introduced three intensity-based variants and also investigated two different temporal weighting schemes that control the influence of single frames on the registration result. Using synthetic as well as real 2D cell microscopy image sequences, we have investigated the performance of our approach and we have performed a quantitative comparison with pairwise registration. The results demonstrate that the multi-frame approach yields a more accurate result than pairwise registration, and is more robust against image noise and intensity scaling. We also showed that temporal weighting reduces outliers in the registration results. We have also presented a diffeomorphic multi-frame approach for temporal non-rigid registration of live cell microscopy images. The registration approach computes diffeomorphic transformations based on local optic flow estimation. The determination of diffeomorphic transformations in the log-domain allows efficient computation of the inverse transformations which are used to construct a temporally weighted mean image. The use of a temporal mean image to register single frames of

an image sequence significantly reduces the computation time compared to the non-diffeomorphic multi-frame registration approach. We introduced two intensity-based variants of the diffeomorphic multi-frame registration approach and for regularization of vector fields, we employed a flow boundary preserving method which prevents from over-smoothing of deformation vector fields. Using synthetic as well as real 2D and 3D live cell microscopy image sequences, we have investigated the performance of our approach and we have performed a quantitative comparison with pairwise registration as well as with other temporal registration approaches. The results demonstrate that the diffeomorphic multi-frame registration approach yields a more accurate result than pairwise registration, and significantly outperforms the non-diffeomorphic multi-frame registration approach, a temporal pairwise extension, and a multi-frame extension of a diffeomorphic registration approach, and a temporal groupwise registration approach.

6.3 Future Work

A limitation of the proposed multi-frame registration approaches is that the number of multiple frames is chosen in advance for each image sequence, and is fixed for all time points of a sequence. In future work, the number of multiple frames could be determined automatically for each time point of an image sequence, for example, based on the image similarity of the multiple consecutive frames. To further improve the registration accuracy, different schemes for computing the temporal mean image could be considered. In addition, our registration approaches could be applied to microscopy data from other biological applications. Also, the computation time could be reduced, for example, by parallelization.

Bibliography

[1] J. Lammerding, K. N. Dahl, D. E. Discher, and R. D. Kamm, "Nuclear mechanics and methods," *Methods in Cell Biology*, vol. 83, pp. 269–294, 2007.

[2] M. Zwerger, C. Y. Ho, and J. Lammerding, "Nuclear mechanics in disease," *Annual Review of Biomedical Engineering*, vol. 13, p. 397, 2011.

[3] Y. S. Mao, B. Zhang, and D. L. Spector, "Biogenesis and function of nuclear bodies," *Trends in Genetics*, vol. 27, no. 8, pp. 295–306, 2011.

[4] Y.-C. M. Chen, C. Kappel, J. Beaudouin, R. Eils, and D. L. Spector, "Live cell dynamics of promyelocytic leukemia nuclear bodies upon entry into and exit from mitosis," *Molecular Biology of the Cell*, vol. 19, no. 7, pp. 3147–3162, 2008.

[5] J. W. Newport and D. J. Forbes, "The nucleus: structure, function, and dynamics," *Annual Review of Biochemistry*, vol. 56, no. 1, pp. 535–565, 1987.

[6] J. Liu, A. J. Prunuske, A. M. Fager, and K. S. Ullman, "The COPI complex functions in nuclear envelope breakdown and is recruited by the nucleoporin Nup153," *Developmental Cell*, vol. 5, no. 3, pp. 487–498, 2003.

[7] D. Hernandez-Verdun and T. Gautier, "The chromosome periphery during mitosis," *BioEssays*, vol. 16, no. 3, pp. 179–185, 1994.

[8] J. Beaudouin, D. Gerlich, N. Daigle, R. Eils, and J. Ellenberg, "Nuclear envelope breakdown proceeds by microtubule-induced tearing of the lamina," *Cell*, vol. 108, no. 1, pp. 83–96, 2002.

[9] J. W. Lichtman and J.-A. Conchello, "Fluorescence microscopy," *Nature Methods*, vol. 2, no. 12, pp. 910–919, 2005.

[10] T. Vercauteren, X. Pennec, A. Perchant, and N. Ayache, "Symmetric log-domain diffeomorphic registration: A demons-based approach," in *Proc. International Conference Medical Image Computing and Computer-Assisted Intervention (MICCAI)*, 2008, pp. 754–761.

[11] I.-H. Kim, Y.-C. Chen, D. Spector, R. Eils, and K. Rohr, "Non-rigid registration of 2-D and 3-D dynamic cell nuclei images for improved classification of subcellular particle motion," *IEEE Transactions on Image Processing*, vol. 20, no. 4, pp. 1011–1022, 2011.

[12] C. Metz, S. Klein, M. Schaap, T. van Walsum, and W. J. Niessen, "Nonrigid registration of dynamic medical imaging data using nD+t B-splines and a groupwise optimization approach," *Medical Image Analysis*, vol. 15, no. 2, pp. 238–249, 2011.

[13] M. Holden, "A review of geometric transformations for nonrigid body registration," *IEEE Transactions on Medical Imaging*, vol. 27, no. 1, pp. 111–128, 2008.

[14] B. Zitová and J. Flusser, "Image registration methods: a survey," *Image Vision Computing*, vol. 21, no. 11, pp. 977–1000, 2003.

[15] A. Sotiras, C. Davatzikos, and N. Paragios, "Deformable medical image registration: a survey," *IEEE Transactions on Medical Imaging*, vol. 32, no. 7, pp. 1153–1190, 2013.

[16] W. R. Crum, T. Hartkens, and D. L. Hill, "Non-rigid image registration: theory and practice," *The British Journal of Radiology*, vol. 77, no. 2, pp. S140–153, 2004.

[17] J. B. A. Maintz and M. A. Viergever, "A survey of medical image registration," *Medical Image Analysis*, vol. 2, no. 1, pp. 1–36, 1998.

[18] K. Rohr, "Elastic registration of multimodal medical images: a survey," *Künstliche Intelligenz*, vol. 14, no. 3, pp. 11–17, 2000.

[19] K. Rohr, *Landmark-Based Image Analysis: Using Geometric and Intensity Models*, ser. Computational Imaging and Vision Series. Kluwer Academic Publishers, Dordrecht Boston London, 2001, vol. 21.

[20] F. P. Oliveira and J. a. M. R. Tavares, "Medical image registration: a review," *Computer Methods in Biomechanics and Biomedical Engineering*, vol. 17, no. 2, pp. 73–93, 2014.

[21] D. Rueckert, L. I. Sonoda, C. Hayes, D. L. Hill, M. O. Leach, and D. J. Hawkes, "Nonrigid registration using free-form deformations: application to breast MR images," *IEEE Transactions on Medical Imaging*, vol. 18, no. 8, pp. 712–721, 1999.

[22] G. E. Christensen, M. I. Miller, and M. Vannier, "A 3D deformable magnetic resonance textbook based on elasticity," in *Proceedings of the American Association for Artificial Inteligence, Spring Symposium Series: Applications of Computer Vision in Medical Image Processing.* Standford University, Stanford, CA, 1994, pp. 153–156.

[23] M. Bro-Nielsen and C. Gramkow, "Fast fluid registration of medical images," in *Visualization in Biomedical Computing*. Springer, 1996, pp. 265–276.

[24] S. S. Beauchemin and J. L. Barron, "The computation of optical flow," *ACM Computing Surveys*, vol. 27, no. 3, pp. 433–466, 1995.

[25] P. J. Besl and N. D. McKay, "Method for registration of 3-D shapes," in *Robotics-DL tentative*. International Society for Optics and Photonics, 1992, pp. 586–606.

[26] G. Borgefors, "Hierarchical Chamfer matching: A parametric edge matching algorithm," *IEEE Transactions on Pattern Analysis and Machine Intelligence*, vol. 10, no. 6, pp. 849–865, 1988.

[27] K. Rohr, H. S. Stiehl, R. Sprengel, T. M. Buzug, J. Weese, and M. Kuhn, "Landmark-based elastic registration using approximating thin-plate splines," *IEEE Transactions on Medical Imaging*, vol. 20, no. 6, pp. 526–534, 2001.

[28] J. Kohlrausch, K. Rohr, and H. S. Stiehl, "A new class of elastic body splines for nonrigid registration of medical images," *Journal of Mathematical Imaging and Vision*, vol. 23, no. 3, pp. 253–280, 2005.

[29] N. Alpert, J. Bradshaw, D. Kennedy, and J. Correia, "The principal axes transformation-a method for image registration," *Journal of nuclear medicine*, vol. 31, no. 10, pp. 1717–1722, 1990.

[30] W. Lu, M.-L. Chen, G. H. Olivera, K. J. Ruchala, and T. R. Mackie, "Fast free-form deformable registration via calculus of variations," *Physics in Medicine and Biology*, vol. 49, no. 14, p. 3067, 2004.

[31] K. Brock, M. Sharpe, L. Dawson, S. Kim, and D. Jaffray, "Accuracy of finite element model-based multi-organ deformable image registration," *Medical Physics*, vol. 32, no. 6, pp. 1647–1659, 2005.

[32] G. Hermosillo, C. Chefd'Hotel, and O. Faugeras, "Variational methods for multimodal image matching," *International Journal of Computer Vision*, vol. 50, no. 3, pp. 329–343, 2002.

[33] B. C. Vemuri, J. Ye, Y. Chen, and C. M. Leonard, "Image registration via level-set motion: Applications to atlas-based segmentation," *Medical Image Analysis*, vol. 7, no. 1, pp. 1–20, 2003.

[34] J.-P. Thirion, "Image matching as a diffusion process: an analogy with Maxwell's demons," *Medical Image Analysis*, vol. 2, no. 3, pp. 243–260, 1998.

[35] B. K. P. Horn and B. G. Schunck, "Determining optical flow," *Artificial Intelligence*, vol. 17, no. 1-3, pp. 185–203, 1981.

[36] H.-H. Nagel, "Constraints for the estimation of displacement vector fields from image sequences," in *International Joint Conference on Artificial Intelligence*, 1983, pp. 945–951.

[37] C. Schnörr, "Segmentation of visual motion by minimizing convex non-quadratic functionals," in *Proc. International Conference on Pattern Recognition*, vol. 1, 1994, pp. 661–663.

[38] A. Wedel, T. Pock, C. Zach, H. Bischof, and D. Cremers, "An improved algorithm for TV-L1 optical flow," in *Statistical and Geometrical Approaches to Visual Motion Analysis*. Springer-Verlag Berlin, Heidelberg, 2009, pp. 23–45.

[39] H.-H. Nagel and W. Enkelmann, "An investigation of smoothness constraints for the estimation of displacement vector fields from image sequences," *IEEE Transactions on Pattern Analysis and Machine Intelligence*, vol. 8, no. 5, pp. 565–593, 1986.

[40] L. Álvarez, J. Weickert, and J. Sánchez, "Reliable estimation of dense optical flow fields with large displacements," *International Journal of Computer Vision*, vol. 39, no. 1, pp. 41–56, 2000.

[41] T. Brox, A. Bruhn, N. Papenberg, and J. Weickert, "High accuracy optical flow estimation based on a theory for warping," in *Proc. European Conference on Computer Vision (ECCV), Part IV*, 2004, pp. 25–36.

[42] B. D. Lucas and T. Kanade, "An iterative image registration technique with an application to stereo vision," in *Proc. International Joint Conference on Artificial Intelligence*, 1981, pp. 674–679.

[43] J. L. Barron, D. J. Fleet, and S. S. Beauchemin, "Performance of optical flow techniques," *International Journal of Computer Vision*, vol. 12, no. 1, pp. 43–77, 1994.

[44] S. Uras, F. Girosi, A. Verri, and V. Torre, "A computational approach to motion perception," *Biological Cybernetics*, vol. 60, no. 2, pp. 79–87, 1988.

[45] M. Tistarelli, "Multiple constraints for optical flow," in *Proc. European Conference on Computer Vision*, 1994, pp. 61–70.

[46] M. J. Black and P. Anandan, "Robust dynamic motion estimation over time," in *Proc. IEEE International Conference on Computer Vision and Pattern Recognition*, 1991, pp. 296–302.

[47] G. Farnebäck, "Fast and accurate motion estimation using orientation tensors and parametric motion models," in *Proc. IEEE International Conference on Pattern Recognition*, vol. 1, 2000, pp. 135–139.

[48] X. Pennec, P. Cachier, and N. Ayache, "Understanding the "Demon's Algorithm": 3D non-rigid registration by gradient descent," in *Proc. International Conference Medical Image Computing and Computer-Assisted Intervention (MICCAI)*, 1999, pp. 597–605.

[49] S. Yang, D. Köhler, K. Teller, T. Cremer, P. L. Baccon, E. Heard, R. Eils, and K. Rohr, "Non-rigid registration of 3D multi-channel microscopy images of cell nuclei," in *Proc. International Conference Medical Image Computing and Computer-Assisted Intervention (MICCAI)*, 2006, pp. 907–914.

[50] T. Vercauteren, X. Pennec, E. Malis, A. Perchant, and N. Ayache, "Insight into efficient image registration techniques and the demons algorithm," in *Proc. International Conference on Information Processing in Medical Imaging (IPMI)*, ser. Lecture Notes in Computer Science, vol. 4584. Springer, 2007, pp. 495–506.

[51] A. Trouvé, "Diffeomorphisms groups and pattern matching in image analysis," *International Journal of Computer Vision*, vol. 28, no. 3, pp. 213–221, 1998.

[52] M. F. Beg, M. I. Miller, A. Trouvé, and L. Younes, "Computing large deformation metric mappings via geodesic flows of diffeomorphisms," *International Journal of Computer Vision*, vol. 61, no. 2, pp. 139–157, 2005.

[53] B. B. Avants, C. L. Epstein, M. Grossman, and J. C. Gee, "Symmetric diffeomorphic image registration with cross-correlation: Evaluating automated labeling of elderly and neurodegenerative brain," *Medical Image Analysis*, vol. 12, no. 1, pp. 26–41, 2008.

[54] T. Vercauteren, X. Pennec, A. Perchant, and N. Ayache, "Diffeomorphic demons: Efficient non-parametric image registration," *NeuroImage*, vol. 45, no. 1, pp. S61–S72, 2009.

[55] V. Arsigny, O. Commowick, X. Pennec, and N. Ayache, "A Log-Euclidean framework for statistics on diffeomorphisms," in *Proc. International Conference Medical Image Computing and Computer-Assisted Intervention (MICCAI)*, 2006, pp. 924–931.

[56] N. J. Higham, "The scaling and squaring method for the matrix exponential revisited," *SIAM Journal on Matrix Analysis and Applications*, vol. 26, no. 4, pp. 1179–1193, 2005.

[57] B. Rieger, C. Molenaar, R. W. Dirks, and L. J. van Vliet, "Alignment of the cell nucleus from labeled proteins only for 4D in vivo imaging," *Microscopy Research and Technique*, vol. 64, pp. 142 – 150, 2004.

[58] C. A. Wilson and J. A. Theriot, "A correlation-based approach to calculate rotation and translation of moving cells." *IEEE Transactions on Image Processing*, vol. 15, no. 7, pp. 1939–1951, 2006.

[59] D. Sage, F. Neumann, F. Hediger, S. Gasser, and M. Unser, "Automatic tracking of individual fluorescence particles: application to the study of chromosome dynamics," *IEEE Transactions on Image Processing*, vol. 14, no. 9, pp. 1372 –1383, 2005.

[60] P. Matula, P. Matula, M. Kozubek, and V. Dvorak, "Fast point-based 3-D alignment of live cells," *IEEE Transactions on Image Processing*, vol. 15, no. 8, pp. 2388 –2396, 2006.

[61] W. H. De Vos, R. A. Hoebe, G. H. Joss, W. Haffmans, S. Baatout, P. Van Oostveldt, and E. M. M. Manders, "Controlled light exposure microscopy reveals dynamic telomere microterritories throughout the cell cycle," *Cytometry Part A*, vol. 75A, no. 5, pp. 428–439, 2009.

[62] O. Dzyubachyk, J. Essers, W. A. van Cappellen, C. Baldeyron, A. Inagaki, W. J. Niessen, and E. H. W. Meijering, "Automated analysis of time-lapse fluorescence microscopy images: from live cell images to intracellular foci," *Bioinformatics*, vol. 26, no. 19, pp. 2424–2430, 2010.

[63] I.-H. Kim, C. Cadmus, A. C. Pfeifer, U. Klingmüller, R. Eils, and K. Rohr, "Quantification of FRAP experiments in live cell image sequences by combining segmentation and registration," in *Proc. IEEE International Symposium on Biomedical Imaging (ISBI)*, 2011, pp. 212–215.

[64] S. Li, J. Wakefield, and J. A. Noble, "Automated segmentation and alignment of mitotic nuclei for kymograph visualisation," in *Proc. IEEE International Symposium on Biomedical Imaging (ISBI)*, 2011, pp. 622–625.

[65] L. Chang, W. J. Godinez, I.-H. Kim, M. Tektonidis, P. De Lanerolle, R. Eils, K. Rohr, and D. M. Knipe, "Herpesviral replication compartments move and coalesce at nuclear speckles to enhance export of viral late mRNA," *Proceedings of the National Academy of Sciences*, vol. 108, no. 21, pp. E136–E144, 2011.

[66] K. Klein, A. M. Gigler, T. Aschenbrenner, R. Monetti, W. Bunk, F. Jamitzky, G. Morfill, R. W. Stark, and J. Schlegel, "Label-free live-cell imaging with confocal Raman microscopy," *Biophysical Journal*, vol. 102, no. 2, pp. 360–368, 2012.

[67] T. Würflinger, J. Stockhausen, D. Meyer-Ebrecht, and A. Böcking, "Robust automatic coregistration, segmentation, and classification of cell nuclei in multimodal cytopathological microscopic images," *Computerized Medical Imaging and Graphics*, vol. 28, no. 1, pp. 87–98, 2004.

[68] A. Goobic, J. Tang, and S. Acton, "Image stabilization and registration for tracking cells in the microvasculature," *IEEE Transactions on Biomedical Engineering*, vol. 52, no. 2, pp. 287 –299, 2005.

[69] I.-H. Kim, W. J. Godinez, N. Harder, F. M. Bermúdez, J. Ellenberg, R. Eils, and K. Rohr, "Compensation of global movement for improved tracking of cells in time-lapse confocal microscopy image sequences," in *Proc. SPIE Medical Imaging 2007: Image Processing*, vol. 6512, no. 1, 2007.

[70] J. Mattes, J. Nawroth, P. Boukamp, R. Eils, and K. Greulich-Bode, "Analyzing motion and deformation of the cell nucleus for studying co-localizations of nuclear structures," in *Proc. IEEE International Symposium on Biomedical Imaging (ISBI)*, 2006, pp. 1044 –1047.

[71] S. Yang, D. Köhler, K. Teller, T. Cremer, P. L. Baccon, E. Heard, R. Eils, and K. Rohr, "Nonrigid registration of 3-D multichannel microscopy images of cell nuclei," *IEEE Transactions on Image Processing*, vol. 17, no. 4, pp. 493–499, 2008.

[72] J. De Vylder, W. H. De Vos, E. M. Manders, and W. Philips, "2D mapping of strongly deformable cell nuclei, based on contour matching," *Cytometry Part A*, vol. 79A, no. 7, pp. 580–588, 2011.

[73] D. Sorokin, M. Tektonidis, K. Rohr, and P. Matula, "Non-rigid contour-based temporal registration of 2D cell nuclei images using the Navier equation," in *Proc. IEEE International Symposium on Biomedical Imaging (ISBI)*, 2014, pp. 746–749.

[74] D. V. Sorokin, I. Peterlik, M. Tektonidis, K. Rohr, and P. Matula, "Non-rigid contour-based registration of cell nuclei in 2D live cell microscopy images using a dynamic elasticity model," *IEEE Transactions on Medical Imaging*, vol. 37, no. 1, pp. 173–184, 2018.

[75] G. K. Rohde, A. J. S. Ribeiro, K. N. Dahl, and R. F. Murphy, "Deformation-based nuclear morphometry: Capturing nuclear shape variation in HeLa cells," *Cytometry Part A*, vol. 73A, pp. 341–350, 2008.

[76] G. R. Johnson, T. E. Buck, D. P. Sullivan, G. K. Rohde, and R. F. Murphy, "Joint modeling of cell and nuclear shape variation," *Molecular Biology of the Cell*, vol. 26, no. 22, pp. 4046–4056, 2015.

[77] S. Yoshizawa, S. Takemoto, M. Takahashi, M. Muroi, S. Kazami, H. Miyoshi, and H. Yokota, "Interactive registration of intracellular volumes with radial basis functions," *International Journal of Computational Intelligence and Applications*, vol. 9, no. 3, pp. 207–224, 2010.

[78] S. Tokuhisa and K. Kaneko, "The time series image analysis of the hela cell using viscous fluid registration," in *Proc. International Conference on Computational Science and Its Applications, Part III*, ser. Lecture Notes in Computer Science, vol. 6018. Springer, 2010, pp. 189–200.

[79] A. Hand, T. Sun, D. Barber, D. Hose, and S. MacNeil, "Automated tracking of migrating cells in phase-contrast video microscopy sequences using image registration," *Journal of Microscopy*, vol. 234, no. 1, pp. 62–79, 2009.

[80] D. C. Barber, E. Oubel, A. F. Frangi, and D. Hose, "Efficient computational fluid dynamics mesh generation by image registration," *Medical Image Analysis*, vol. 11, no. 6, pp. 648–662, 2007.

[81] N. Scherf, M. Herberg, K. Thierbach, T. Zerjatke, T. Kalkan, P. Humphreys, A. Smith, I. Glauche, and I. Roeder, "Imaging, quantification and visualization of spatio-temporal patterning in mESC colonies under different culture conditions," *Bioinformatics*, vol. 28, no. 18, pp. 556–561, 2012.

[82] T. Du and M. Wasser, "3D image stack reconstruction in live cell microscopy of Drosophila muscles and its validation," *Cytometry Part A*, vol. 75A, no. 4, pp. 329–343, 2009.

[83] S. Allgeier, A. Zhivov, F. Eberle, B. Koehler, S. Maier, G. Bretthauer, R. F. Guthoff, and O. Stachs, "Image reconstruction of the subbasal nerve plexus with in vivo confocal microscopy," *Investigative Ophthalmology & Visual Science*, vol. 52, no. 9, pp. 5022–5028, 2011.

[84] W.-Y. Hsu, "Analytic differential approach for robust registration of rat brain histological images," *Microscopy Research and Technique*, vol. 74, no. 6, pp. 523–530, 2011.

[85] A. Akselrod-Ballin, D. Bock, R. C. Reid, and S. K. Warfield, "Accelerating image registration with the Johnson-Lindenstrauss Lemma: Application to imaging 3-D neural ultrastructure with electron microscopy," *IEEE Transactions on Medical Imaging*, vol. 30, no. 7, pp. 1427–1438, 2011.

[86] S. Saalfeld, R. Fetter, A. Cardona, and P. Tomancak, "Elastic volume reconstruction from series of ultra-thin microscopy sections," *Nature Methods*, vol. 9, pp. 717–720, 2012.

[87] L. Hogrebe, A. R. Paiva, E. Jurrus, C. Christensen, M. Bridge, L. Dai, R. L. Pfeiffer, P. R. Hof, B. Roysam, J. R. Korenberg, and T. Tasdizen, "Serial section registration of axonal confocal microscopy datasets for long-range neural circuit reconstruction," *Journal of Neuroscience Methods*, vol. 207, no. 2, pp. 200 – 210, 2012.

[88] K. S. Lorenz, P. Salama, K. W. Dunn, and E. J. Delp, "A multi-resolution approach to non-rigid registration of microscopy images," in *Proc. IEEE International Symposium on Biomedical Imaging (ISBI)*, 2012, pp. 198–201.

[89] C.-W. Wang, E. B. Gosno, and Y.-S. Li, "Fully automatic and robust 3D registration of serial-section microscopic images," *Scientific Reports*, vol. 5:15051, 2015.

[90] R. Tomer, A. Denes, K. Tessmar-Raible, and D. Arendt, "Profiling by image registration reveals common origin of annelid mushroom bodies and vertebrate pallium," *Cell*, vol. 142, no. 5, pp. 800–809, 2010.

[91] H. Peng, P. Chung, F. Long, L. Qu, A. Jenett, A. M. Seeds, E. W. Myers, and J. H. Simpson, "BrainAligner: 3D registration atlases of Drosophila brains," *Nature Methods*, vol. 8, no. 6, pp. 493–498, 2011.

[92] L. Qu, F. Long, and H. Peng, "3-D registration of biological images and models: Registration of microscopic images and its uses in segmentation and annotation," *IEEE Signal Processing Magazine*, vol. 32, no. 1, pp. 70–77, 2015.

[93] C. Fowlkes, C. Luengo Hendriks, S. Keränen, G. Weber, O. Rübel, M.-Y. Huang, S. Chatoor, L. Simirenko, A. DePace, C. Henriquez, A. Beaton, R. Weiszmann, S. Celniker, B. Hamann, D. Knowles, M. Biggin, M. Eisen, and J. Malik, "A quantitative spatiotemporal atlas of gene expression in the Drosophila Blastoderm," *Cell*, vol. 133, pp. 364–374, 2008.

[94] B. Lombardot, M. Luengo-Oroz, C. Melani, E. Faure, A. Santos, N. Peyrieras, M. Ledesma-Carbayo, and Bourgine, "Evaluation of four 3D non rigid registration methods applied to early zebrafish development sequences," *MICCAI Workshop in Microscopic Image Analysis with Applications in Biology*, 2008.

[95] L. Pizarro, J. Delpiano, P. Aljabar, J. Ruiz-del Solar, and D. Rueckert, "Towards dense motion estimation in light and electron microscopy," in *In Proc. IEEE International Symposium on Biomedical Imaging (ISBI)*, 2011, pp. 1939–1942.

[96] A. N. Kumar, K. W. Short, and D. W. Piston, "A motion correction framework for time series sequences in microscopy images," *Microscopy and Microanalysis*, vol. 19, no. 02, pp. 433–450, 2013.

[97] M. J. Ledesma-Carbayo, J. Kybic, M. Desco, A. Santos, M. Sühling, P. R. Hunziker, and M. Unser, "Spatio-temporal nonrigid registration for ultrasound cardiac motion estimation," *IEEE Transactions on Medical Imaging*, vol. 24, no. 9, pp. 1113–1126, 2005.

[98] M. Lorenzo-Valdés, G. I. Sanchez-Ortiz, H. G. Bogren, R. Mohiaddin, and D. Rueckert, "Determination of aortic distensibility using non-rigid registration of cine MR images," in *International Conference on Medical Image Computing and Computer-Assisted Intervention (MICCAI)*, 2004, pp. 754–762.

[99] W. Bai and M. Brady, "Spatio-temporal image registration for respiratory motion correction in PET imaging," in *Proc. IEEE International Symposium on Biomedical Imaging (ISBI)*, 2009, pp. 426–429.

[100] J. Vandemeulebroucke, S. Rit, J. Kybic, P. Clarysse, and D. Sarrut, "Spatiotemporal motion estimation for respiratory-correlated imaging of the lungs," *Medical Physics*, vol. 38, no. 1, 2011.

[101] W. Shi, M. Jantsch, P. Aljabar, L. Pizarro, W. Bai, H. Wang, D. O'Regan, X. Zhuang, and D. Rueckert, "Temporal sparse free-form deformations," *Medical Image Analysis*, vol. 17, no. 7, pp. 779–789, 2013.

[102] G. Wu, Q. Wang, J. Lian, and D. Shen, "Estimating the 4D respiratory lung motion by spatiotemporal registration and super-resolution image reconstruction," *Medical Physics*, vol. 40, no. 3, pp. 1–17, 2013.

[103] H. Xu and X. Li, "A symmetric 4D registration algorithm for respiratory motion modeling," in *Proc. International Conference Medical Image Computing and Computer-Assisted Intervention (MICCAI)*, 2013, pp. 149–156.

[104] W. Huizinga, D. H. J. Poot, J.-M. Guyader, R. Klaassen, B. F. Coolen, M. van Kranenburg, R. J. M. van Geuns, A. Uitterdijk, M. Polfliet, J. Vandemeulebroucke, A. Leemans, W. J. Niessen, and S. Klein, "PCA-based groupwise image registration for quantitative MRI," *Medical Image Analysis*, vol. 29, pp. 65–78, 2016.

[105] E. Castillo, R. Castillo, J. Martinez, M. Shenoy, and T. Guerrero, "Four-dimensional deformable image registration using trajectory modeling," *Physics in Medicine and Biology*, vol. 55, no. 1, p. 305, 2010.

[106] Z. Zhang, D. J. Sahn, and X. B. Song, "Temporally consistent diffeomorphic motion estimation with mutual information: Application to echocardiographic sequences," in *IEEE Computer Society Conference on Computer Vision and Pattern Recognition (CVPR) Workshops*, 2012, pp. 84–90.

[107] M. Yigitsoy, C. Wachinger, and N. Navab, "Temporal groupwise registration for motion modeling," in *Proc. International Conference Information Processing in Medical Imaging (IPMI)*, ser. Lecture Notes in Computer Science, vol. 6801. Springer, 2011, pp. 648–659.

[108] H. Sundar, H. Litt, and D. Shen, "Estimating myocardial motion by 4D image warping," *Pattern Recognition*, vol. 42, no. 11, pp. 2514–2526, 2009.

[109] M. De Craene, G. Piella, O. Camara, N. Duchateau, E. Silva, A. Doltra, J. D'hooge, J. Brugada, M. Sitges, and A. F. Frangi, "Temporal diffeomorphic free-form deformation: Application to motion and strain estimation from 3D echocardiography," *Medical Image Analysis*, vol. 16, no. 2, pp. 427–450, 2012.

[110] Z. Zhang, M. Ashraf, D. J. Sahn, and X. Song, "Temporally diffeomorphic cardiac motion estimation from three-dimensional echocardiography by minimization of intensity consistency error," *Medical Physics*, vol. 41, no. 5, p. 0529020, 2014.

[111] D. Perperidis, R. Mohiaddin, and D. Rueckert, "Spatio-temporal free-form registration of cardiac MR image sequences," *Medical Image Analysis*, vol. 9, no. 5, pp. 441–456, 2005.

[112] E. Schreibmann, B. Thorndyke, T. Li, J. Wang, and L. Xing, "Four-dimensional image registration for image-guided radiotherapy," *International Journal of Radiation Oncology Biology Physics*, vol. 71, no. 2, pp. 578 – 586, 2008.

[113] S. Durrleman, X. Pennec, A. Trouvé, G. Gerig, and N. Ayache, "Spatiotemporal atlas estimation for developmental delay detection in longitudinal datasets," in *Proc. International Conference Medical Image Computing and Computer-Assisted Intervention (MICCAI)*, 2009, pp. 297–304.

[114] G. Wu, Q. Wang, and D. Shen, "Registration of longitudinal brain image sequences with implicit template and spatial-temporal heuristics," *NeuroImage*, vol. 59, no. 1, pp. 404–421, 2012.

[115] M. Bieth, H. Lombaert, A. J. Reader, and K. Siddiqi, "Atlas construction for dynamic (4D) PET using diffeomorphic transformations," in *Proc. International Conference Medical Image Computing and Computer-Assisted Intervention (MICCAI)*, 2013, pp. 35–42.

[116] M. Lorenzi and X. Pennec, "Geodesics, parallel transport & one-parameter subgroups for diffeomorphic image registration," *International Journal of Computer Vision*, vol. 105, no. 2, pp. 111–127, 2013.

[117] S. Durrleman, X. Pennec, A. Trouvé, J. Braga, G. Gerig, and N. Ayache, "Toward a comprehensive framework for the spatiotemporal statistical analysis of longitudinal shape data," *International Journal of Computer Vision*, vol. 103, no. 1, pp. 22–59, 2013.

[118] M. Tektonidis, I.-H. Kim, Y.-C. Chen, R. Eils, D. Spector, and K. Rohr, "Non-rigid multi-frame registration of cell nuclei in live cell fluorescence microscopy image data," *Medical Image Analysis*, vol. 19, no. 1, pp. 1–14, 2015.

[119] W. Press, S. Teukolsky, W. Vetterling, and B. Flannery, *Numerical Recipes in C: The Art of Scientific Computing, Second Edition*. Cambridge, UK: Cambridge University Press, 1992.

[120] M. Tektonidis and K. Rohr, "Diffeomorphic multi-frame non-rigid registration of cell nuclei in 2D and 3D live cell images," *IEEE Transactions on Image Processing*, vol. 26, no. 3, pp. 1405–1417, 2017.

[121] H. Lombaert, L. Grady, X. Pennec, N. Ayache, and F. Cheriet, "Spectral log-demons: Diffeomorphic image registration with very large deformations," *International Journal of Computer Vision*, vol. 107, no. 3, pp. 254–271, 2014.

[122] S. Baker and I. Matthews, "Lucas-Kanade 20 years on: A unifying framework," *International Journal of Computer Vision*, vol. 56, no. 3, pp. 221–255, 2004.

[123] M. Bossa, M. Hernandez, and S. Olmos, "Contributions to 3D diffeomorphic atlas estimation: Application to brain images," in *Proc. International Conference Medical Image Computing and Computer-Assisted Intervention (MICCAI)*, 2007, pp. 667–674.

[124] M. Tektonidis, I.-H. Kim, and K. Rohr, "Non-rigid multi-frame registration of live cell microscopy images," in *Proc. IEEE International Symposium on Biomedical Imaging (ISBI)*, 2012, pp. 438–441.

[125] D. Sun, S. Roth, and M. J. Black, "A quantitative analysis of current practices in optical flow estimation and the principles behind them," *International Journal of Computer Vision*, vol. 106, no. 2, pp. 115–137, 2014.

[126] S. Baker, D. Scharstein, J. P. Lewis, S. Roth, M. J. Black, and R. Szeliski, "A database and evaluation methodology for optical flow," *International Journal of Computer Vision*, vol. 92, no. 1, pp. 1–31, 2011.

[127] S. Klein, M. Staring, K. Murphy, M. A. Viergever, J. P. Pluim *et al.*, "Elastix: a toolbox for intensity-based medical image registration," *IEEE Transactions on Medical Imaging*, vol. 29, no. 1, pp. 196–205, 2010.